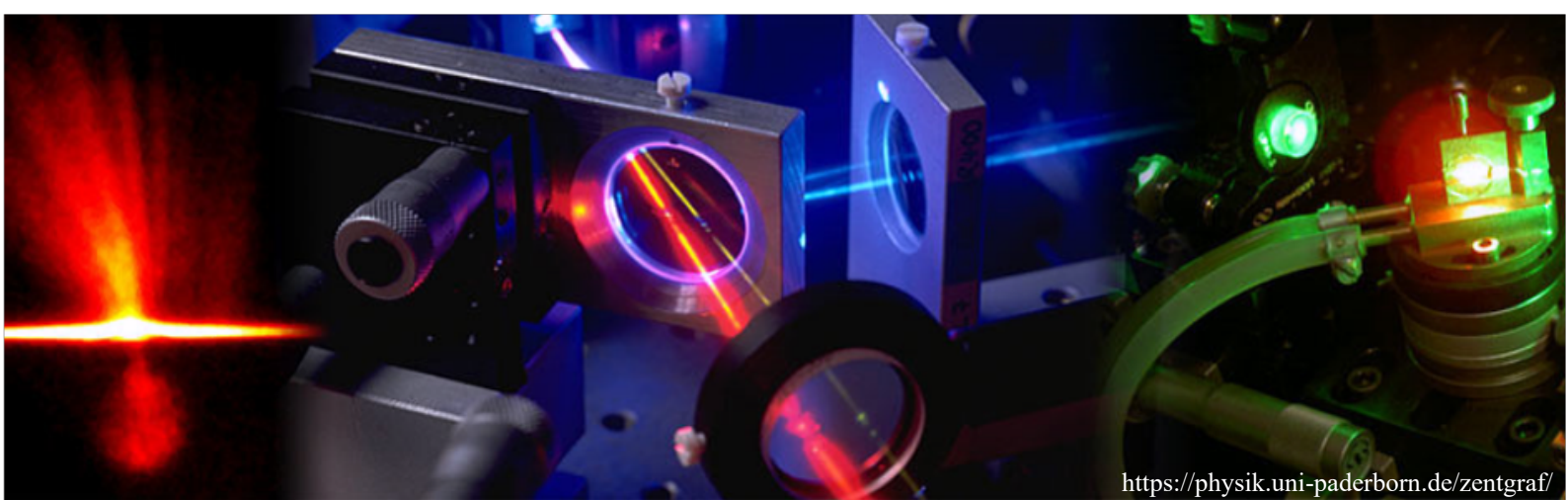




**PADERBORN UNIVERSITY**  
*The University for the Information Society*

# **PLASMONIC AND DIELECTRIC METALENSES FOR NANOPHOTONIC APPLICATION**

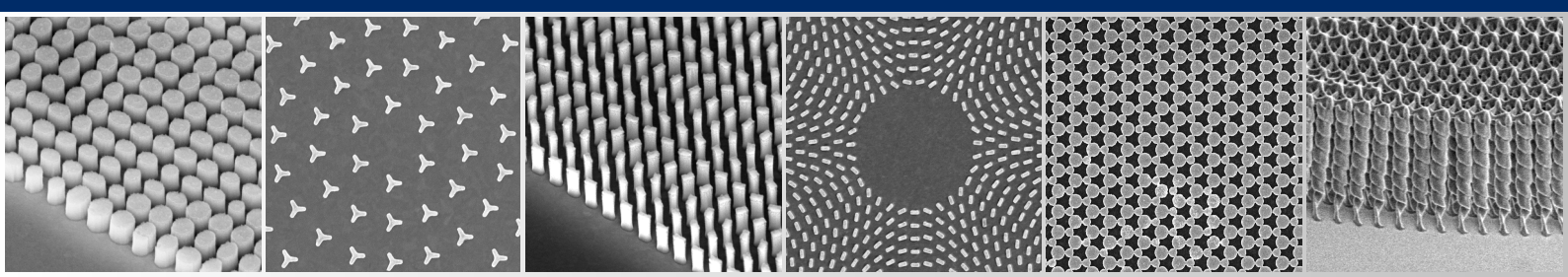


<https://physik.uni-paderborn.de/zentgraf/>

**Dissertation zur Erlangung des akademischen Titels  
doctor rerum naturalium**

**Fakultät der Naturwissenschaften  
Universität Paderborn**

**M.Sc. Christian Schlickriede  
März 2021**







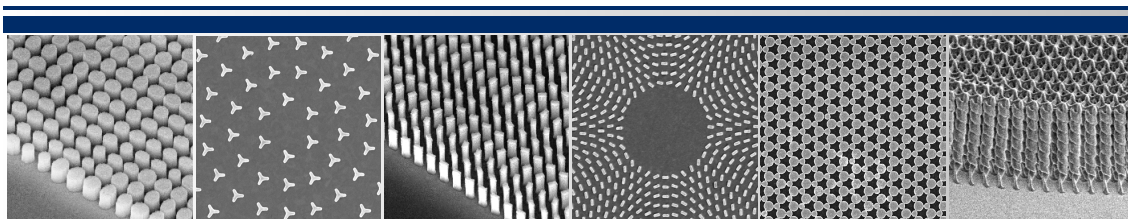
**PADERBORN UNIVERSITY**  
*The University for the Information Society*

# PLASMONIC AND DIELECTRIC METALENSES FOR NANOPHOTONIC APPLICATIONS

Dissertation zur Erlangung des akademischen Titels  
doctor rerum naturalium

Fakultät der Naturwissenschaften  
Universität Paderborn

M.Sc. Christian Schlickriede  
März 2021





---

## Kurzfassung

---

Die vorliegende Arbeit untersucht metallische und dielektrische Metalinsen für verschiedene nanophotonische Anwendungen wie die Bildentstehung mit nichtlinearen Metalinsen und die Integration von Metalinsen in optische Pinzetten.

Die Metaoberflächen werden je nach Anwendung designt und durch Verfahren der Elektronenstrahlolithografie hergestellt. Die experimentelle Charakterisierung erfolgt durch optische Spektroskopieverfahren und Effizienzmessungen.

Unter Verwendung von arrayförmig angeordneten Gold-Nanoantennen mit einer dreizähligen Rotationssymmetrie kann eine nichtlineare Pancharatnam-Berry Phase ausgenutzt werden, um in einem nichtlinearen Prozess zweiter Ordnung eine abrupte Phasenänderung zu implementieren. Dies geschieht ohne eine Veränderung der Fundamentalwelle. Auf diese Weise kann eine nichtlineare Metalinse implementiert werden, welche die Funktionsweise einer ultradünnen flachen Linse mit gleichzeitiger Frequenzkonversion verbindet. Abzubildende Objekte, welche mit infrarotem Licht beleuchtet werden, können so im sichtbaren Spektrum abgebildet werden. Außerdem kann die Funktion der Linse je nach zirkularem Polarisationszustand der Fundamentalwelle verändert werden, dies führt entweder zur realen oder zur virtuellen nichtlinearen Abbildung eines Gegenstandes.

Unter Zuhilfenahme von effizienteren dielektrischen Metaoberflächen basierend auf dem generalisierten Huygens' Prinzip können die Untersuchungen auf nichtlineare optische Phänomene höherer Ordnungen ausgeweitet werden. So kann eine dielektrische Metalinse bestehend aus Silizium-Nanostrukturen zur Erzeugung der dritten Harmonischen realisiert werden. Dadurch kann experimentell und theoretisch demonstriert werden, dass die nichtlineare Bildentstehung nicht der bekannten Gaußschen Linsengleichung unterliegt, sondern einer generalisierten Form dieser Gleichung. Außerdem konnte gezeigt werden, wie die hergestellten Metaoberflächen nichtlineare mathematische Operationen von optischen Signalen ausführen können (zum Beispiel nichtlineare optische Fourier Transformationen oder räumliche Korrelationen verschiedener Ordnungen, die auf dem nichtlinearen Prozess beruhen).

Lineare dielektrische Metalinsen können außerdem als zentrales Element in einer optischen Pinzette fungieren. Es konnte experimentell sowohl die 2D polarisationssensitive Drag- und Drop-Manipulation von in Wasser suspendierten Polystyrolpartikeln als auch die Übertragung von Bahndrehimpulsen auf diese Partikel mit einem einzigen maßgeschneiderten Strahl gezeigt werden.



---

## Abstract

---

The present work investigates metallic and dielectric metalenses for various nanophotonic applications such as image formation with nonlinear metalenses and integration of metalenses into optical tweezers.

The metasurfaces are designed and fabricated by electron beam lithography techniques depending on the application. Experimental characterization is performed by optical spectroscopy techniques and efficiency measurements.

By using an array of gold nanoantennas with a C3 rotational symmetry, a nonlinear Pancharatnam-Berry phase can be exploited to implement an abrupt phase change in a second order nonlinear process. This is done without a change in the fundamental wave. In this way, a nonlinear metalens can be implemented that combines the functionality of an ultrathin flat lens with simultaneous frequency conversion. Objects, which are illuminated with infrared light, can thus be imaged in the visible spectrum. In addition, the function of the lens can be changed depending on the circular polarization state of the fundamental wave, resulting in either real or virtual nonlinear imaging of an object.

With the help of more efficient dielectric metasurfaces based on the generalized Huygens' principle, the investigations can be extended to higher order nonlinear optical phenomena. A dielectric metalens consisting of silicon nanostructures for third harmonic generation can be realized. Thus, it can be demonstrated experimentally and theoretically that the nonlinear image formation is not governed by the well-known Gaussian lens equation but a generalized version of it. It was also shown how the fabricated metasurfaces can perform nonlinear mathematical operations of optical signals (for example, nonlinear optical Fourier transforms or spatial correlations of different orders based on the nonlinear process).

Linear dielectric metalenses can also act as a central element in optical tweezers. Both 2D polarization-sensitive drag and drop manipulation of polystyrene particles suspended in water and the transmission of orbital angular momentum to these particles with a single tailored beam have been demonstrated experimentally.



---

## Declaration

---

I hereby declare that this work is my own work and effort and that it has not been submitted anywhere for any other degree or professional qualification. If other sources of information have been used, they have been acknowledged.

Parts of this work have already been published in peer reviewed journals. A list of publications can be found in appendix [E](#).

March 15, 2021 , Paderborn

Christian Schlickriede



---

## Contents

---

1	Introduction	1
2	From conventional bulky optical elements to metasurface optics	7
2.1	Refractive to diffractive optical elements in a ray optics picture . . . . .	7
2.1.1	Refractive optical lens to focus a ray of light . . . . .	7
2.1.2	Refractive and diffractive lens-like phase profiles . . . . .	8
2.1.3	Conventional lens equation . . . . .	11
2.2	Fundamental concepts to describe plasmonic metasurfaces . . . . .	15
2.2.1	The dielectric function of the free electron gas . . . . .	16
2.2.2	The polarization of light and the geometric Pancharatnam-Berry phase . . . . .	19
	Jones Calculus . . . . .	19
	Stokes parameters and Poincaré sphere . . . . .	21
	The Pancharatnam-Berry phase . . . . .	23
2.3	Plasmonic metalens for linear image formation at infrared wavelength .	27
2.4	The nonlinear lens in a ray optics picture . . . . .	30
2.5	Conclusion . . . . .	31
3	Nonlinear plasmonic metasurfaces for image formation and further applications	33
3.1	Introduction to nonlinear harmonic generation processes . . . . .	33
3.1.1	Selection rules for harmonic generation in nonlinear optics . . . .	37
3.2	Tailor nonlinear optical wavefront control . . . . .	39
3.2.1	Space variant nonlinear Pancharatnam-Berry phase . . . . .	39
3.3	From linear to nonlinear plasmonic metalenses . . . . .	41
3.4	Imaging through nonlinear plasmonic metalens using second harmonic generation . . . . .	43
3.4.1	Nanofabrication of plasmonic metalens . . . . .	44
3.4.2	Optical characterization . . . . .	45
3.4.3	Second harmonic focusing with nonlinear plasmonic metalens . .	47
3.4.4	SHG imaging of real objects . . . . .	51
	Experimental setup . . . . .	51
	A short introduction to the beam propagation method in the nonlinear regime . . . . .	51

SHG image formation of an L-shaped aperture . . . . .	53
3.4.5 Nonlinear plasmonic metalens as 'AND' logic gate . . . . .	56
3.5 Further application possibilities for nonlinear plasmonic metasurfaces . . . . .	57
3.5.1 Spin angular momentum and orbital angular momentum control . . . . .	59
3.6 Conclusion . . . . .	61
<b>4 The nonlinear image formation with nonlinear dielectric metasurfaces . . . . .</b>	<b>63</b>
4.1 Dielectric versus plasmonic metasurfaces and the paradigm shift in nonlinear optics . . . . .	64
4.2 All dielectric nonlinear metalens for third-harmonic generation . . . . .	65
4.2.1 Design concept . . . . .	65
4.2.2 Nanofabrication of the dielectric nonlinear metalens . . . . .	66
4.2.3 Optical characterization with third-harmonic diffraction efficiency . . . . .	66
4.2.4 Focusing of Gaussian beams by a THG metalens . . . . .	68
4.2.5 Derivation of nonlinear lens equation based on the imaging of a single Gaussian beam waist . . . . .	70
4.3 Generalized Gaussian lens equation . . . . .	75
4.4 Higher order nonlinear spatial correlations . . . . .	82
4.4.1 TH imaging of multiple Gaussian beams interfering on the metalens . . . . .	82
4.4.2 Experimental demonstration of TH imaging of two apertures . . . . .	84
4.4.3 Experimental demonstration of TH imaging of three apertures . . . . .	85
4.5 Conclusion . . . . .	86
<b>5 Linear metalenses for integration in optical tweezers . . . . .</b>	<b>89</b>
5.1 A short introduction to optical tweezers . . . . .	90
5.2 Dielectric metasurfaces for integration in optical tweezers: Schematic Concept, Metasurface Design, and Nanofabrication . . . . .	92
5.2.1 Schematic Concept . . . . .	92
5.2.2 Rigorous Coupled Wave Analysis . . . . .	93
5.2.3 Nanofabrication . . . . .	94
5.2.4 Optical Characterization of the Metalens and Vortex Metalens . . . . .	94
5.3 Metasurface enhanced optical tweezers for two-dimensional particle manipulation . . . . .	97
5.3.1 Experimental Setup . . . . .	97
5.3.2 Experimental Results and Discussions . . . . .	99
Metalens optical tweezers for 2D Polarization dependent drag and drop . . . . .	99
5.3.3 Vortex Metalens for OAM transfer with a single tailored beam . . . . .	101
5.4 Conclusion . . . . .	103
<b>6 Summery and Outlook . . . . .</b>	<b>105</b>

---

Bibliography	109
Appendix	129
A Derivation of the lensmaker's equation	129
B Polarization manipulation in an experimental setup	131
C Numerical simulation via beam propagation method for linear and nonlinear metalens	133
D Experimental demonstration of TH imaging of two and three apertures	135
E Scientific publications	137
Acknowledgments	141



# CHAPTER 1

---

## Introduction

---

In historiography, the 20<sup>th</sup> century can be considered as the century of electronics and the origin of today's digital economy. Based on the invention of the electronic tube, that was used as an active electronic component to establish amplifiers and later, the technological break-through of semiconductor technology, innovations like radar and mass media broadcasting were facilitated and since then have determined the everyday human life. In contrast to electronic tubes, field-effect transistors provide high current densities and led to miniaturization through their ability to realize complex integrated circuits on a small length scale with low costs at the same time. Concerning the development of electronics in the 20<sup>th</sup> century, it is noticeable that it has been massively accelerated by smart technologies that led to miniaturization and new functionalities at a price level that is affordable for everyone.

As the faster version of electronics, photonics is dedicated to play the part in the 21<sup>st</sup> century. Thereby, the main difference lies in the type of transmission: Where in electronic components information is carried by electrons, photonic devices use photons. This physical science of light generation, detection and modulation paved the way to modern technologies like high-bandwidth connection to the world wide web, harvesting of solar energy, biotechnology, optical information processing, data security, and many more.

In conventional optical setups, light is controlled and modulated by bulky optical elements like lenses, mirrors, prisms, filters, gratings, optical fibers, waveplates and polarizers. The fabrication of such traditional elements involves complicated processing of natural materials in optical workshops. Limitations for respective application areas are often dictated by natural material properties like the surface topography, absorbance or the refractive index. Prospectively, advanced control of light on small length scale will be one of the key demands.

Nowadays, a new paradigm for designing optical elements is used: Instead of accepting the natural limitations we discovered how to architect material properties at will. Therefore, we make use of the advanced development of nanofabrication in order to construct artificial materials that are called metamaterials. The literal translation 'beyond matter' means it is a new class of three-dimensional (3D) periodic subwavelength plasmonic or dielectric structures that exhibit electromagnetic and/or

magnetic characteristics not found in nature [Che16]. These new synthetic materials enable numerous applications that were previously considered impossible [Zhe12]. One of the best-known examples are materials with a negative refractive index [Smi04]. Despite major breakthroughs in different applications, nanoscale three-dimensional metamaterials usually suffer from high losses and they are expensive and difficult to fabricate [Liu19].

In contrast, the two-dimensional type of metamaterials which is termed *metasurface* offers a route to cost-efficient large area mass manufacturing [She18]. Metasurfaces are artificial planar interfaces that consist of a nanostructured periodic or aperiodic array of carefully designed metallic or dielectric building blocks. It is possible to design and fabricate a deterministic arrangement, shape and orientation of these so-called meta-atoms in order to apply substantial optical modulation to an incident electromagnetic wave at distinct frequency range [Yu14]. Compared to conventional optical elements that accumulate changes of amplitude, phase or polarization while light propagates along the optical path, metasurfaces can be used to tailor these electromagnetic properties abruptly within a sub-wavelength thick device. Consequently, adverse effects of dispersion are reduced to a minimum.

In general, metasurfaces are divided into two categories: They can be made either from metallic or dielectric material. With regard to the size of the nanostructured building blocks, plasmonic metasurfaces belong to the sub-wavelength regime and dielectric metasurfaces to the near-wavelength regime [Gen17]. Metal or plasmonic metasurfaces depend on the surface plasma oscillations within their nanometric building blocks. These are so-called optical nanoantennas referring to their larger analogue at radio-frequency. Due to reflection and ohmic losses caused by the metal structures in the optical band, the efficiency of transmission-type plasmonic metasurfaces is commonly limited to ten percent [Zha19]. Dielectric metasurfaces are based on Mie resonances regarding to the scattering of high-index dielectric nanobricks [Gen17]. This concept refers to the creation of standing wave patterns in dielectric structures and it is used in particular to increase the metasurface efficiency to a current experimentally demonstrated maximum of about ninety percent at visible wavelengths [Che16; Kho17].

In recent years, various plasmonic and dielectric metasurfaces were demonstrated that mimic optical functionalities known from traditional bulky optical elements on the nanoscale, such as achromatic metalenses for imaging [Che18b], optical metaholograms for 3D image reconstruction [Hua13b], broadband orbital angular momentum converters [Hua12], broadband quarter-wave plates [Yu12], ultrathin axicons [Aie12], and others. Based on the recent progress in the development of achromatic properties, metalenses were even awarded by the "Scientific American" as

one of the "Top 10 Emerging Technologies of 2019"<sup>1</sup>. However, exceptional abilities of flat optics offer also new physics and phenomena that are significantly different from those observed in their 3D counterparts. As a famous example, phase discontinuities introduced by metasurfaces deviate from classical laws of reflection and refraction [Ni12; Yu11]. In the past decade, the utilization of metasurfaces and their optical properties have renewed the scientific interest in classical optics, a discipline which was considered to be almost completely understood.

Furthermore, exciting non-conventional phenomena are linked to the ultrafast nonlinear optical response from metasurfaces like frequency conversion processes, such as second- and third-harmonic generation. Natural materials are characterized by an inherently weak nonlinear response, which requires optically large samples, high light intensities, and complex phase matching conditions to obtain measurable nonlinear signals [Kra18]. In striking contrast to bulky nonlinear crystals, ultrathin metasurfaces profit from an enormous relaxation of phase matching conditions because the nonlinear process arises only on a sub-wavelength scale [Li17b]. At the same time, metasurfaces can enhance the light-matter interaction to enable tailorable nonlinearities. This advantage is utilized to create nonlinear metasurfaces that incorporate a dual functionality: On the one hand, they perform a nonlinear optical process and, on the other hand, the wavefront of the nonlinear signal is locally tailored at will [Sch20]. A very interesting example are the recently demonstrated plasmonic nonlinear metalenses based on four-wave mixing and third harmonic generation [Alm16a; Alm16b]. These intrinsically nonlinear lenses are suitable for the focusing of nonlinear signals to a nearly diffraction limited spot.

This thesis is about plasmonic and dielectric ultrathin metalenses for different optical applications that go beyond the frame of just replacing bulky traditional optical functionalities. It is motivated by the fundamental research question of what would happen if a conventional lens made of glass was replaced by a lens made of a nonlinear material. The question arises whether nonlinear imaging can also be described by fundamental concepts, such as the well-known Gaussian lens equation. A scientific goal of the work is therefore to investigate if and how image formation changes for higher order nonlinear processes. It is difficult to answer this question by using conventional bulky nonlinear materials, since the phase-matching conditions would be extremely difficult to satisfy. Due to the previously described advantages, nonlinear metasurfaces are a perfect candidate for the experimental realization. This also results in the goal of fabricating and characterizing nonlinear metalenses which allow imaging of a real object in the nonlinear regime. Such a nonlinear lens would also be interesting for certain technological applications. It permits imaging in the visible region while illuminating an object with fundamental near-infrared (NIR)

---

<sup>1</sup> <https://www.scientificamerican.com/report/the-top-10-emerging-technologies-of-2019/>

light. This could be used, for example, for detectors or cameras which have a high quantum efficiency in the visible spectrum but no sensitivity in the NIR (like silicon CCDs). Such technique might be preferable compared to the imaging principle with phosphorescence because there is no photobleaching and it might be much more suitable for the microscopic investigation of ultrafast processes in the infrared range.

Due to the high efficiencies that can be achieved, linear all-dielectric metasurfaces can be more easily applied in many different technological and scientific fields. An interesting interdisciplinary application idea would be the integration of metalenses into optical tweezers. The manipulation of several particles is usually realized by a bulky spatial light modulator (SLM) and a microscope objective with a very high numerical aperture (NA). In this way, the question arises whether both optical devices can be combined in one ultrathin metalens. Then the efficiency could be optimized for a single wavelength to enable efficient particle manipulation in an ultracompact device.

The thesis is structured in the following way: At first, theoretical fundamentals of the imaging process are explained in the second chapter of this work. Basic physical concepts like the Fermat's principle can be used to explain the image formation from refractive and diffractive optical elements in a ray optics picture. As an example, the linear image formation with the help of a plasmonic metalens is demonstrated and differences to traditional optical elements are discussed.

In the third chapter, basic concepts and functionalities of nonlinear plasmonic metasurfaces are investigated. The linear interaction of light with electronic dipoles is expanded to the nonlinear regime. Nonlinear processes and selection rules for harmonic processes are studied as a theoretical framework to explain nonlinear wavefront control and, more specifically, plasmonic metalenses for second harmonic generation (SHG) based on the Pancharatnam-Berry (PB) phase. Differences between the image formation with a SHG metalens and a conventional lens are discussed. As another intriguing application possibility, a similar nonlinear metasurface design for spin and orbital angular momentum control is discussed.

The investigations are further expanded to all-dielectric metalenses for third harmonic generation (THG). These metasurfaces are based on the generalized Huygens' principle extended to nonlinear optics. The nonlinear wavefront control is emerging from electric and magnetic multipolar Mie resonances. In this way, the efficiency of higher order nonlinear processes is significantly increased. This allows the investigation of the scientific validity of a proposed generalized nonlinear lens equation that can be expanded for higher order harmonic generation processes.

In the fifth chapter, all-dielectric metalenses for the integration in optical tweezers are studied. This concept and its results demonstrate new application areas with new scientific connections to biotechnology or biomedicine. The chapter starts with a basic introduction to optical tweezers, followed by a metalens design concept via rigorous coupled-wave analysis (RCWA). Metasurface enhanced optical tweezers

for two-dimensional particle manipulation is evolved by the means of polarization dependent drag and drop and orbital angular momentum transfer to dielectric particles.

The last chapter of this work summarizes the important results and gives a brief outlook.



# CHAPTER 2

---

## From conventional bulky optical elements to metasurface optics

---

In this chapter the fundamentals of the conventional image formation with linear bulky optical elements are discussed in a ray optics picture. It is discussed how a beam propagates through an ordinary lens, which optical properties a lens has to possess and how conventional imaging proceeds. These basic concepts form a basis one can resort to throughout this work. These fundamental principles are then expanded to metasurface optics and a plasmonic linear metalens is demonstrated experimentally.

### 2.1 Refractive to diffractive optical elements in a ray optics picture

Refractive optical elements can be described physically by geometrical ray optics. The most important fundamental law to describe the geometric ray tracing in this regard is Fermat's principle of least time. All further physical regularities, like Snell's law and the imaging equation can be deduced from Fermat's principle.

#### 2.1.1 Refractive optical lens to focus a ray of light

A conventional bulky refractive lens is an optical device that can focus a collimated beam at an focal point  $F$ . The distance from the center of the lens to this point is called focal distance  $f$ . The question arises how to choose the radius of curvature to focus light exactly at a given focal length. This question can be answered with the help of the lensmaker's equation, whose derivation is completely based on the laws of geometrical ray optics (see appendix A).

$$\frac{1}{f} = \left( \frac{n_2}{n_1} - 1 \right) \left( \frac{1}{R_2} - \frac{1}{R_1} \right) \quad (2.1)$$

The lensmaker's equation is the definition of the focal length  $f$  that combines the physical properties of the lens, namely the ratio of the refractive indices of the lens material  $n_2$  and the surrounding medium  $n_1$ , and both radii of curvature ( $R_i$ ) [Goo05]. Typically, the ray of light propagates in air ( $n_1 = 1$ ) while the lens is made of glass ( $n_2 := n \approx 1.5$ ). Both radii of curvature have the same magnitude but opposite

directions  $R_2 = -R_1$  in case of a double-convex lens. Thus, the focal length is given by the general radius of curvature  $R$ :

$$f = \frac{R}{2(n-1)} \approx R. \quad (2.2)$$

With regard to eq. (2.1),  $f$  will be positive if the difference of both curvatures ( $\frac{1}{R_2} - \frac{1}{R_1}$ ) is positive as well. Thus, lenses whose thickness decreases from the center to the edge are convergent (convex focusing lens), and those whose thickness increases are divergent (concave defocusing lens) [Bor13]. It can be noted at this point that the focusing of conventional lenses and their associated phase profile are fixed and cannot be changed by properties of the light.

### 2.1.2 Refractive and diffractive lens-like phase profiles

In general, a phase profile can be calculated with

$$\Phi = k d_{\text{opt}}, \quad (2.3)$$

where  $k = \frac{2\pi}{\lambda}$  is the wavenumber and  $d_{\text{opt}} = nL$  is the optical path consisting of refractive index  $n$  and propagation length  $L$ . A traditional lens is typically made of curved glass surfaces and it introduces a phase delay that is introduced by the path length difference between rays at different distances from the center of the lens. With regard to fig. 2.1 the optical path through a conventional lens with thickness  $d$  at a position  $\varrho = \sqrt{x^2 + y^2}$  is given by  $d_{\text{opt}} = \delta_1 + \delta_2 + n(d - \delta_1 - \delta_2)$ , where  $\delta_1 + \delta_2$  is the phase delay introduced by the remaining region of free space. Therefore, the lens-like phase profile can be derived to:

$$\Phi_{\text{pl}}(\varrho) = k \cdot d_{\text{opt}}(\varrho) = knd - k(n-1)(\delta_1 + \delta_2), \quad (2.4)$$

where  $k = \frac{2\pi}{\lambda}$  is the free space wave vector and  $\lambda$  is the wavelength. At this point, most textbooks apply the paraxial approximation, which can be applied if  $|R_i| \gg \varrho$  so that  $\delta_i \approx \frac{\varrho^2}{2R_i}$  and  $i \in \{1,2\}$  [Goo05]. It describes a parabolic lens surface:

$$\Phi_{\text{pl}}(\varrho) = knd - k\frac{\varrho^2}{2}(n-1)\left(\frac{1}{R_2} - \frac{1}{R_1}\right). \quad (2.5)$$

Now, the lensmaker's equation (eq. (2.1)) can be substituted as it also satisfies the paraxial approximation (see appendix A). In two dimensions, the position is given by the radius  $\varrho = \sqrt{x^2 + y^2}$  so that

$$\Phi_{\text{pl}}(x,y) = knd - k\frac{(x^2 + y^2)}{2f}. \quad (2.6)$$

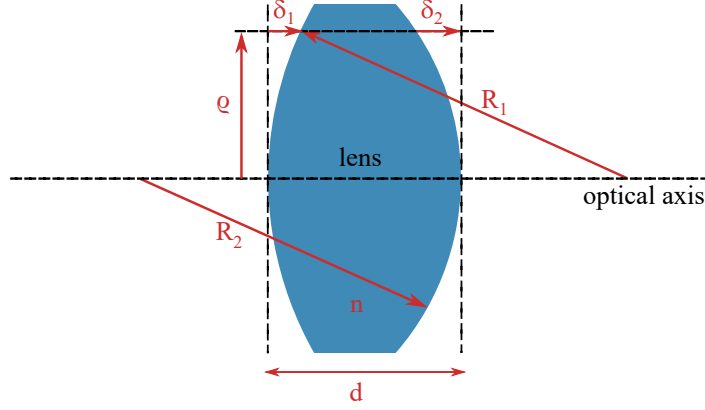


**Figure 2.1: Refractive lens-like phase profile.** Optical lens with refractive index  $n$  and radii of curvature  $R_1$  and  $R_2$  is centered on an optical axis surrounded by air. At a position  $\varrho = \sqrt{x^2 + y^2}$  the optical path  $d_{\text{opt}}$  through the lens is given by  $\delta_1 + \delta_2 + n(d - \delta_1 - \delta_2)$ .

Usually, only the relative phase is important and the constant term  $knd$  can be neglected.

$$\Phi_{\text{pl}}^*(x, y) = -k \frac{(x^2 + y^2)}{2f} \quad (2.7)$$

This equation is taking account for the effects of a thin conventional lens in fundamental textbooks. It features a parabolic phase distribution.

In reality, bulky lenses with a spherical surface (so that  $\delta_i = R_i - \sqrt{R_i^2 - \varrho^2}$ ) are commonly used because they can be produced cost-effectively and with less effort since it is much easier to fabricate a spherical shape than an aspherical one. However, these lenses lead to spherical aberration and therefore they do not allow diffraction-limited focusing and high quality imaging. As carried out in the first sections, the light manipulation in conventional refractive optical elements comes from different optical path lengths that are caused by the curved surface of the lens. This leads to lens thickness in the centimeter range, which can be described with the model of geometrical optics (fig. 2.2a).

In contrast, there are also diffractive flat lenses (e.g. Fresnel lenses), whose thickness is comparable to the wavelength of light. They represent the transition from geometrical optics to wave optics. Diffractive optical lenses mimic refractive lenses, but use a flat phase shift, which is usually wrapped into radial zones ranging from 0 to  $2\pi$ . Thus, they generate a quasi-periodic structure [Eng20]. They greatly reduce spherical aberration with the disadvantage of strong chromatic aberration at

operating wavelengths different from the design wavelength.

A Metalens is also a type of diffractive lens although it offers a fundamentally different concept of phase accumulation: The optical wavefront modulation is induced via the scattering from nanometric structures [Eng20]. The great variety and diversity of these plasmonic and dielectric nanostructures is evident from fig. 2.2c, which illustrates different structures, all of which were designed or fabricated within the further context of this work. They are all characterized by a quasiperiodic structure, but it is smaller than the wavelength of light allowing light manipulation down to a length scale of just a few tens of nanometers (fig. 2.2b).

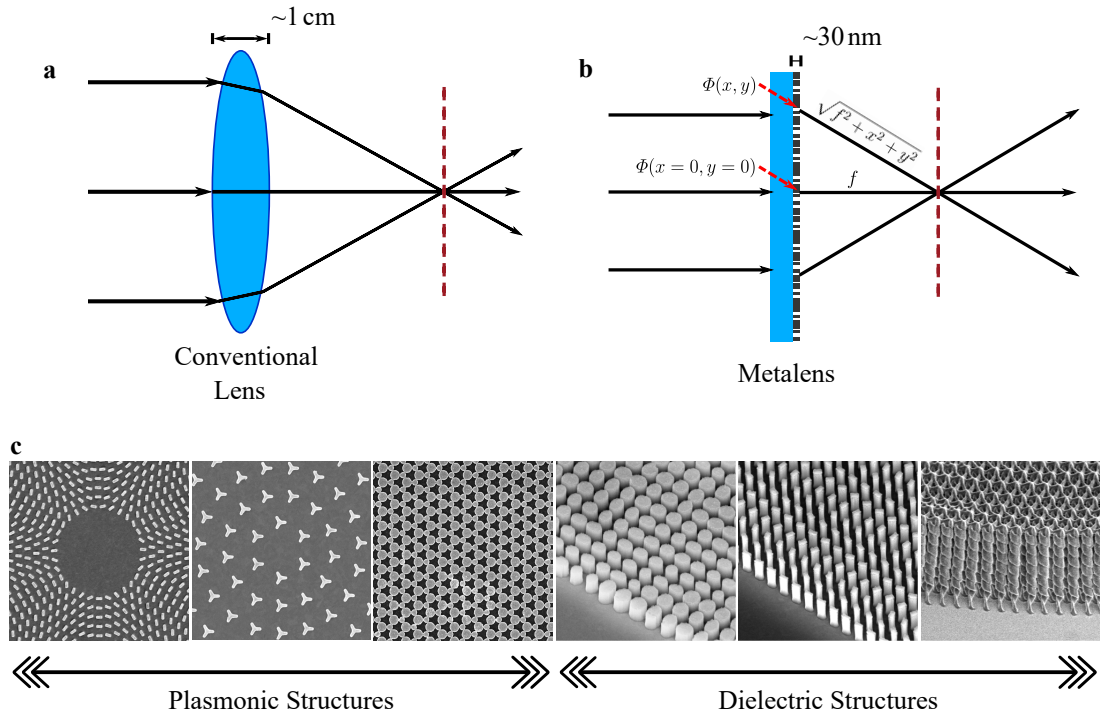


**Figure 2.2: Conventional bulky lens versus an ultrathin metalens.** **a** Regular optical lens that is based on the refraction to focus light at a certain distance. Typically, the thickness is around  $d \approx 1$  cm. **b** In contrast, a metasurface lens is able to bend light at a length scale of a few tens of nanometers. **c** The manipulation of light can be done with various plasmonic or dielectric nanostructures like gold nanoantennas with different rotational symmetries or hexagonally arranged nanodisks, silicon nanopillars or nanofins, or even 3D spiral photonic crystals [Thi07].

Ultrathin planar lenses can be designed to induce a phase front free from spherical aberration that focuses a normally incident plane wave to a diffraction-limited spot in the focal plane [Kho16; Zha21]. In fact, starting from a flat input surface, the spherical phase front is the one that will create a diffraction-limited spot. With

regard to fig. 2.2b, the phase in the center of a flat lens is [Che20]

$$\Phi(x = 0, y = 0) + k d_{\text{opt}} = \Phi(0, 0) + kf, \quad (2.8)$$

where  $k = \frac{2\pi}{\lambda_d}$  denotes the free space wave vector, which corresponds to the design wavelength  $\lambda_d$ . The phase at any point away from the center can be calculated using Pythagoras theorem:

$$\Phi(x, y) + k\sqrt{f^2 + x^2 + y^2}. \quad (2.9)$$

Equating the two phase terms then results in the spherical phase delay for a focusing (converging) lens [Kho16]:

$$\Phi_{\text{sl}}(x, y) = -k(\sqrt{f^2 + x^2 + y^2} - f), \quad (2.10)$$

where  $\Phi(0, 0) = 0$ , because only the relative phase has to be considered. The sign of the phase distribution can be denoted by the variable  $\sigma$ , so that both converging ( $\sigma = -1$ ) and diverging ( $\sigma = +1$ ) spherical lenses can be described. Different phase distributions are shown in fig. 2.3. Panels *a* to *c* refer to converging lenses with different focal lengths and panels *d* to *f* show the corresponding diverging lenses. While all phase distributions refer to a design wavelength of 532 nm, the radial phase interval from 0 to  $2\pi$  shrinks for higher radii and a smaller focal distance. The diameter of these phase distributions is only 100  $\mu\text{m}$ . Even though the concept of geometrical optics is viable for these parameters, there are no manufacturing processes for conventional optical lenses at these dimensions. Only with considerable effort in microfabrication, glass-based components with a diameter with less than 1 mm can be realized [Car19].

### 2.1.3 Conventional lens equation

The imaging equation is one of the most basic equation in textbooks. In a ray optics picture, it is usually derived by simple geometric considerations that already require a lens focusing light in a certain focal length [Sal19]. However, image formation can also be described analytically by Fermat's principle, which states that rays of light travel along the path of least time. This is equivalent to saying that the time of travel (or the optical pathlength) between two points needs to be an extremum relative to neighboring paths. This following calculation only takes into account the phase distribution of the lens. Therefore it is valid for any kind of linear lens regardless of whether it uses refractive or diffractive optics. For simplification we consider the phase distribution of a convex lens only as a function of  $y$ -coordinate ( $x = 0$ ):

$$\Phi(y) = -k(\sqrt{f^2 + y^2} - f). \quad (2.11)$$

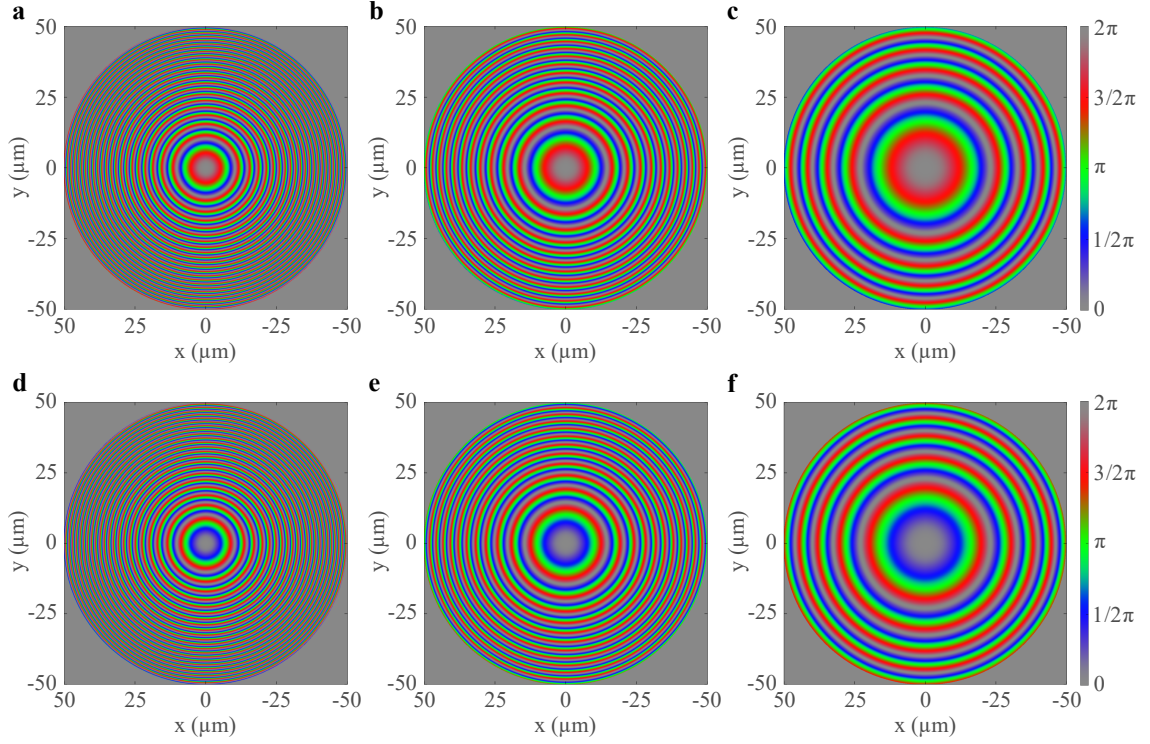


**Figure 2.3: Phase distributions for different spherical lenses.** All lenses have a diameter of 100  $\mu\text{m}$  and they are designed to work at wavelength of 532 nm. The phase distribution alters for different focal lengths according to **a**  $f_a = +100 \mu\text{m}$ , **b**  $f_b = +200 \mu\text{m}$  and **c**  $f_c = +500 \mu\text{m}$  (convergent); **d**  $f_d = -100 \mu\text{m}$ , **e**  $f_e = -200 \mu\text{m}$  and **f**  $f_f = -500 \mu\text{m}$  (divergent).

The question arises which exact path does the light travel in presence of a lens. In the following model, light from the top point of an object  $A$  may take several arbitrary paths  $d_1$  (fig. 2.4). Note that the axial thickness may be neglected in case of a thin lens. After the propagation through the lens, the light beam takes the corresponding path  $d_2$  to form an inverted optical image  $B$ . The distance in  $z$ -direction from object to lens is called object distance  $a$  and the one from lens to image position is called image distance  $b$ . Note that for all following considerations the coordinate origin is placed in the center of the lens to take into account different directions. Now Fermat's principle can be applied to solve the differential equation:

$$\frac{d}{dy}(d_1 k + \Phi(y) + d_2 k) = 0 \quad (2.12)$$

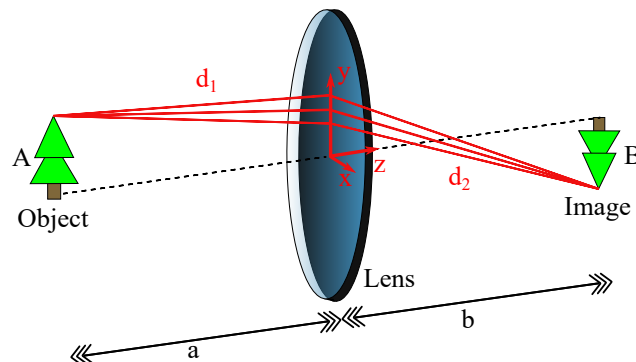


**Figure 2.4: Fermat's Principle describing optical image formation.** Light from an object  $A$  propagates through a regular lens to form an image  $B$  upside down. Fermat's principle can be used to determine the actual light path.

For this purpose, the different optical paths can be expressed depending on the  $y$ -coordinate by using Pythagorean theorem. Note that  $A$  ( $B$ ) are equivalent to the height of the object (image).

$$d_1 = \sqrt{(A - y)^2 + (-a)^2}, \quad d_2 = \sqrt{(-B + y)^2 + b^2} \quad (2.13)$$

Now eq. (2.12) becomes

$$\begin{aligned} \frac{d}{dy} (\sqrt{(A - y)^2 + a^2} - \sqrt{f^2 + y^2} + \sqrt{(-B + y)^2 + b^2}) &= 0 \\ \frac{-A + y}{\sqrt{(A - y)^2 + a^2}} - \frac{y}{\sqrt{f^2 + y^2}} + \frac{-B + y}{\sqrt{(-B + y)^2 + b^2}} &= 0 \end{aligned} \quad (2.14)$$

Simplifying the equation by using the small angle approximation ( $|a| \gg |A| \wedge |b| \gg |B|$ ) leads to:

$$\begin{aligned} \frac{A}{|a|} &= -\frac{B}{|b|} & \text{for } y = 0 \\ \frac{-A + y}{|a|} &= \frac{B - y}{|b|} + \frac{y}{\sqrt{f^2 + y^2}} & \text{for } y \neq 0 \end{aligned} \quad (2.15)$$

In the first case ( $y = 0$ ), it is the central ray propagating through the center of the lens without suffering any deviation. This is a valid approximation for the ideal case of a thin lens. This solution shows that the relation between object size and object distance is equal to the relation between image size and image distance. In other words, to determine the image magnification  $M = B/A$ , it is sufficient to know the

object and image distance:

$$M = \frac{B}{A} = -\frac{|b|}{|a|} \quad (2.16)$$

Assuming a large focal distance  $f$  in comparison to the lens aperture  $d_a$  (diameter of the entrance pupil), the second case from eq. (2.15) can be simplified to derive the conventional lens equation:

$$\frac{1}{|b|} + \frac{1}{|a|} = \frac{1}{\sqrt{f^2 + y^2}} \approx \frac{1}{f} \quad \text{for } f \gg y \quad (2.17)$$

These equations indicate that each point in the object plane is imaged onto a corresponding point in the image plane with a magnification  $M = -\frac{|b|}{|a|}$  that is unity if  $|a| = |b| = 2f$ . The sign describes whether the image is upside down or upright.

This work is about ultrathin lenses that may work at very short focal lengths compared to conventional bulky lenses [Pan18]. Therefore, the experimental environment and configuration will be different, e.g. a much smaller lens aperture need to be illuminated homogeneously. With the help of the image equation, the focal length and possible magnifications for a set of image and object distances can be determined (fig. 2.5). The white line corresponds to a lens with a focal distance of  $f_c = 500 \mu\text{m}$ . The astral data point highlights the experimental configuration for the one-to-one image. This figure illustrates the experimental difficulty in this context. In contrast to traditional optical experiments with bulky elements, the magnification and focal length varies slightly by changing the object and image distance only in the micrometer range. In order to investigate the functionality of ultrathin optical lenses, the measurement accuracy needs to fulfill certain demands. In case of a lens with focal distance of  $f_c = 500 \mu\text{m}$ , the measurement accuracy in beam tracing experiments should be at least  $5 \mu\text{m}$  in the axial direction. Moreover, it should be ensured that the position of object  $A$ , image  $B$  and lens can be determined within this measurement uncertainty. Cameras with a relatively small pixel size and microscope objectives with high magnification are required to detect the image size accurately. In this regard, the numerical aperture (NA) of a lens should be introduced as

$$\text{NA} = n \sin(\alpha_c) = n \sin \left( \arctan \left( \frac{d_a}{2f} \right) \right), \quad (2.18)$$

It is the main technical parameter to determine the lens' performance and it describes the maximum cone angle  $\alpha_c$  of the light emitted from a point source placed in the focus that can be collected by the lens [Zou20]. Using reciprocity arguments, the NA also determines the diffraction limited focal spot size to be  $s = \frac{\lambda}{2\text{NA}}$  [Pan18].

Therefore, to experimentally verify the focal spot size  $s$  of an ultrathin metalens, the numerical aperture of the bulky imaging techniques needs to be larger than the NA from the metalens itself.

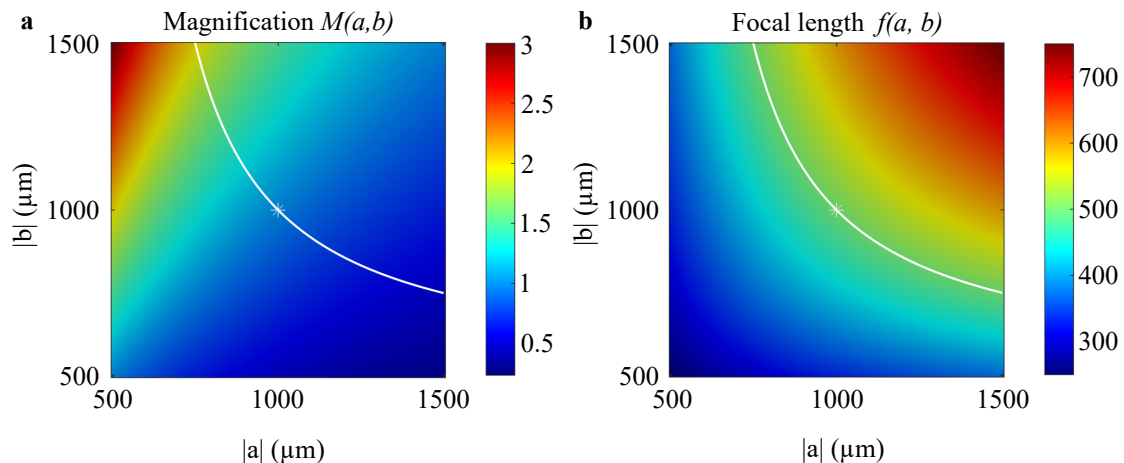


**Figure 2.5: Magnification and focal length for a set of object and image distances.** **a** Magnification  $M = |b|/|a|$  for a set of image and object distances. **b** focal length  $f = \frac{|a||b|}{|a|+|b|}$  for the same set. The white lines correspond to a focal distance of  $f_c = 500 \mu\text{m}$  and the astral data point highlights the experimental configuration for the one-to-one image.

## 2.2 Fundamental concepts to describe plasmonic metasurfaces

In this chapter the transition from conventional optical elements to metasurface optics is conducted. The question arises how such a surface is fabricated and on which design concept it is based. The creation of a metasurface design usually follows a design flow chart [Che20]:

1. A target phase profile is determined. This can be done by an analytical solution in the case of a relatively simple design like a lens or a grating, or by a numerical simulation in the case of a more complex design like an optical hologram.
2. The exact geometry of the nanostructures is determined in part by the wavelength range in which the metasurface is expected to function. Here, commercial software is used to perform a parameter sweep over different geometries by means of numerical simulations.
3. Conceptual implementation of the target phase control with the help of different nanostructure properties (for example by different orientation angles).

Often the last two points are connected, resulting in a library for different nanostructures, which can be applied depending on the required spatial phase value. After the

design has been found, the question of fabrication of the metasurface arises. Over the past decade, planar optics and nanoscience have experienced enormous advances in manufacturing techniques and concepts [Gen17; Wan16]. Nowadays, a plethora of different metasurfaces exist, the functional principle of which depends, among other things, on the material type. Initially, metasurfaces were constructed from resonant plasmonic nanostructures. To understand the operating principle it is mandatory to look at the interaction of light and metal in the frame of the so-called plasma model.

### 2.2.1 The dielectric function of the free electron gas

The interaction of light with metal nanostructures is described in the field of plasmonics [Lee10]. As a pioneer in this field of research one should mention Ebbesen and co-workers, who were the first to describe the extraordinary optical transmission through sub-wavelength hole arrays [Ebb98]. Due to the external electromagnetic field, free electrons in the metal start oscillating. The oscillation is confined in all dimensions because the subwavelength metal nanostructures are placed on a dielectric surface. Then the displacement of the conduction electrons with respect to the positively charged atoms induces a restoring force. This leads to particle plasmon resonances (or localized surface plasmon resonances) that depend on the geometry of the nanostructure, the surrounding medium and the dielectric function of the metal. As in this work, plasmonic antennas made of gold are used, it is essential to discuss the dielectric function of gold. Already in 1972, P. B. Johnson and R. W. Christy provide a comprehensive insight into this topic. They experimentally measured the refractive index  $n$  and the extinction coefficient  $k$  (optical absorption) of gold from reflection and transmission measurements [Joh72]. The vacuum evaporated film had a thickness of only 34.3 nm and it is therefore comparable to the height of plasmonic nanostructures. Results depend to a large extent on the film thickness [Kur13]. The complex refractive index  $\tilde{n} = n + ik$  is directly connected to the complex dielectric constant  $\tilde{\epsilon} = \epsilon_1 + i\epsilon_2$  via  $\tilde{n} = \sqrt{\tilde{\epsilon}}$ , so that  $\epsilon_1 = n^2 - k^2$  and  $\epsilon_2 = 2nk$ . Based on these relations, the measured real and imaginary part of the dielectric constant for Gold is shown for different wavelengths (fig. 2.6). High values of  $\epsilon_2$  in the visible range correspond to a high ohmic losses that indicate a drawback of using noble metals. Ohmic losses can be reduced by choosing a different metal with a large negative real part  $\epsilon_1$  that reduces the penetration depth [Bia12]. Furthermore, the real part  $\epsilon_1$  is negative, which means that the conduction electrons do not oscillate in phase with the external field. This is the reason for the high reflectivity of gold surfaces [Dre02]. These experimental findings were described theoretically by the Drude-Sommerfeld theory [Nov12]. Even though the theory is part of many textbooks, it is worthwhile to take a closer look, as many connections emerge again in this work. The model is based on the assumption that conduction electrons behave as a gas of free electrons interacting with fixed periodically arranged atoms while they oscillate in response to the external electromagnetic field  $\vec{E}_0 e^{-i\omega t}$  [Mai07]. The location of the electron's

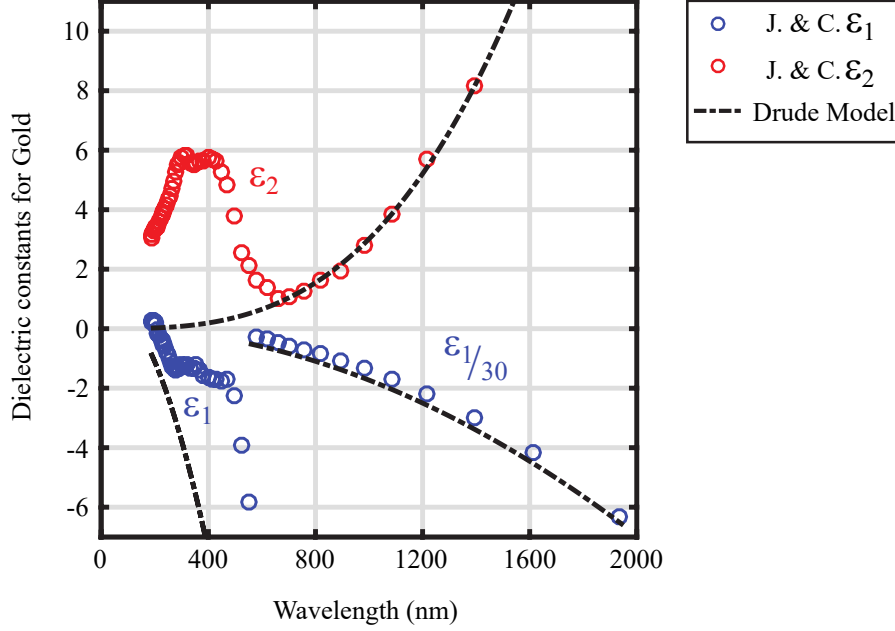


**Figure 2.6: Dielectric constants for Gold as a function of the wavelength according to Johnson and Christy.** Dielectric constants  $\varepsilon_1$  (blue) and  $\varepsilon_2$  (red) measured by P. B. Johnson and R. W. Christy [Joh72]. For  $\varepsilon_1 < -7$  the values are divided by a factor of 30 for better visibility. The black dashed line corresponds to the Drude free-electron theory. It can be seen that the Drude model is a good approximation for wavelengths higher than 660 nm.

charge  $e$  is described by a position vector  $\vec{r}$  so that

$$m_e \frac{\partial^2}{\partial t^2} \vec{r} + m_e \Gamma_a \frac{\partial}{\partial t} \vec{r} = e \vec{E}_0 e^{-i\omega t}. \quad (2.19)$$

The oscillation is damped by collisions and free carrier absorption that are characterized by the phenomenological collision frequency  $\Gamma_a$ . The influence of the band structure (lattice potential) and electron-electron interactions are not taken into account directly. These effects are only included by using an effective optical mass  $m_e$  [Mai07; Olm12]. Furthermore, the differential equation incorporates no restoring force as free electrons are considered. Using the ansatz  $\vec{r}(t) = \vec{r}_0 e^{-i\omega t}$  leads to the particular solution:

$$\vec{r}(t) = \frac{e/m}{\omega^2 + i\Gamma_a\omega} \vec{E}_0 e^{-i\omega t}. \quad (2.20)$$

The microscopic displacement  $\vec{r}$  of an individual electron results in a dipole moment  $\vec{\mu} = e\vec{r}$ . Under the assumption that all conduction electrons with density  $N$  exercise the same movement, the macroscopic polarization is given as  $\vec{P} = N\vec{\mu} = Ne\vec{r}$ . Following eq. (2.20), the polarization yields

$$\vec{P} = \frac{Ne^2/m}{\omega^2 + i\Gamma_a\omega} \vec{E}_0 e^{-i\omega t}. \quad (2.21)$$

It is known from Maxwell's equations that an electric field  $\vec{E}$  causes bound charges to slightly separate and induces a local electric dipole moment. The associated vector field of the electric displacement is defined as

$$\vec{D} \equiv \varepsilon_0 \vec{E} + \vec{P}. \quad (2.22)$$

Inserting eq. (2.21) yields

$$\begin{aligned} \vec{D} &= \varepsilon_0 \left( 1 - \frac{\omega_p^2}{\omega^2 + i\Gamma_a\omega} \right) \vec{E}_0 e^{-i\omega t}, \\ \omega_p^2 &= \frac{Ne^2}{\varepsilon_0 m}. \end{aligned} \quad (2.23)$$

Thereby,  $\omega_p$  is defined as the volume plasma frequency of the free electron gas, which increases with increasing carrier density. The electric susceptibility  $\chi_e$  describes the proportionality between polarization and electric field at low field strength. In general this is a linear complex second order tensor, which can depend on both location and time.

$$\begin{aligned} \vec{P} &= \varepsilon_0 \chi_e \vec{E}, \\ \chi_e &= \varepsilon_r - 1. \end{aligned} \quad (2.24)$$

Using eq. (2.22) and inserting eq. (2.24) yields

$$\vec{D} = \varepsilon_r \varepsilon_0 \vec{E}. \quad (2.25)$$

A comparison to eq. (2.23) reveals the complex frequency-dependent dielectric function of the free electron gas  $\varepsilon(\omega)$ , which consists of real and imaginary part.

$$\begin{aligned} \varepsilon(\omega) &= 1 - \frac{\omega_p^2}{\omega^2 + i\Gamma_a\omega} \\ &= 1 - \frac{\omega_p^2}{\omega^2 + \Gamma_a^2} + i \frac{\Gamma_a \omega_p^2}{\omega^3 + \Gamma_a^2 \omega}. \end{aligned} \quad (2.26)$$

The course of the experimental data for a thin film of Gold can now be fitted by the Drude free electron theory (black dashed line in fig. 2.6). The collision frequency is given as  $\Gamma_a = 1.075 \times 10^{14}$  Hz and the plasma frequency appears to be  $\omega_p = 13.8 \times 10^{15}$  Hz [Nov12]. The Drude-Sommerfeld model describes the dielectric function of gold sufficiently for near infrared wavelengths. However, there are large deviations for higher frequencies in the visible spectrum which come from the response of bound electrons. The reason is that higher energy photons are capable to promote electrons of lower lying bands into the conduction band. The Drude model provides an excellent starting point for the numerical simulation of various arrayed nanostructures, for example rectangular nano-holes or bow-tie slot antennas [Gar05; Guo08]. In order to ultimately describe the spectral resonance properties, commercial software for finite integration time domain algorithms such as CST Microwave Studio are typically used. Hereby, the Drude model is used to describe the frequency dependent dielectric functions of metals [Guo08].

### 2.2.2 The polarization of light and the geometric Pancharatnam-Berry phase

The observation of polarization states is of particular importance for the characterization of the metasurfaces investigated in this thesis, because all of them are polarization sensitive and they partly perform a geometric phase change where the phase is accumulated by space-variant polarization manipulations [Pan56]. This so-called Pancharatnam-Berry phase is a key technology not only for the functioning of countless geometric metasurfaces [Din15; Kar14; Lin14]. Traditionally, the Aharonov-Bohm effect is known as an important realization of the geometric phase in area of quantum mechanics, however, it is also related to many areas including condensed-matter physics, optics, high-energy and particle physics, as well as fluid mechanics, gravity and cosmology [Coh19]. One advantage of this kind of phase manipulation is in its purely geometric origin, which means that there is no need to build up a library for different nanostructure geometries in complex numerical simulations. In this regard, individual meta-atoms are designed to exert certain phases on orthogonal states of polarization. Such elements can then be described by a Jones matrix of a conventional birefringent wave plate which offers an intuitive method to describe the operating principle [Mue17].

#### Jones Calculus

A simple possibility for the mathematical representation and simulation of polarization states in experiments is given by the Jones calculus [Hau80; Sal19]. This formalism describes polarization states by means of a complex amplitude vector, which is commonly normalized to one. A transverse monochromatic plane wave  $E(z,t)$  propagating in  $z$ -direction is denoted as the vector of two perpendicular fields. The Jones vector  $|J\rangle$  represents amplitude and phase of the electric field in the  $x$ - and  $y$ -directions, it does not take into account the propagation in  $z$ -direction nor the time

dependence.

$$\vec{E}(z,t) = \begin{pmatrix} E_{0,x} e^{i(\omega t - kz + \phi_x)} \\ E_{0,y} e^{i(\omega t - kz + \phi_y)} \end{pmatrix} \rightarrow |J\rangle = \begin{pmatrix} E_{0,x} e^{i\phi_x} \\ E_{0,y} e^{i\phi_y} \end{pmatrix} \quad (2.27)$$

A pair of orthogonal Jones vectors forms a complete basis of all fully polarized states. The most important pairs are shown in table 2.1. For convenience, the Dirac bra-ket notation is used. The great advantage of the Jones formalism is the possibility

**Table 2.1: Jones vectors of the basic polarization states.** LHP and LVP: linear horizontal and linear vertical polarization, LDP and LAP: linear diagonal and linear antidiagonal polarization, RCP and LCP: right-circular and left-circular polarization.

Polarization basis	Jones vectors	Basis ket notation
LHP and LVP	$\begin{bmatrix} 1 \\ 0 \end{bmatrix}$ and $\begin{bmatrix} 0 \\ 1 \end{bmatrix}$	$ H\rangle$ and $ V\rangle$
LDP and LAP	$\frac{1}{\sqrt{2}} \begin{bmatrix} 1 \\ 1 \end{bmatrix}$ and $\frac{1}{\sqrt{2}} \begin{bmatrix} -1 \\ 1 \end{bmatrix}$	$ D\rangle$ and $ A\rangle$
RCP and LCP	$\frac{1}{\sqrt{2}} \begin{bmatrix} 1 \\ +i \end{bmatrix}$ and $\frac{1}{\sqrt{2}} \begin{bmatrix} 1 \\ -i \end{bmatrix}$	$ R\rangle$ and $ L\rangle$

to simulate polarization-optical components by two-dimensional Jones matrices  $M$ . Some of the most important optical components and their Jones matrices are listed in table 2.2. These matrices describe the change of a polarization input state  $|j_{\text{in}}\rangle$  by an optical component and result in its output state  $|j_{\text{out}}\rangle = M |j_{\text{in}}\rangle$ .

The comparison of the matrices shown in table 2.2 shows that the Jones matrix of the half-wave plate (HWP) multiplied by  $e^{+i\frac{\pi}{2}}$  looks like that of a mirror. This is a legitimate transformation of the Jones matrix, as the wave plate still describes a delay of  $\pi$  between  $x$ - and  $y$ -components, only that this delay is now applied to only one component and not to both. The mirror analogy is consistent with the expectation, since a HWP rotates a linear input polarization by twice the value of its angle to the fast axis. This means that horizontally and vertically polarized light remains unchanged but right and left circularly polarized waves exchange their helicity. This means that a HWP acts on the Jones vector like a reflection on the  $x$ -axis of the two-component system. The change of polarization by successive insertion of several components (component cascade) into the propagation path of an optical wave that is fully polarized can be ensured by matrix multiplication of the individual Jones matrices. The order of the matrices has to be carefully observed, since matrix multiplication is in general not commutative.

In the appendix there is an example calculation for the polarization change of a component cascade, which will be used later in a similar way to investigate metasurfaces (appendix B).

**Table 2.2: Jones matrices of some important components.**

Optical component	Orientation	Jones matrix
Linear polarizer	x-axis (horizontal)	$M_{\text{hlp}} = \begin{bmatrix} 1 & 0 \\ 0 & 0 \end{bmatrix}$
Linear polarizer	Angle $\phi$ with respect to x-axis	$M_{\text{lp}}(\phi) = \begin{bmatrix} \cos^2 \phi & \sin \phi \cos \phi \\ \sin \phi \cos \phi & \sin^2 \phi \end{bmatrix}$
$\lambda/2$ -wave plate	Fast axis parallel to x-axis	$M_{\text{hwp}} = e^{-i\frac{\pi}{2}} \begin{bmatrix} 1 & 0 \\ 0 & e^{i\pi} \end{bmatrix}$
$\lambda/4$ -wave plate	Fast axis parallel to x-axis	$M_{\text{qwp}} = e^{-i\frac{\pi}{4}} \begin{bmatrix} 1 & 0 \\ 0 & e^{i\frac{\pi}{2}} \end{bmatrix}$
Wave plate with retardation $\varepsilon$	Fast axis parallel to x-axis	$M_{\varepsilon} = e^{-i\frac{\varepsilon}{2}} \begin{bmatrix} 1 & 0 \\ 0 & e^{i\varepsilon} \end{bmatrix}$
Rotation matrix	Angle $\phi$ with respect to initial orientation	$R(\phi) = \begin{bmatrix} \cos \phi & -\sin \phi \\ \sin \phi & \cos \phi \end{bmatrix}$
Rotated component	Angle $\phi$ with respect to initial orientation	$M(\phi) = R(\phi)MR(-\phi)$
Mirror	Normal incidence	$M_{\text{m}} = \begin{bmatrix} 1 & 0 \\ 0 & -1 \end{bmatrix}$

### Stokes parameters and Poincaré sphere

To measure polarization states of electromagnetic waves four intensity parameters, the Stokes parameters, are widely used [Sch07]. Stokes parameters offer the advantage to not only describe fully polarized light but also its unpolarized part. Nevertheless, Jones vectors  $|J\rangle = [E_x, E_y]$  can be converted into Stokes parameters by [Hau80]

$$\begin{aligned}
S_0 &= |E_x|^2 + |E_y|^2 \\
S_1 &= |E_x|^2 - |E_y|^2 \\
S_2 &= 2\text{Re}\{E_x^* E_y\} \\
S_3 &= 2\text{Im}\{E_x^* E_y\}.
\end{aligned} \tag{2.28}$$

The parameter  $S_0$  represents the total intensity of the light wave,  $S_1$  determines the difference between horizontally and vertically linearly polarized light. This fact is also reflected in the value range of the parameters: While  $S_0$  takes only positive values smaller than one, the value range of  $S_1$  (as well as all other parameters) extends from  $-1$  to  $1$ . Parameter  $S_2$  represents the discrepancy between linearly polarized light in  $45^\circ$  direction and in  $-45^\circ$  direction. Finally, the parameter  $S_3$  determines the

difference between right-circular and left-circular polarized fraction. It is helpful to consider some examples for the description of certain polarization states via Stokes parameters:

$$\begin{aligned} S_{\text{LHP}} &= \begin{pmatrix} 1 \\ 1 \\ 0 \\ 0 \end{pmatrix}, \quad S_{\text{LVP}} = \begin{pmatrix} 1 \\ -1 \\ 0 \\ 0 \end{pmatrix}, \quad S_{\text{LDP}} = \begin{pmatrix} 1 \\ 0 \\ 1 \\ 0 \end{pmatrix}, \\ S_{\text{LAP}} &= \begin{pmatrix} 1 \\ 0 \\ -1 \\ 0 \end{pmatrix}, \quad S_{\text{RCP}} = \begin{pmatrix} 1 \\ 0 \\ 0 \\ 1 \end{pmatrix}, \quad S_{\text{LCP}} = \begin{pmatrix} 1 \\ 0 \\ 0 \\ -1 \end{pmatrix}. \end{aligned} \quad (2.29)$$

The polarization ellipse graphically visualizes the path traced by the real part of the electromagnetic field. Any fully polarized state can be converted into its orientation angle  $\psi$  and its ellipticity angle  $\chi$ , which can be calculated from the Stokes parameters by [Sch07]:

$$\psi = \frac{1}{2} \arctan 2(S_2, S_1) + \frac{\pi}{2} \quad \text{with} \quad (0 \leq \psi \leq \pi), \quad (2.30)$$

$$\chi = \frac{1}{2} \arcsin \left( \frac{S_3}{S_0} \right) \quad \text{with} \quad \left( -\frac{\pi}{4} \leq \chi \leq \frac{\pi}{4} \right). \quad (2.31)$$

As an example, fig. 2.7 illustrates how the polarization ellipse is changed by a QWP with its fast axis aligned in  $y$ -direction ( $M_{\text{qwp}}(\pi/2)$ ). RCP light is composed of  $x$ - (red) and  $y$ - component (green) with a  $\pi/2$  phase difference. The  $x$ -component is delayed by a quarter-wave ( $\pi/2$ ) after propagating through the wave plate leading to diagonally polarized light ( $S_{\text{LDP}}$ ).

In addition to the polarization ellipse, there is another useful tool for visualizing the 2D polarization vector space, which proves to be particularly helpful when it comes to the representation of a large number of different polarization states in the space of polarization: the Poincaré or Bloch sphere (fig. 2.7, b). It is a hypothetical sphere placed in the center of a three-dimensional coordinate system whose base is formed by the Stokes parameters and whose volume corresponds to a unit sphere. The equatorial plane is spanned by  $S_1$  and  $S_2$  parameters. This means that all linear states lie in this plane. The upper hemisphere includes all elliptic states with right-handed helicity. At the north pole of the sphere is the RCP state. The lower hemisphere correspondingly includes all left-handed elliptical states, including the LCP state at the southernmost central point. The Poincaré sphere is also capable of

representing unpolarized or partially polarized states, that is, states with a degree of polarization less than one [Sch07]. The degree of polarization  $P$  is the magnitude of the location vector in the coordinate system.

$$P = \frac{\sqrt{S_1^2 + S_2^2 + S_3^2}}{S_0} \quad \text{with: } (0 \leq P \leq 1). \quad (2.32)$$

For the sake of simplicity, in the following only fully polarized states are considered that lie on the spherical surface.

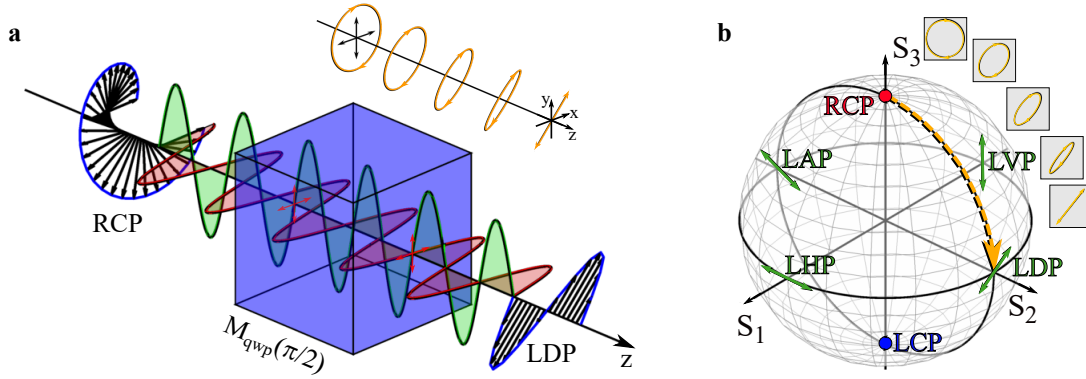


**Figure 2.7: Polarization modulation in real space and polarization space.**

**a** The evolution of the state of polarization of a light beam propagating through a QWP in real space. When the instantaneous electric field forms a right-handed helix in space, so that its point of intersection with a transverse plane rotates in a clockwise sense to an observer facing the source, the polarization is called right-handed. RCP is converted to LCP light after propagating through the QWP. **b** The same polarization modulation is illustrated as a path on the Poincaré sphere (orange arrow).

### The Pancharatnam-Berry phase

Unlike diffractive and refractive elements, the Pancharatnam-Berry phase is not induced by optical path differences but results from a geometrical phase that is accompanied by a space-variant change of polarization [Bie02; Pan56]. Therefore, the phase between two states of polarization  $|\psi_A\rangle$  and  $|\psi_B\rangle$  is described by phase of their scalar product  $\arg(\langle\psi_A|\psi_B\rangle)$ . Pancharatnam's theorem can be restated by considering three different polarization states,  $|\psi_A\rangle$ ,  $|\psi_B\rangle$  and  $|\psi_C\rangle$ , of which  $|\psi_A\rangle$  and  $|\psi_B\rangle$ , as well as  $|\psi_B\rangle$  and  $|\psi_C\rangle$  are in phase (fig. 2.8). Now it can be shown that  $|\psi_A\rangle$  and  $|\psi_C\rangle$  are generally not in phase, but  $|\psi_C\rangle$  is in phase with a state  $|\psi_{A^*}\rangle$  which has the same polarization state as  $|\psi_A\rangle$ , but differs from  $|\psi_A\rangle$  by a geometric

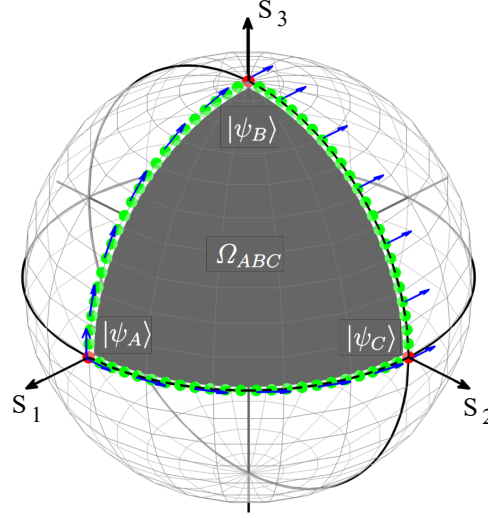


**Figure 2.8: Non-transitivity of the phase difference among three polarization states.** A set of polarization states  $|\psi_A\rangle = |H\rangle$ ,  $|\psi_B\rangle = |R\rangle$ , and  $|\psi_C\rangle = |D\rangle$  (red dots) corresponds to a Pancharatnam-Berry phase that is determined by half the solid angle of the geodesic triangle  $\Omega_{ABC}/2 = \pi/4$  spanned by the points on the Poincaré sphere. The geometric phase change can also be obtained by applying the holonomy of the closed path on the sphere (green dots) yielding a parallel transported vector (blue arrows) that deviates by an angle of  $\pi/2 = \Omega_{ABC}$  from the initial vector [Coh19].

phase difference described by half the area of the geodesic triangle [Ara92; Coh19]:

$$\arg(\langle \psi_A | \psi_A \rangle) = \frac{\Omega_{ABC}}{2}. \quad (2.33)$$

To understand the underlying concept, it is convenient to use the Jones calculus in order to illustrate the manipulation of polarization by different wave plates first (fig. 2.9). To do this, the respective Jones matrices from table 2.2 are used and the final states of polarization are converted into Stokes parameters (eq. (2.28)) which can be plotted on the Poincaré sphere.<sup>1</sup> The first two Poincaré spheres show the usual change in polarization of a QWP and a HWP for a horizontal linear input polarization. For different rotation angles of the QWP, it covers the two circular polarization states, traversing the surface of the sphere in the form of the

<sup>1</sup> In literature often also the so-called Mueller calculus is used as a generalization of the Jones calculus and to manipulate directly the Stokes parameters of light [Sal19].

number eight (a). The HWP rotates the linear input polarization by twice the angle that lies between its fast axis and the input polarization (b). This behavior changes significantly for a right-circular input polarization. The QWP can now generate any linear state of polarization (c; this case is demonstrated in detail in fig. 2.7). The HWP transforms the circular input polarization into its circular cross-polarization regardless of the rotation angle (d). Thus, it becomes clear that an optical element whose phase delay is exactly half a wavelength always entails a transfer to the opposite spin state than that of the input polarization. This transformation is exactly the same as that caused by geometric metasurfaces at every single nanostructure (compare fig. 2.2c) [Din15; Kho16; Lin14]. Therefore, subwavelength meta-atoms are in demand that can be understood as individual half-wave plates, so that the response of the geometric metasurface, which contains the phase information, is mostly to be expected in the circular cross-polarization. Anisotropic building blocks like metal nanoantennas or dielectric nanofins can serve both as a set of birefringent elements that feature different optical properties for two perpendicular states of polarization [Min18]. To achieve high conversion between the two circular polarization states, it is preferable that the phase difference between the complex transmission coefficient for light polarized along the long axis ( $t_l$ ) and the short axis ( $t_s$ ) of the nanoantenna equals  $\pi$  at the design wavelength [Che20]. Since the helicity of the incident circular polarization is reversed on a subwavelength scale an abrupt interfacial phase discontinuity is introduced by the metasurface [Hua13a]. Much of the research is concerned with simulations using the finite difference time domain (FDTD) method to search for appropriate nanostructure geometries so that they really cause the desired retardation of the phase. The polarization conversion efficiency varies between 0% and 100%, depending on whether the retardation is an even or odd multiple of  $\pi$  [Kho14].

It remains to be clarified which exact path the polarization change takes on the Poincaré sphere (d, dashed red line). By using a wave plate with variable retardation (see table 2.2), the path on the Poincaré sphere can be traced (e, shown here for eight specific angles of rotation  $\pi/8, \pi/4, \dots, \pi$ ). The phase delay ranges from 0 to  $\pi$  and is indicated by the color brightness. Now it becomes clear how the spatially variable phase change within a metasurface proceeds: Different rotation angles of the variable wave plate correspond to the orientation angles of single meta-atoms since the anisotropic geometry of the meta-atom is rotated as well. In general, the Jones matrix  $M_{\text{ns}}$  of an anisotropic nanostructure that is rotated by the angle  $\theta$  is given as [Che20]

$$\begin{aligned} M_{\text{ns}} &= R(\theta) \begin{bmatrix} t_l & 0 \\ 0 & t_s \end{bmatrix} R(-\theta) \\ &= \frac{t_l + t_s}{2} \begin{bmatrix} 1 & 0 \\ 0 & 1 \end{bmatrix} + \frac{t_l - t_s}{2} \begin{bmatrix} \cos(2\theta) & -\sin(2\theta) \\ \sin(2\theta) & \cos(2\theta) \end{bmatrix}, \end{aligned} \quad (2.34)$$

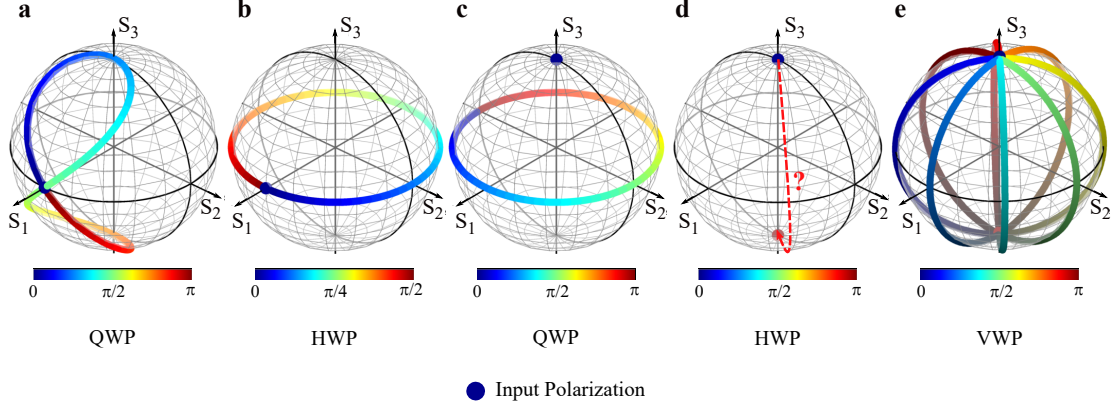


**Figure 2.9: Polarization modulation by different wave plates illustrated on the Poincaré sphere.** **a** Illustration of the polarization modulation by a QWP for input LHP light (blue point) and for different rotation angles of the wave plate. **b** Corresponding polarization modulation by a HWP. **c-d** Change of polarization by QWP and HWP for input polarization that is changed to LCP. **e** Polarization modulation by a wave plate with a variable phase retardation at eight specific rotation angles. The phase retardation ranges from 0 to  $\pi$  and it is encoded by the color brightness.

where  $R(\theta)$  is the rotation matrix (see table 2.2). Considering an incident LCP/RCP wave  $\vec{E}_{\text{LCP/RCP}}$ , the transmitted electromagnetic field can be written as:

$$\begin{aligned} \vec{E}_T &= M_{\text{ns}} \cdot \vec{E}_{\text{LCP/RCP}} \\ &= \frac{t_l + t_s}{2} \vec{E}_{\text{LCP/RCP}} + \frac{t_l - t_s}{2} \vec{E}_{\text{RCP/LCP}} e^{i\sigma 2\theta}, \end{aligned} \quad (2.35)$$

where the first term denotes circular co-polarization, and the second term represents circular cross-polarization of the scattered wave. The latter provides an additional Pancharatnam-Berry phase of  $\sigma 2\theta$ , where  $\sigma$  is  $+1$  for LCP and  $-1$  for RCP incident light [Che20]. A nanostructure embodies an ideal half-wave plate functionality with maximum cross-polarization transmission amplitude for  $|t_l| = |t_s|$  and  $\arg(t_l) - \arg(t_s) = \pi$ . The same relative phase change between two nanostructures with a relative rotation angle of  $\pi/8$  can be calculated by the half enclosed area on the Poincaré sphere in fig. 2.9e [Pan56]. Since the full surface of a unit sphere corresponds to the value  $4\pi$ , the phase difference between two adjacent rotation angles can be given as  $\pi/4$ . In this way, the geometric phase change can cover the full  $2\pi$  range with nanostructures that are continuously rotated from 0 to  $\pi$ . This concept of wavefront manipulation provides a broadband performance since the phase is purely geometric and does not suffer from dispersion effects. A detailed example calculation

for the meta-atoms used in this work is given later (see section 3.2.1).

### 2.3 Plasmonic metalens for linear image formation at infrared wavelength

As an example of how the introduced concepts can be applied, the linear image formation with a metalens working at infrared frequency is demonstrated. This example also illustrates some of the experimental challenges. A similar experiment was performed in 2012 by Chen and co-workers with a cylindrical metalens [Che12]. The phase modulation of the lens is based on the presented principle of the Pancharatnam-Berry phase. Accordingly, each plasmonic nanoantenna should function like a half-wave plate with an individual angle of rotation (see fig. 2.10). The antenna-geometries are designed to have a focal length of  $f_0 = 500 \mu\text{m}$  at a design wavelength of  $\lambda_d = 1200 \text{ nm}$ . With regard to eq. (2.10), the spatially variable rotation angles of the nanoantennas wrapped into radial zones ranging from 0 to  $2\pi$  are given by a modulo operation:

$$\theta_{\text{ML}}(x,y) = \frac{1}{2} \text{mod} \left( \frac{2\pi}{\lambda_d} \left( \sqrt{x^2 + y^2 + f_0^2} - f \right), 2\pi \right). \quad (2.36)$$

The upright L-shaped hard-edge aperture is used as a bright object placed at  $z = -1000 \mu\text{m}$  in front of a plasmonic metalens ( $z = 0 \mu\text{m}$ ) in order to enable an upside down real image formation after propagating through the metalens. Note that the image is inverted again through the microscope objective and a tube lens. The setup is illustrated in fig. 2.10. To enable the required operation as a convex lens, the polarization optics (P and  $\lambda/4$ ) are adjusted as described in eq. (B.1). In this way, only light with the reversed helicity is measured on the camera and the image appears to be background-free. The axial positions of aperture and lens can also be verified under the illumination with white light (fig. 2.10a, c).

To realize the one-to-one image according to the image equation (eq. (2.17)), the object distance should be  $|a| = 2f$ . However, optical transmission measurements showed a localized surface plasmon polariton resonance at a wavelength of  $\lambda_o = 1175 \text{ nm}$ . While using this operating wavelength, the axial position of the sharp aperture image is shifted to  $z = -840 \mu\text{m}$  (fig. 2.10b). It must be taken into account that the imaging optics (MO and  $L_2$ ) can shift the camera image depending on the used wavelength. An axial shift of  $160 \mu\text{m}$  is therefore assumed. For clarity, the axial positions of the acquired images are shown as red dots on the optical axis (fig. 2.10). A ray tracing experiment demonstrates that the incident light is focused at  $z = 680 \mu\text{m}$  (fig. 2.10d) and an upright image of the L-shaped aperture can be detected at  $z = 1260 \mu\text{m}$  (fig. 2.10e). The measured magnification was  $M = 1.13$ . At first sight, these results seemed unexpected. Since it was ensured that the distance between metalens and real object is  $1000 \mu\text{m}$ , one should expect a magnification of the image of  $M = 1$ . However, this phenomenon can be explained by the wavelength

dependency of the metalens phase profile (see eq. (2.10)). The metalens that was designed for a wavelength of 1200 nm is now operated at a shorter wavelength of 1175 nm and this results in an increased focal length of  $f'_0 \approx 520 \mu\text{m}$ . The assumed shift of  $160 \mu\text{m}$  explains why the focal plane is not located at  $520 \mu\text{m}$  but at  $680 \mu\text{m}$ . Accordingly, the measured image distance is  $b = 1100 \mu\text{m}$ , which corresponds to a magnification of  $M = 1.10$ . As a result, it is demonstrated that the image formation with plasmonic metalenses can be predicted by simple geometrical optics.

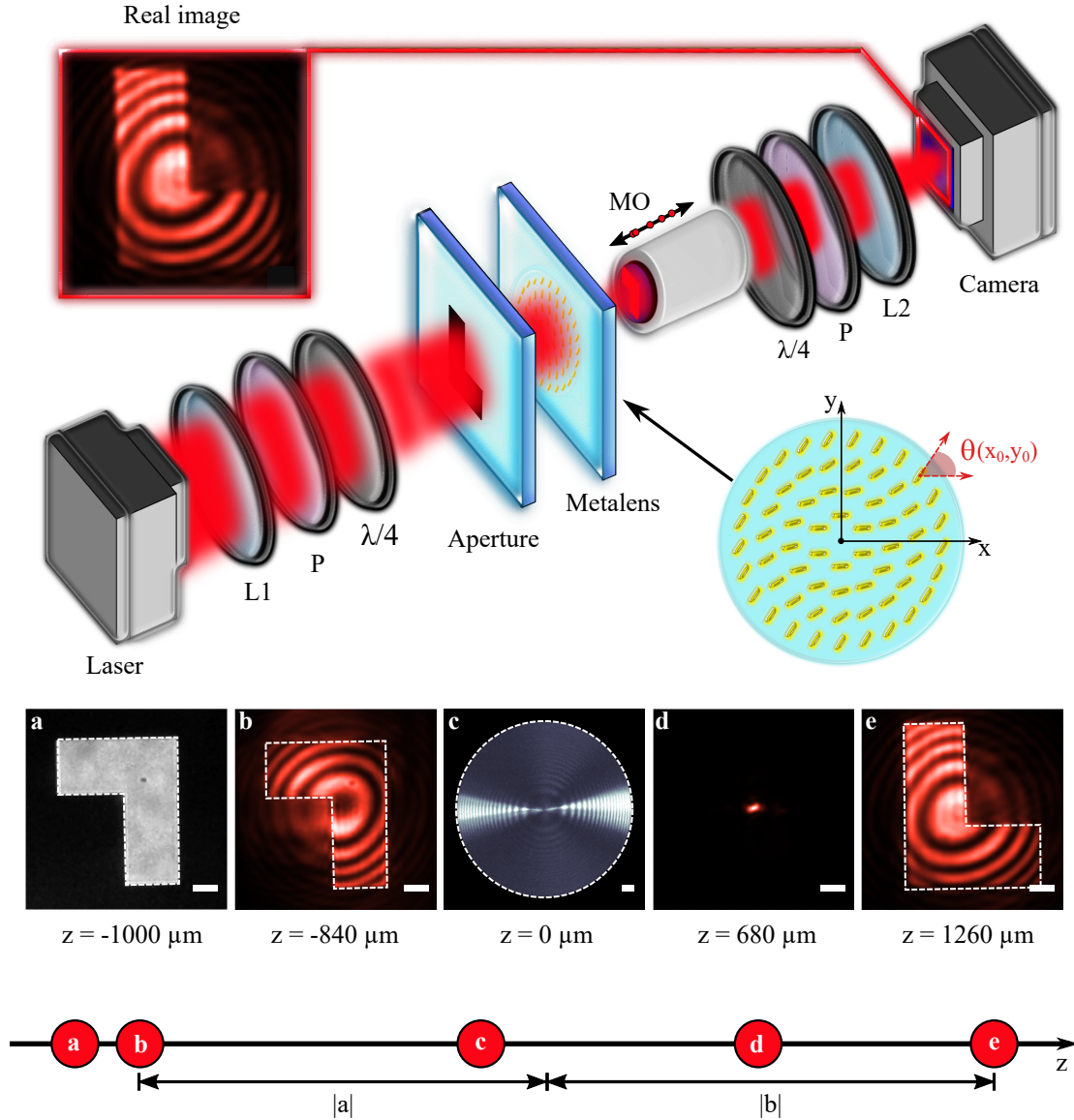


**Figure 2.10: Plasmonic metalens for imaging at infrared frequency.** The experimental setup is shown schematically. The insets show a schematic image of metalens as well as the measured real image (false color) at the camera position. Acronyms:  $\lambda/4$ , quarter waveplate; L, lens; P, polarizer; MO, microscope objective. **a** The L-shaped aperture is imaged with white light at  $z = -1000 \mu\text{m}$ . **b** The same aperture is imaged under the illumination with laser light (1175 nm) at  $z = -840 \mu\text{m}$ . **c** An image of the metalens is detected at  $z = 0 \mu\text{m}$ . **d** The laser light behind the metalens is converging to a minimum spot at  $z = 680 \mu\text{m}$ . **e** The upright real image of the aperture is formed at  $z = 1260 \mu\text{m}$ . White scale bars correspond to a width of  $20 \mu\text{m}$ .

## 2.4 The nonlinear lens in a ray optics picture

The image formation by a lens is one of the most basic and important optical principles. It can be easily described by the Gaussian lens equation that is a part of many introductory textbooks in optics [Hec02]. As the linear optical component heavily relies on the basic electromagnetic principle of superposition, its functionality is easily understood in a ray optics picture (see section 2.1). From a scientific point of view, the question rises how the image formation is affected if these linear principles are violated and the regular glass lens is replaced with one made of a nonlinear material. This is a novel approach, while most works on nonlinear imaging are in general either linked to experiments where people execute a nonlinear process on the object or on the image of an object [Bar13]. Thus we imagine a nonlinear lens, where the phase accumulation is accompanied by a nonlinear process as depicted in fig. 2.11. For this

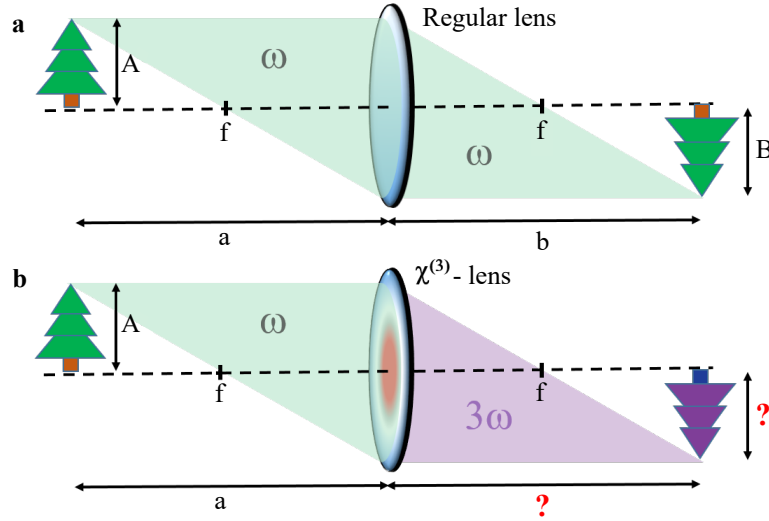


**Figure 2.11: Schematic concept and characteristics of nonlinear metalenses.**

**a** Schematic illustration of the image formation with a regular lens. **b** Intuitive realization of schematic image formation with a nonlinear lens made of  $\chi^3$ -material.

thought experiment, the fundamental wave incorporates the object information and the nonlinear image formation on the other side of this  $\chi^3$ -lens deviates from the linear regime. Even if it is practically possible to manufacture refractive nonlinear crystals with curved surfaces, the phase matching conditions will massively impede the experimental realization. The intrinsic properties of metasurfaces make them attractive candidates for the realization of such device [Alm16b]. In contrast to conventional bulky optics, the nonlinear response of subwavelength-thick metasurfaces

does not rely on the phase matching condition [Wan17], instead it is governed by localized geometric resonances [Kra18; Li17b; Sai19].

## 2.5 Conclusion

In this chapter the operation of a conventional thin lens, which is based on refractive optics, is discussed. It can be illustrated by geometrical optics. In this way the optical path through a lens and the associated focusing of the light beam can be described using Snellius' law of refraction. The resulting Lensmaker's equation describes how the focal length of a refractive lens can be adjusted by the radii of curvature. Thus, convex lenses with positive focal length and concave lenses with negative focal length can be realized. The effect of the lens on an incident light beam can be translated into the corresponding lens-like phase profile. To realize the same phase manipulation by an ultrathin planar lens, a spherical phase retardation is required. Now, based only on the phase distribution of the lens, the conventional Gaussian lens equation can be derived using Fermat's principle. This equation describes the image formation of both conventional lenses and metalenses in the linear regime.

In the following, the fundamental concepts of plasmonic metasurfaces are discussed. They are based on the array-like arrangement of metallic meta-atoms, which are smaller than the wavelength of light. In this work, all plasmonic nanoantennas were made of gold. They can show a distinct resonance in the collective motion of conduction band electrons in a certain spectral range. The plasmon resonance is due to the confinement of the electron gas to a small spatial region and is determined by the explicit geometry and dielectric functions of the metal and the surrounding environment. As an example, the dielectric function of gold is derived based on the Drude free electron theory and compared with experimental data investigated by P. B. Johnson and R. W. Christy. In order to design plasmonic metasurfaces explicitly, the derived dielectric function can be used as an input parameter in commercial software like CST microwave studio. In this way, the nanometric geometry (length, width, height, and periodicity) of the nanoantennas can be determined.

To encode a phase manipulation in a metasurface, for example, one makes use of the concept of geometric phase manipulation. The Pancharatnam-Berry phase describes the accumulated spatially variant phase change that occurs when the polarization state is changed. It can be shown for a circular input polarization that nanoantennas whose phase retardation corresponds to half a wavelength perform a local phase change corresponding to twice the rotation angle. Accordingly, Pancharatnam-Berry metasurfaces provide an abrupt phase manipulation that does not result from propagation effects. This dispersionless phase control offers the advantage of producing ultrathin metasurfaces which are highly versatile in application and intuitive to use, making them an ideal candidate for integrated optical elements.

As an example, a plasmonic metalens consisting of gold nanoantennas with C2

rotational symmetry is presented, which can be used to image an L-shaped aperture object that is illuminated at circularly polarized infrared light. For this purpose, an experimental setup is realized and operated at the plasmon polariton resonance of 1175 nm. It is experimentally shown that the image formation in the circular cross-polarization is completely described by the Gaussian lens equation.

A central question of this work has been presented at the end of this chapter. It is the question of how the image formation would change if a conventional linear lens is replaced by a nonlinear lens. It turns out that nonlinear metalenses are the ideal candidate for the experimental realization, which will be pursued in the following chapters.

## CHAPTER 3

---

### Nonlinear plasmonic metasurfaces for image formation and further applications

---

The abrupt phase change of light at metasurfaces provides high flexibility in wave manipulation without the need of accumulation of a propagating phase through dispersive materials. In the linear optical regime, one important application field of metasurfaces is imaging by planar metalenses, which enables device miniaturization and aberration correction compared to conventional optical microlens systems. With the incorporation of nonlinear responses into passive metasurfaces, optical functionalities of metalenses are anticipated to be further enriched, leading to completely new applications areas. In this chapter imaging with nonlinear metalenses is demonstrated that combine the function of an ultrathin plasmonic lens with simultaneous frequency conversion [Sch18]. Imaging of real objects with near infrared light is experimentally demonstrated with such nonlinear metalenses, while the image appears in the second harmonic signal of visible frequency range. Furthermore, the functionality of these nonlinear metalenses can be modified by switching the handedness of the circularly polarized fundamental wave, leading to either real or virtual nonlinear image formation. Nonlinear metalenses do not only enable infrared light imaging through a visible detector but also have the ability to modulate nonlinear optical responses through ultrathin metasurface device while the fundamental wave remains unaffected, which offers the capability of nonlinear information processing with novel optoelectronic devices. In the following sections the fundamentals of nonlinear optical processes are discussed in general and then it will be worked out to what extent these can be generated and exploited by nonlinear plasmonic metasurfaces. These will provide the basis for the understanding of nonlinear optical metasurfaces. Furthermore, concepts for the nonlinear phase manipulation are introduced that take up again the geometrical manipulation already presented.

#### 3.1 Introduction to nonlinear harmonic generation processes

Nonlinear optical processes occur due to a modification of the optical properties of a material in the presence of light at high intensities [Boy20]. It should be noted that at this point only parametric processes are considered, where the quantum-mechanical state of the material remains unchanged. In this case, the material response that is

characterized by the macroscopic polarization  $\vec{P}(t)$  varies not in a linear demeanor with the applied optical field  $\vec{E}(t)$ . In the linear regime, the bulk polarization of

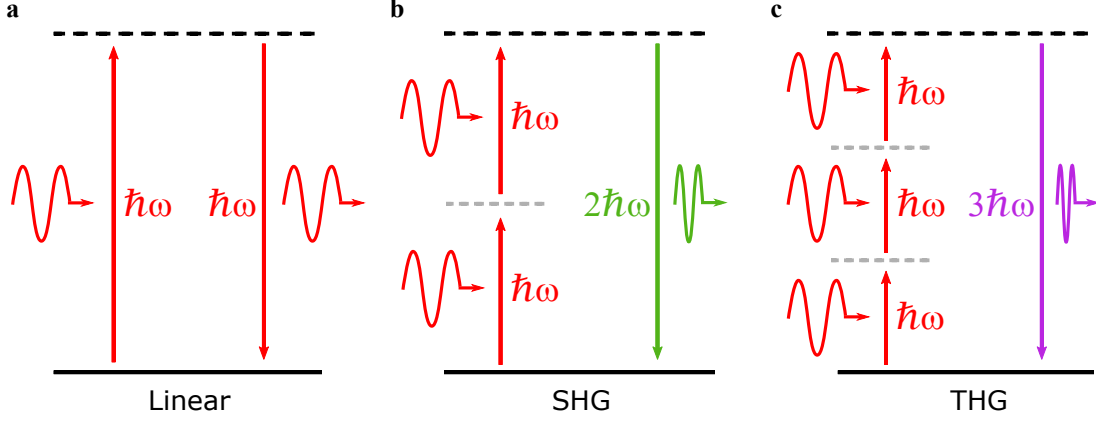


**Figure 3.1: Schematic energy level diagrams of linear and nonlinear processes.** Photons at identical fundamental frequencies  $\omega$  interact within a nonlinear process that result in the generation of new frequencies  $n\omega$ . The solid and dashed lines represent electronic and virtual levels for the excitation of the material polarization, respectively. **a** Linear interaction, **b** Second harmonic generation (SHG), **c** third harmonic generation (THG).

the material is outlined in eq. (2.24), where the induced dipole oscillates with the same frequency as the electric field and each molecule can be characterized as a harmonic oscillator (see fig. 3.1). By taking into account larger optical field strengths, this model idea is no longer valid and nonlinear terms must be taken into account. This can be done by expanding the polarization  $\vec{P}(t)$  as a generalized Taylor series expansion in  $\vec{E}(t)$ :

$$\begin{aligned}\vec{P} &= \varepsilon_0 \chi^{(1)} \vec{E}^1(t) + \varepsilon_0 \chi^{(2)} \vec{E}^2(t) + \varepsilon_0 \chi^{(3)} \vec{E}^3(t) + \dots \\ &= \vec{P}^{(L)} + \vec{P}^{(NL)},\end{aligned}\tag{3.1}$$

where  $\chi^{(i)}$  denote the  $(i + 1)$ th order nonlinear susceptibility and refers to a tensor of rank  $(i + 1)$ . The polarization can be separated in a linear and a nonlinear part.

In comparison to the linear case (eq. (2.25)), the vector field of the electric displacement  $\vec{D}$  (eq. (2.22)) now takes into account the nonlinear part of the polarization

$$\vec{D} = \varepsilon_0(1 + \chi^{(1)})\vec{E}(t) + \vec{P}^{(NL)}.\tag{3.2}$$

Starting from a second derivative identity ("curl of curl"), Maxwell's equations in the absence of charges ( $\rho = 0$ ) and currents ( $\vec{J} = 0$ ) are used to derive the vector Laplace operator of the electric field:

$$\begin{aligned}\nabla \times (\nabla \times \vec{E}) &= \nabla \underbrace{(\nabla \cdot \vec{E})}_{=0} - \Delta \vec{E} \\ &= -\frac{\partial}{\partial t} \nabla \times \vec{B} = -\mu_0 \frac{\partial^2}{\partial t^2} \vec{D}\end{aligned}\tag{3.3}$$

Inserting eq. (3.2) and using  $(1 + \chi^{(1)}) = \varepsilon_r = \tilde{n}^2$  as well as  $\frac{1}{c_0^2} = \mu_0 \varepsilon_0$  leads to the nonlinear wave equation for a loss-free and isotropic nonlinear medium

$$\left( \Delta - \frac{\tilde{n}^2}{c_0^2} \frac{\partial^2}{\partial t^2} \right) \vec{E} = \mu_0 \frac{\partial^2}{\partial t^2} \vec{P}^{(\text{NL})}.\tag{3.4}$$

In comparison to the linear wave equation, the electric field  $\vec{E}$  is now driven by the nonlinear polarization  $\vec{P}^{(\text{NL})}$ , which will act as a source of new frequencies of the electromagnetic field. The generation of new frequencies will be demonstrated briefly using the example of a medium with quadratic nonlinear susceptibility that is pumped with two plane waves. Therefore, the nonlinear polarization is given by

$$\vec{P}^{(\text{SHG})} = \varepsilon_0 \chi^{(2)} \vec{E}^2.\tag{3.5}$$

It is now deducible that materials which show an inversion symmetry (centrosymmetric materials) cannot exhibit any second-order response [Kau12]. Because of the inversion symmetry, a change of the sign of the applied electric field has to result in a change of the sign of the induced polarization, too. Then, by comparison with eq. (3.5) the equation  $-\vec{P}^{(\text{NL})} = \varepsilon_0 \chi^{(2)} (-\vec{E})(-\vec{E})$  is invalid if  $\chi^{(2)} \neq 0$  [Boy20].

Furthermore, for all solutions to the nonlinear wave equation the principle of superposition does not apply. It follows that a plane wave of the form  $\vec{E}_j = \vec{A}_j \cos(\omega_j t - k_j z + \zeta_j)$  must be considered as real part of a generally complex function as

$$\vec{E}_j = \frac{1}{2} \left( \vec{A}_j e^{i(\omega_j t - k_j z)} + \vec{A}_j^* e^{-i(\omega_j t - k_j z)} \right)\tag{3.6}$$

with  $\vec{A}_j = \vec{A}_j e^{i\zeta_j}$  and  $\vec{A}_j^*$  denotes the complex conjugated (*c.c.*) form. Now the nonlinear medium is pumped with two monochromatic plane waves so that  $j \in \{1, 2\}$ .

The sum of both waves is squared in order to derive the nonlinear polarization

$$\begin{aligned}
P^{(\text{NL})} = \frac{1}{2}\varepsilon_0\chi^{(2)} & \left( |\tilde{A}_1|^2 + |\tilde{A}_2|^2 \right. \\
& + \frac{1}{2}(\tilde{A}_1^2 e^{2i(\omega_1 t - k_1 z)} + c.c.) + \frac{1}{2}(\tilde{A}_2^2 e^{2i(\omega_2 t - k_2 z)} + c.c.) \\
& + (\tilde{A}_1 \tilde{A}_2 e^{i((\omega_1 + \omega_2)t - (k_1 + k_2)z)} + c.c.) \\
& \left. + (\tilde{A}_1 \tilde{A}_2^* e^{i((\omega_1 - \omega_2)t - (k_1 - k_2)z)} + c.c.) \right)
\end{aligned} \tag{3.7}$$

The terms in eq. (3.7) refer to different frequencies of the nonlinear polarization. Once these terms are applied in the nonlinear wave equation (eq. (3.4)), they will lead to electromagnetic waves which oscillate at the same frequency. The first line of eq. (3.7) describes the optical rectification, which causes a static polarization in the material. The terms in the second line show the frequency doubling of the two input frequencies. This frequency conversion is called second harmonic generation (SHG) or frequency doubling. In lines three and four the processes of sum frequency (SFG) and difference frequency generation (DFG) are outlined. However, since the latter are not relevant in the context of this work, a detailed discussion shall be refrained and the reader is referred to relevant literature [Boy20]. All of these quadratic interactions are lowest order nonlinear processes that depend on the second-order susceptibility of the material. The  $\chi^{(2)}$ -interactions are usually weak, SHG, for example, normally needs complex tailor-made crystals with low-symmetry unit cells. Popular, commercially available examples are crystalline barium borate ( $\beta$ -BaB<sub>2</sub>O<sub>4</sub>) or lithium niobate (LiNbO<sub>3</sub>) [Bar19].

However, third order nonlinear processes are also an important basis for this work. Considering a monochromatic plane wave  $\tilde{E}(t) = E e^{-i\omega t} + c.c.$  incident on a nonlinear  $\chi^{(3)}$ -medium results in a nonlinear polarization of the form [Boy20]

$$\tilde{P}^{(\text{NL})} = \varepsilon_0\chi^{(3)} \left( (E^3 e^{-3i\omega t} + c.c.) + 3EE^*(E + E^*) e^{-i\omega t} \right). \tag{3.8}$$

The first term is oscillating at a frequency  $3\omega$ , which describes the third harmonic generation (THG). The energy level diagrams for all processes that are discussed within the scope of this work are illustrated in fig. 3.1. All are photon mixing processes that can be described by means of energy and momentum conservation:

$$\begin{aligned}
\text{SHG: } \hbar\omega + \hbar\omega &= 2\hbar\omega \quad \text{and} \quad \vec{k}(\omega) + \vec{k}(\omega) = \vec{k}(2\omega), \\
\text{THG: } \hbar\omega + \hbar\omega + \hbar\omega &= 3\hbar\omega \quad \text{and} \quad \vec{k}(\omega) + \vec{k}(\omega) + \vec{k}(\omega) = \vec{k}(3\omega).
\end{aligned} \tag{3.9}$$

During the generation of the second harmonic, two photons of frequency  $\omega$  interact

and produce a photon of double frequency  $2\omega$ , while during the generation of the third harmonic three photons of frequency  $\omega$  interact, which then leads to the generation of a photon of triple frequency  $3\omega$ . These photon interactions will later play an important role in the operation of nonlinear metalenses at different harmonic processes.

It should be mentioned that nearly all here mentioned nonlinear processes can be implemented simultaneously with only a single dielectric gallium arsenide (GaAs) metasurface generating new frequencies that span the ultraviolet to NIR spectral range [Liu18]. However, which nonlinear processes are applied is generally decided by the symmetry of the optical system [She84]. This implies the application of the selection rules, which are discussed in the following section.

### 3.1.1 Selection rules for harmonic generation in nonlinear optics

The conventional selection rules are based on the transformation properties of the nonlinear susceptibility tensors. Thus, statements are made about the feasibility of nonlinear optical processes at crystals with certain symmetries and for certain input polarizations. These rules then determine, depending on the order of the nonlinear process, whether it is allowed or forbidden [Bha72]. Based on recent advances in nonlinear optics, these concepts are completely transferable to the symmetry of artificial atoms in metasurfaces [Li15]. With respect to the application in the context of a geometric phase manipulation, especially the selection rules for a circular input polarization are relevant. These can be summarized as follows:

Based on the selection rules for circularly polarized harmonic generation, fundamental waves (FW) propagating perpendicular to the metasurface consisting of meta-atoms with  $m$ -fold rotational symmetry can only generate harmonic orders of

$$n = jm \pm 1. \quad (3.10)$$

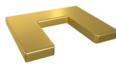


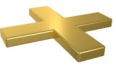
Here,  $j$  is an arbitrary integer,  $m$  characterizes the rotational symmetry of the artificial nanostructure and the  $\pm$  sign coincides to co- or cross-polarized harmonic generation, respectively [Che14a; Li15]. All centro-symmetric atoms, for example, are characterized by an even rotational symmetry such that  $m = 2, 4, 6, \dots$  and the right-hand side of the equation thus always yields an odd number. Consequently, the generation of even harmonic processes (SHG, FHG, ...) does not occur at atoms with inversion symmetry (see also section 3.1). Furthermore, the observation of SHG specifically is only allowed for structures with  $C_1$  or  $C_3$  rotational symmetry. The mentioned popular bulk materials for SHG may serve as an analogy. Barium borate ( $\beta$ -BaB<sub>2</sub>O<sub>4</sub>) and lithium niobate (LiNbO<sub>3</sub>) belong to the cyclic group  $C_3$ , which also

lacks inversion symmetry and refers to a trigonal crystal system.<sup>1</sup> For an incident fundamental wave of circular polarization the phases of the nonlinear polarizability are shown for different harmonic generation orders and various rotational symmetries (table 3.1). It can be seen that the phase depends on the order of the nonlinear process and the helicity of the input circular polarization, but, once both are defined, not on the rotational symmetry. In this context, the rotational symmetry only makes a statement about the feasibility of the nonlinear process.

Furthermore, meta-atoms with a rotational symmetry ( $m \geq 3$ ) feature an isotropic response in the linear optical regime [Sai19], which means that the linear signal from the metasurface remains unaffected.

It should be noted at this point that the utilization of C3 meta-atoms provides all the advantages for the SHG in Pancharatnam-Berry phase plasmonic metasurfaces.

**Table 3.1: Comparison of nonlinear geomtric Pancharatnam-Berry phases for different harmonic generation orders and meta-atom rotational symmetries.** The order of the nonlinear process ( $n = 1, 2, 3, 4$ ) and the rotational symmetry of the meta-atom (C1, C2, C3, C4) determines the phase that accumulates during the harmonic generation process and depends on the orientation angle of the meta-atom. The factor  $\sigma$  describes the circular polarization state of the light. A similar table can be found in [Li17b].

Harmonic order	$\sigma(n\omega)$	C1	C2	C3	C4
					
$n = 1$	+				
	−	$2\theta\sigma$	$2\theta\sigma$		
$n = 2$	+	$1\theta\sigma$			
	−	$3\theta\sigma$		$3\theta\sigma$	
$n = 3$	+	$2\theta\sigma$	$2\theta\sigma$		
	−	$4\theta\sigma$	$4\theta\sigma$		$4\theta\sigma$
$n = 4$	+	$3\theta\sigma$		$3\theta\sigma$	
	−	$5\theta\sigma$			

<sup>1</sup> In literature both structures are represented by the Hermann-Mauguin notation  $3m$ , which is equivalent to the Schoenflies notation  $C_{3v}$ .

### 3.2 Tailor nonlinear optical wavefront control

The following chapter deals with the question of how to tailor nonlinear optical wavefronts with nanostructures. The focus is on the dimensional tailoring of the light field using nonlinear Pancharatnam-Berry phase, which is an extension of the geometric phase from the linear regime.

#### 3.2.1 Space variant nonlinear Pancharatnam-Berry phase

In this work, a metasurface design with threefold rotational symmetry is fabricated, from which SHG should be observed only in the cross-circular state of polarization. Furthermore, the nonlinear polarizabilities for the harmonic generation can be described as [Li15]

$$P_{\theta, \pm\sigma, \sigma}^{n\omega} \propto e^{i(n \pm 1)\sigma\theta}, \quad (3.11)$$

where  $\sigma = \pm 1$  corresponds to the combination of incident and transmitted circular state of polarization and  $\theta$  is the orientation angle of the nanostructure. For a right circularly polarized input beam with spin state  $\sigma$ , which will be partly converted to the left circularly polarized SHG output beam with spin state  $-\sigma$  (RCP to LCP), the sign is positive and vice versa [Kon14]. Hereby, the exponent  $\phi = (n \pm 1)\sigma\theta$  represents the Pancharatnam-Berry phase factor, which only depends on the rotation angle of the m-fold rotational symmetric meta-atom. Based on the before mentioned selection rules, maintaining the same circular state of polarization is forbidden in this case [Li15]. An abrupt phase change occurs, which is governed by  $P_{\theta, -\sigma, \sigma}^{2\omega}$  that has a phase term of  $\varphi = \pm 3\theta$  [Li15].

As an calculation example, the graphical illustration of the nonlinear Pancharatnam-Berry phase change  $\varphi_{\text{ex}}$  of two nanoantennas with C3 rotational symmetry is shown in the following. The two structures differ only by their orientation angles. The Poincaré sphere is used to illustrate the change in the polarization space (fig. 3.2). Both antennas are impinged by RCP light  $(0, 0, 1)$  at normal incidence. As already shown in fig. 2.9, if the phase retardation corresponds to that of a HWP, the change of polarization runs along a meridian from one pole to the other reaching the left circularly state of polarization at the south pole  $(0, 0, -1)$ . In this case, a nonlinear SHG process is additionally performed at the C3 structure, which means that the phase delay has to match  $\frac{1}{2}$  of the second harmonic wavelength. The exact course can be traced by observing an increasing phase retardation from 0 to  $\pi$  with the help of the Jones Calculus. The meridians along which the polarization changes occur are arbitrary and depend only on the orientation angles. Since for the phase change only the relative change of the angles to each other is decisive, one meridian is chosen by the path traversing through the linear horizontal state at  $(1, 0, 0)$ . In the model of the wave plates this would correspond to a HWP with an orientation angle of  $\pi/4$ . As this is not just a graphical illustration but also

a graphical calculation method, the second polarization state on the equator (red dot) is defined as  $(\sqrt{0.8}, \sqrt{0.2}, 0)$ , which complies with the orientation angle of the nanostructure  $\theta = \frac{1}{3} \arctan \sqrt{0.2/0.8} \approx 8.86^\circ$ . The revealed phase equals half of the surface area which is encompassed by the loop on the sphere. (colored in gray).

Another way to graphically calculate the geometric phase is to determine the angle between an arbitrary oriented, initial surface vector and the parallel transported vector on the surface of the sphere (blue) [Coh19]. Half of the angle between both vectors yields the gathered geometric phase. In this case, the angle between the two blue vectors at  $(0, 0, 1)$  is calculated to be  $\approx 53.13^\circ$ . Half of this angle is  $\approx 26.57^\circ$  corresponding to a Pancharatnam-Berry phase of  $\varphi_{\text{ex}} \approx 0.15\pi$ . This phase angle corresponds exactly to three times the orientation angle of the structure:  $3 \cdot 8.86^\circ \approx 26.57^\circ$ .

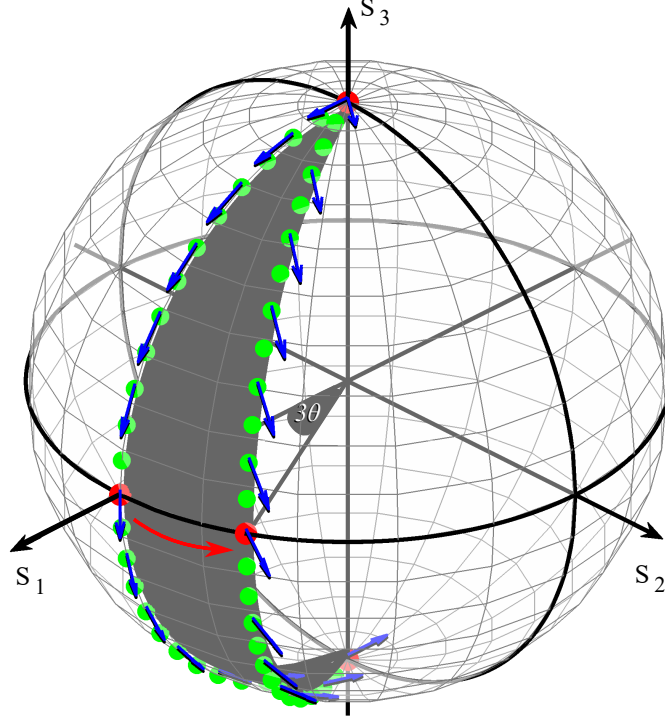


**Figure 3.2: Graphical calculation method to determine the Pancharatnam-Berry phase on the Poincaré sphere.** RCP incident light  $(0, 0, 1)$  is converted into LCP light  $(0, 0, -1)$  after propagating through the nonlinear metasurface. The path on the sphere is related to the rotational angle of the C3 nanostructure (illustrated on the right side) and to the reference path which traverses in this case through the horizontal linear polarization. The grey area surrounded by this path as well as the angle between an initial and a parallel transported vector on the sphere are twice the Pancharatnam-Berry phase change between two C3 nanoantennas twisted against each other by an angle of  $\theta$ .

### 3.3 From linear to nonlinear plasmonic metalenses

Conventional optical focusing, which can be classified by refractive and diffractive effects, is limited either by the surface topography or the refractive index contrast dictated by the materials or the fabrication processes. Metamaterials have shown the potential to relax some constraints in the control of light propagation, enabling new or improved functionalities such as invisibility cloaking [Erg10], and sub-diffraction-limited super-imaging [Fan05]. A sophisticated manipulation of both phase and amplitude of light [Liu14] can be realized by designing the geometries and orientation angles of meta-atoms on planar metasurfaces [Arb15; Che12; Hua13a; Hua13b; Ni12;

Yu11]. In this way, both plasmonic and dielectric metalenses with diverse optical functionalities have been demonstrated [Arb16; Cam16; Kho16; Ni13a; Shc15]. One example are dual-polarity metalenses that act as either convex or concave lenses depending on the circular polarization state of the light [Che13; Che12]. The underlying mechanism of such dual-polarity lenses results from a spin-dependent Pancharatnam-Berry phase [Ber87; Bom02; Mar06; Pan56]. Meanwhile a plethora of optical effects using Pancharatnam-Berry phase metasurfaces have been successfully demonstrated, including three-dimensional optical holography [Hua13b; Lar12; Ni13b], generation of vortex beams [Hua12; Yu11], laser beam shaping [Che14b; Ker15], multifocal lenses [Che15], integrated dynamical phase lenses [Ke16; Yin17], or helicity-dependent multifunctional lenses [Wen16a; Wen16b]. The concept of geometric Pancharatnam-Berry phases has been recently applied for tailoring the nonlinear optical responses of plasmonic metasurfaces [Seg15]. Nonlinear spin-orbit interactions [Li15] and nonlinear optical holography [Ye16] have been demonstrated through harmonic generation processes. Plasmon-enhanced nonlinear processes were also proposed for superresolution applications [Sim14]. While the conversion efficiency of such nonlinear devices is generally too low for practical applications, Lee et al. demonstrate that the second harmonic generation (SHG) can be strongly enhanced by coupling the plasmonic resonances of the meta-atoms with intersubband transitions in semiconductor quantum wells, paving the way for high-efficiency nonlinear metasurfaces [Lee14]. There are other strategies to increase the efficiency, for instance, using different material platforms. Strong THG has also been introduced from Fano-resonant Si-based metasurfaces leading to an enhancement factor of  $> 10^5$  compared to bulk material [Yan15]. Gallium arsenide based dielectric metasurfaces for SHG are reported, which show an enhancement factor of  $10^4$  compared to the unstructured film [Liu16]. The advantage by using nonlinear optics with resonant dielectric nanostructures is that it grants a 3D volume that is not restricted to interfaces and thus may lead to higher conversion efficiencies due to Fabry-Perot effects. However, so far there is no dielectric high-efficiency metasurface for the nonlinear regime, which is able to spatially control the phase at the same time. Meanwhile, nonlinear plasmonic metalenses based on four-wave mixing and third harmonic generation have been introduced [Alm16a; Alm16b]. However, those metalenses rely on the dispersion control of the individual meta-atoms, which introduces more complexities and phase uncertainties in the design and device fabrication. Furthermore, the question remains whether such nonlinear metalenses can be used for nonlinear optical imaging of objects and not only for relative simple focusing of Gaussian beams.

### 3.4 Imaging through nonlinear plasmonic metalens using second harmonic generation

Here, a nonlinear metalens for nonlinear light focusing and imaging is designed and experimentally demonstrated. The nonlinear metalens acts like a regular lens but with the difference that it only controls the beam propagation of the nonlinear signal, which is simultaneously generated when the light from the object interacts with the metalens. The propagation of the fundamental light remains unaltered.

For demonstration purpose, the concept of the nonlinear Pancharatnam-Berry phase for SHG from meta-atoms with three-fold (C3) rotational symmetry is used. Based on the symmetry selection rules, SHG from a C3 meta-atom has opposite circular polarization compared to that of the fundamental wave (section 3.1.1). By controlling the orientation angle of the meta-atom, the local phase of SHG can be continuously controlled over the entire  $2\pi$  range. By assembling the C3 meta-atoms into a configuration that resembles the phase profile of a lens for the SHG wavelength, helicity dependent nonlinear beam focusing and nonlinear imaging by using second harmonic generations is realized at visible wavelengths.

The concept of the imaging with a nonlinear metalens is schematically shown in fig. 3.3. Light from an object at the fundamental wavelength is collected by the metalens, partially converted to the second harmonic wavelength and imaged to an image plane, which is determined by the focal length and the distance of the object to the lens. The functionality of an optical lens can be realized by a suitable spatially variant phase that is simultaneously added to the nonlinear signal generated at each meta-atom on the surface. For a meta-atom with C3 rotational symmetry, a nonlinear phase of  $3\sigma\theta$  is introduced to the SHG wave, where  $\sigma = \pm 1$  represents the left and right circular polarizations (LCP and RCP) and  $\theta$  is the orientation angle of the meta-atom section 3.2.1. The required spatial phase distribution for a converging lens is given by

$$\varphi(r) = -k_0(\sqrt{f^2 + r^2} - |f|), \quad (3.12)$$

where  $r$  is the radial distance from the lens axis of the metalens,  $f$  is the focal length of the lens in air and  $k_0 = \frac{2\pi}{\lambda_{\text{SHG}}}$  is the free-space wave vector, which corresponds to the second harmonic wavelength in contrast to the previously derived formula (eq. (2.10)). Another difference is the specification of the focal length as magnitude. The reason lies in the geometric phase, which changes the sign of the phase depending on the incoming circular polarization state and thus can encode both a convex and the concave lens. Accordingly, the phase distribution is translated into the orientation angle of the C3 meta-atom by  $\theta = \frac{\varphi}{3\sigma}$ . The metalens is designed to have a diameter of 300  $\mu\text{m}$ , whereas the C3 meta-atoms are aligned in polar coordinates on concentric rings with a spacing of 500 nm.

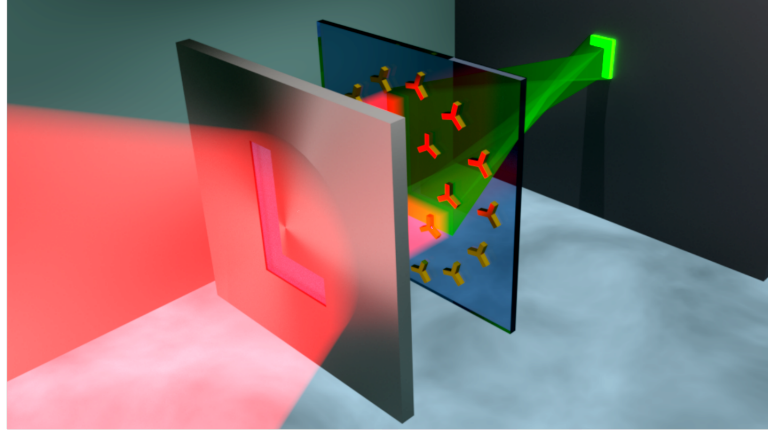


**Figure 3.3: Schematic concept of the imaging with a nonlinear metalens.**

An upright L-shaped aperture is illuminated at infrared fundamental wave. The Aperture is imaged at visible wavelength on a screen with the help of the nonlinear metalens consisting of C3 nanoantennas.

#### 3.4.1 Nanofabrication of plasmonic metalens

A set of different plasmonic metalenses with different focal lengths ( $f_a = 100 \mu\text{m}$ ,  $f_b = 200 \mu\text{m}$ ,  $f_c = 500 \mu\text{m}$ ) is fabricated by using standard electron beam lithography (fig. 3.4a-f). For that, a 150 nm poly-methyl-methacrylate (PMMA) resist layer is spin-coated on ITO coated glass substrate and baked on a hotplate at  $150^\circ\text{C}$  for 2 minutes to remove the solvent. The meta-atoms are patterned in the resist by using standard electron beam lithography (EBL), subsequent deposition of 2 nm chromium as an adhesion layer and 30 nm gold, followed by a lift-off procedure using acetone.

Aperture objects that will be used later as real objects are fabricated with the help of standard electron beam lithography and etching into a 100-nm-thick chromium layer. An L-shaped aperture is  $100 \mu\text{m}$  in width and  $120 \mu\text{m}$  in height.

In fig. 3.5, the design parameters for the nonlinear metalenses are shown. Each C3 meta-atom is composed of three single nanorods rotated by 120 degrees. The length of each nanorod is designed to be 130 nm. In order to verify the quality of the nanofabrication, an image processing software is developed, which is capable to analyze the statistical length distribution of the fabricated C3 meta-atoms. The program imports SEM images and convert them into binary images which depend on a certain threshold. Furthermore, structures can be identified, localized and fitted

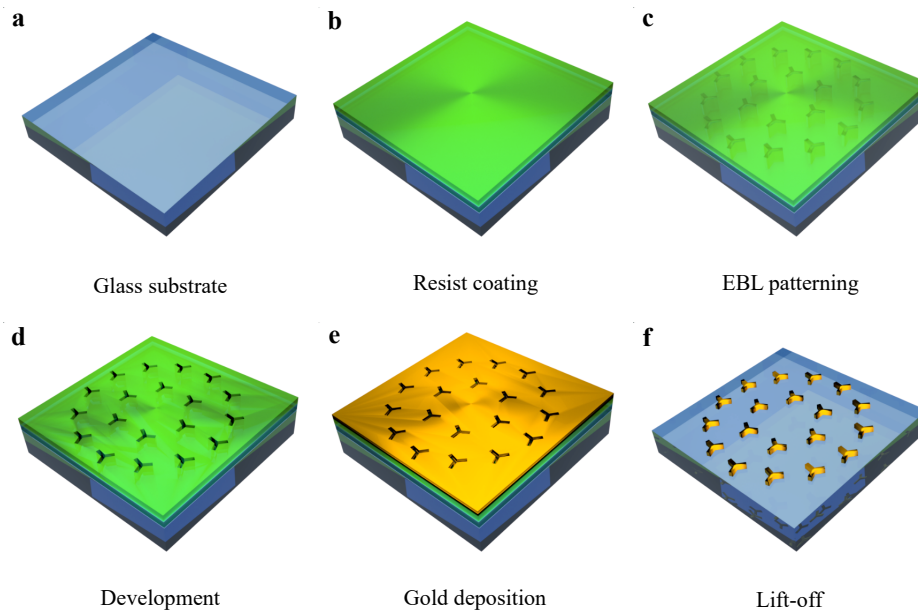


**Figure 3.4: Fabrication process of the nonlinear plasmonic metalens.** Schematic images of the fabrication process that includes **a** cleaning of the glass substrate, **b** spin-coating of PMMA resist layer, **c** EBL patterning, **d** developing, **e** deposition of a 30 nm gold layer, and **f** lift-off procedure.

to individual C3 objects by using the Nelder-Mead algorithm. Thus, meaningful statistics are generated, which include the statistical length distribution. In fig. 3.5 b and c, the length distribution of one SEM image with over 1000 C3 meta-atoms is investigated exemplary. The distribution clearly verifies that the length's mean value is between 135 and 136 nm, which means that the fabricated nanorods are longer than specified in the design. This deviation explains the slightly red-shifted transmission spectra resonance, which is described in the next section.

### 3.4.2 Optical characterization

First, the linear transmission spectra of the lens is measured to determine the resonance wavelength of the localized plasmonic mode of the meta-atoms (fig. 3.6). The far-field characterization setup consists of a Bruker Vertex 70 spectrometer to perform Fourier-transform infrared spectroscopy (FTIR) and a Bruker Hyperion 1000 IR-microscope, which is equipped with a knife-edge aperture that can be used to investigate exclusively the small area of the metasurface [Bla11]. Light from the metasurface is collected in transmission mode by a Schwarzschild microscope objective ( $\times 36 / 0.5$ ) and focused onto a liquid nitrogen cooled Mercury-Cadmium-

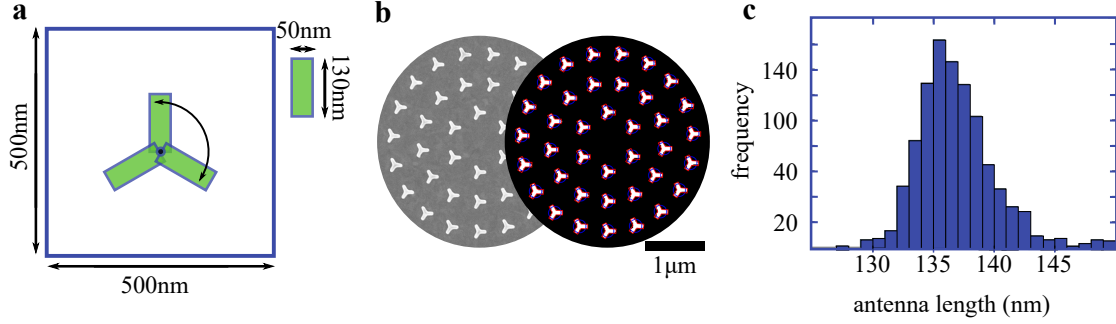


**Figure 3.5: C3 meta-atom size analysis.** **a** Geometric design for the C3 meta-atoms. The SEM image in **b** is analyzed with image processing techniques to determine the statistical length distribution and length deviation (shown in **c**) of the fabricated structures from the design.

Telluride (MCT) detector. All transmission spectra were divided by the reference spectrum of a pure glass substrate to provide the ratio of the transmittance output  $T$ .

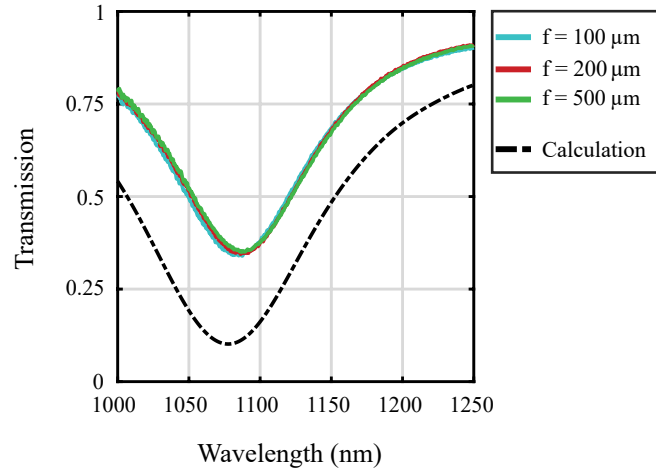


**Figure 3.6: Measured localized surface plasmon polariton resonance.** Measured transmission spectra of the metalens with a focal length of 500  $\mu\text{m}$ . The simulation predicts a localized surface plasmon polariton resonance at a wavelength of 1064 nm, whereby the measured resonance dip is slightly shifted to 1085 nm.

Compared to the design wavelength of 1064 nm the resonance dips are slightly red-shifted to a resonance wavelength of approximately 1085 nm, which is due to a small discrepancy of the fabricated meta-atom geometry from the target design

(fig. 3.5).

Although the dispersionless characteristics of the nonlinear Pancharatnam-Berry phase enable the SHG beam focusing and imaging across a broad range of wavelengths, the efficiency and the focal lengths vary for different fundamental wavelengths. The spectral response of SHG from the C3 metalens in forward direction is obtained for illumination with circularly polarized femtosecond laser pulses (fig. 3.7a). A circular polarizer is used before the fundamental wave is focused on the metalens by a regular lens ( $f_{L1} = 75$  mm). Any unwanted nonlinear signal is filtered out by a long-pass filter. The SHG signal from the metalens is collected by a microscope objective and the circular co- and cross-polarization can be investigated with the help of a circular polarization analyzer (see appendix B). Finally, a 4- $f$  configuration is used to couple the SHG signal into a spectrometer while the fundamental light is blocked by a short-pass filter. As expected, the SHG signal with the same polarization as that of the fundamental wave disappears as this process is forbidden by the nonlinear selection rule due to the C3 rotational symmetry of the meta-atoms [Li15]. In comparison, the SHG signal with cross-polarization shows a strong signal (fig. 3.7b). It should be noted that the maximum SHG signal for a fundamental wavelength between 1105 and 1125 nm is stronger than that at the resonant wavelength of 1085 nm. This redshift is a result of the resonance that measures the wavelength dependent strength of the far-field enhancement, while the nonlinear conversion is sensitive to the near field enhancement [Zul11].

To determine the SHG efficiency, the signal at a specific SH wavelength is integrated which leads to the total number of counts  $C_{\text{SHG}}$ . For this purpose, the efficiency of the spectrometer components (camera, grating) and the used filters must be taken into account as a correction factor  $\eta_{\text{corr}}(\lambda_{\text{SHG}}) \approx 0.5$ . Thus, the power  $P_{\text{SHG}}$  reads:

$$P_{\text{SHG}} = \frac{C_{\text{SHG}}}{t_{\text{int}} \eta_{\text{corr}}} \frac{hc}{\lambda_{\text{SHG}}}, \quad (3.13)$$

where  $t_{\text{int}} = 1$  s denotes the integration time of the spectrometer. The efficiency is then estimated by dividing  $P_{\text{SHG}}$  by the total incident power  $P_0 = 26$  mW. From the measured SHG signal strength a conversion efficiency in the order of  $10^{-12}$  is estimated. Much larger values might be attainable by combining the plasmonic metalens with highly nonlinear materials [Lee14; Li17b].

### 3.4.3 Second harmonic focusing with nonlinear plasmonic metalens

Next, the focusing behavior of the metalenses for the second harmonic signal in forward direction is experimentally investigated. Note that there is a comparable SHG emission in backward direction, which was not investigated in these measurements. In the experiment, the incident circularly polarized femtosecond (fs) laser beam from an optical parametric oscillator is generated by using a linear polarizer and a QWP.

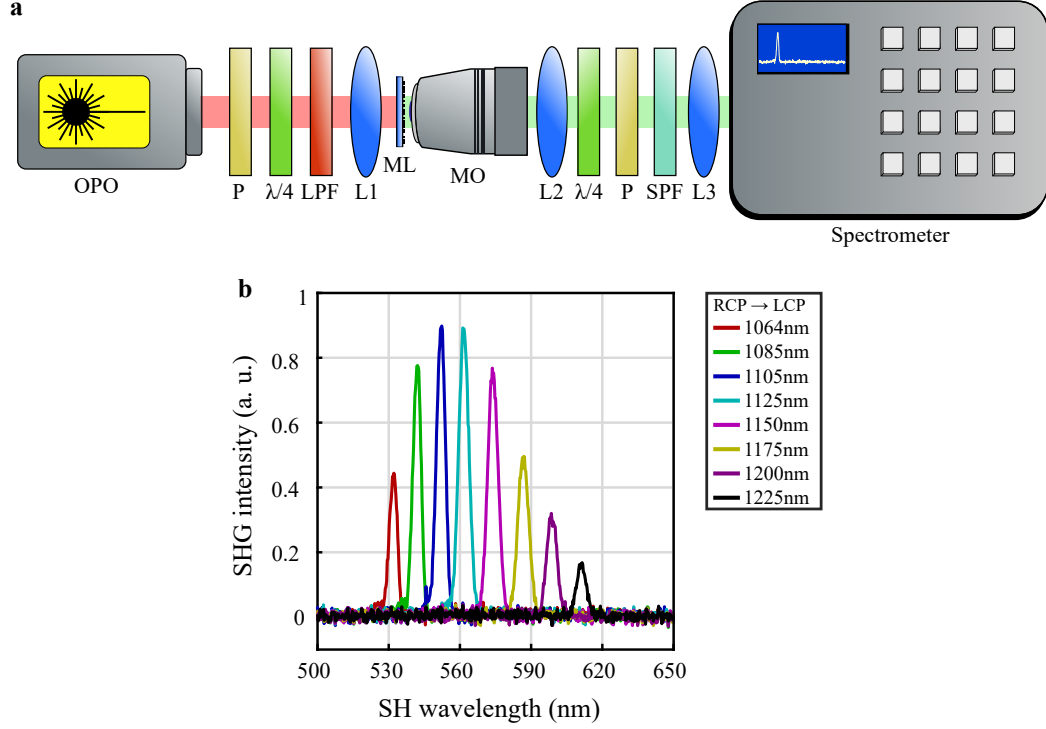


**Figure 3.7: Nonlinear spectroscopy measurement of SHG intensity** **a** Experimental setup for nonlinear spectroscopy measurement. Acronyms:  $\lambda/4$ , quarter waveplate; L1-L3, lenses; LPF, long-pass filter; ML, metalens; MO, microscope objective lens; OPO, optical parametric oscillator; P, polarizer; SPF, short-pass filter. **b** Measured SHG signals for different right circularly polarized fundamental wavelengths with the maximum SHG intensity for RCP-LCP conversion between 1105 and 1125 nm. The SHG response disappears for RCP-RCP.

Then the fs laser of the desired wavelength is focused by an achromatic condenser lens ( $f = 500$  mm) to a spot size that is marginally larger than  $\approx 300 \mu\text{m}$  to ensure that the full numerical aperture of the metalens is used. The laser repetition rate is 80 MHz, the pulse duration  $\sim 200$  fs and the used average power is  $\sim 75$  mW. The metalens is illuminated at normal incidence and the SHG signal is collected by an infinity corrected microscope objective ( $\times 10 / 0.25$ ). The collected light is subsequently filtered using a short-pass filter. To measure the spin state of transmitted SHG signal, a second QWP and a polarizer behind the microscope objective is added. A tube lens ( $f_T = 200$  mm) is used to image the nonlinear signal onto the ultra-low noise sCMOS camera (Andor Zyla 5.5). By changing the position of the microscope objective along the optical axis, different planes perpendicular to the propagation direction are

imaged onto the camera. For the fundamental wave with RCP state, the metalens is designed to work as a convex lens with positive focal length for the SHG signal while the fundamental wave remains unaffected (fig. 3.8). For the fundamental wavelength

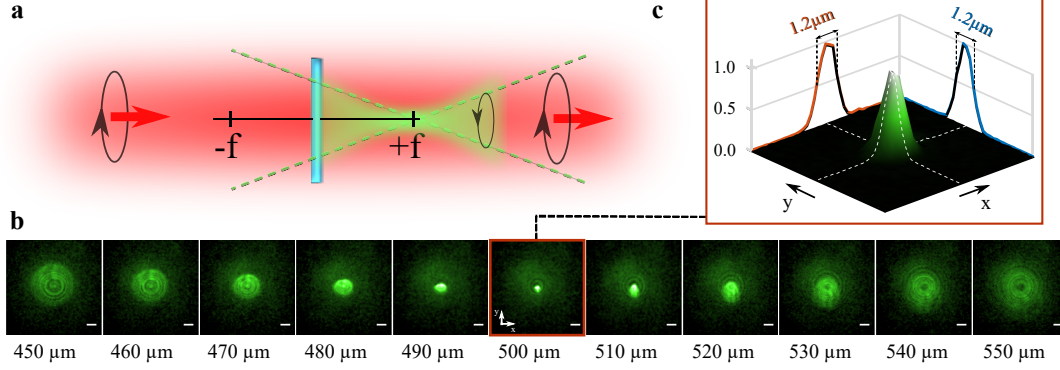


**Figure 3.8: SHG Measurement of the beam propagation in focal region.** **a** Schematic of the measurement: A right circularly polarized incident beam with a wavelength of 1085 nm and a power of 75 mW is used. The converted left circularly polarized SHG signal is measured in the real focal region while the fundamental wave remains unaffected. **b** Measured SHG intensity distribution for the nonlinear metalens with  $f = 500 \mu\text{m}$  at different transverse planes in the focal region. The white scale bars correspond to a length of  $10 \mu\text{m}$  and the SHG is encoded in false color on a logarithmic scale for better visibility. **c** Interpolated surface plot of the SHG focal spot on an area of  $75 \mu\text{m}^2$ . The focal spot size for this metalens is  $1.2 \mu\text{m}$ .

of 1085 nm, the SHG light is focused at the designed focal length of  $500 \mu\text{m}$  (Figure 2b). As for all the measurements, the point of reference for the beam propagation on the optical axis is the position of the nonlinear metalens ( $z = 0$ ). The Gaussian FWHM is measured to  $1.2 \mu\text{m}$  for each direction. To characterize the precise spot size, this measurement was done with a different microscope objective ( $40\times / 0.60$ ) and a tube lens with a focal length of  $f_T = 150 \text{ mm}$  (compare section 2.1.3).

Reversing the circular polarization state of the incident fundamental wave leads to a concave phase profile with negative focal length. All phase distributions which can be realized in this way are in principle linear distributions for a diameter of  $300 \mu\text{m}$  (compare fig. 2.3). In further measurements of the SH focusing, the dual polarity of the nonlinear metalens is verified by measuring the real and virtual focal planes in dependence on different wavelengths. Therefore, SHG focusing planes are measured for all three metalenses at fundamental wavelengths of 1064 nm, 1085 nm, and 1150 nm (see fig. 3.9). From a qualitative point of view, it can be found that all focal lengths are close to the design value with only a small mismatch. Note that for the focal spot measurement, a regular lens with  $f = 200 \text{ mm}$  is utilized in front of the metasurface while in fig. 3.8 a lens with  $f = 500 \text{ mm}$  is used. For the tube

lens in front of the camera a local length of 100 mm is employed. The discrepancy between the measured and designed focal lengths possibly arises from the fact that the sample position is not perfectly placed into the beam waist of the fundamental beam. Although the phase profile is designed for a SHG wavelength of 532 nm, the nonlinear focusing phenomena can be observed for all the three incident fundamental wavelengths. The SHG waves at wavelengths of 532 nm, 542.5 nm and 575 nm are focused to nearly the same focal planes, as the dispersion in the focal length of the metalenses is negligible within this bandwidth. However, from the formula of the phase profile eq. (3.12) the focal length is expected to change with the wavelength. Including the calculation, the focal length for using 542.5 nm is approximately 10  $\mu\text{m}$  smaller than for the design wavelength of 532 nm.

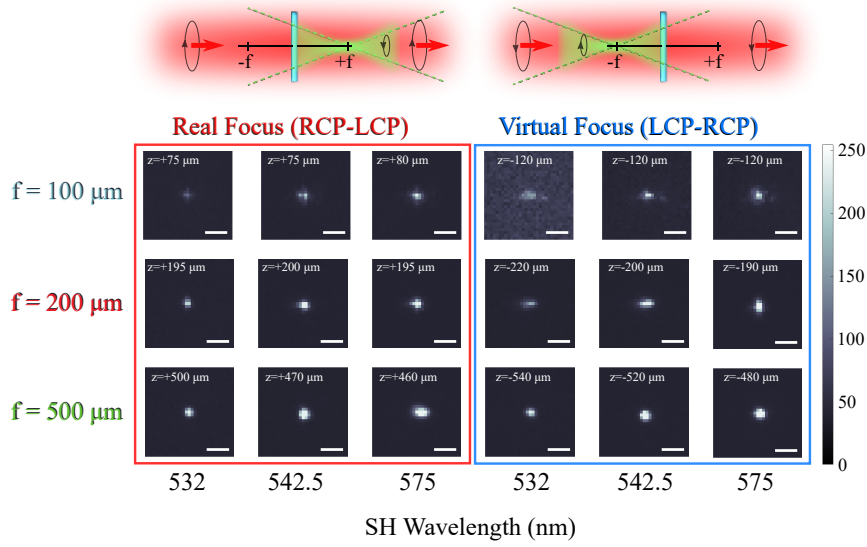


**Figure 3.9: Measured SHG intensity distribution at the focal plane.** Real and virtual focal spot planes are shown for three metalenses with the design focal lengths (100, 200, 500)  $\mu\text{m}$ . Depending on the circular polarization state of the fundamental light, the metalenses act either as positive or as a negative lens for the SHG, therefore forming a real or virtual image. In the case of right circularly polarized incident beam (red framed box), the converted left circularly polarized SHG signal is measured in the real focal plane which is located in the positive direction of propagation (value given in each image). For the reversed case (blue framed box), the virtual focal plane can be obtained in front of the metalens causing the beam to diverge in direction of propagation. All focal planes are examined for the design wavelength, the resonant wavelength and the measured wavelength with the highest SHG efficiency (scale bar equals 50  $\mu\text{m}$  on the camera screen).

#### 3.4.4 SHG imaging of real objects

In the following sections, it will be investigated whether the fabricated plasmonic lenses can also be used to actually image real objects in the second harmonic signal. Thereby it shall be clarified how a possible image formation can be described and whether it is governed by the traditional laws from geometrical optics.

##### Experimental setup

For demonstrating the imaging abilities of the nonlinear metalens, an L-shaped aperture object is fabricated as well as a double slit aperture. These apertures are used as bright objects for the fundamental wave to provide sufficient power for the nonlinear process. For the following experiments the metalens with a focal length of  $f = 500 \mu\text{m}$  is selected. The schematic of the imaging setup at the example for the L-shaped aperture is shown in fig. 3.10. The average power of the laser is set to  $\sim 100 \text{ mW}$ . In the experiment, the nonlinear metalens and the chromium apertures are facing each other. By illuminating the aperture with a right circularly polarized Gaussian beam at  $1085 \text{ nm}$  wavelength, the metalens is expected to work as a convex lens generating a real image of the aperture. First the aperture is placed at the object distance  $a = -f$  in front of the metalens. By adjusting the imaging plane of the microscope objective, the inverted SHG image of the L-shaped aperture can be retrieved with the magnification  $\Gamma = -1$  at a certain image distance  $b = 2f$  to the metalens. Note that the imaging system to the camera, which consists of the objective and the tube lens, also inverts the image, hence the real image after the nonlinear metalens is upright (in contrast to the white light image). Compared to the linear optical case, where the object and image distance is related by  $-a = b = 2f$ , it can be found that the nonlinear image formation is not governed by this relation. Hence, the traditional lens equation from linear optics cannot be applied to the nonlinear imaging case. To further study the nonlinear imaging properties of the metalens, a beam propagation method in the nonlinear regime is used.

##### A short introduction to the beam propagation method in the nonlinear regime

To numerically simulate the image formation created by a nonlinear metalens, the beam propagation method (BPM) is used in the nonlinear regime. For this purpose a self-written MatLAB script is implemented, which shall be roughly introduced here. In the following chapter this method will be discussed in more detail. Note that conventional analytical methods like Fermat's principle or ABCD matrices fail to describe the squaring of the electromagnetic field in the context of the SHG at the metasurface. The Beam Propagation Method expands the beam profile in plane wave modes. Since the propagation of these modes is analytically known, the field at

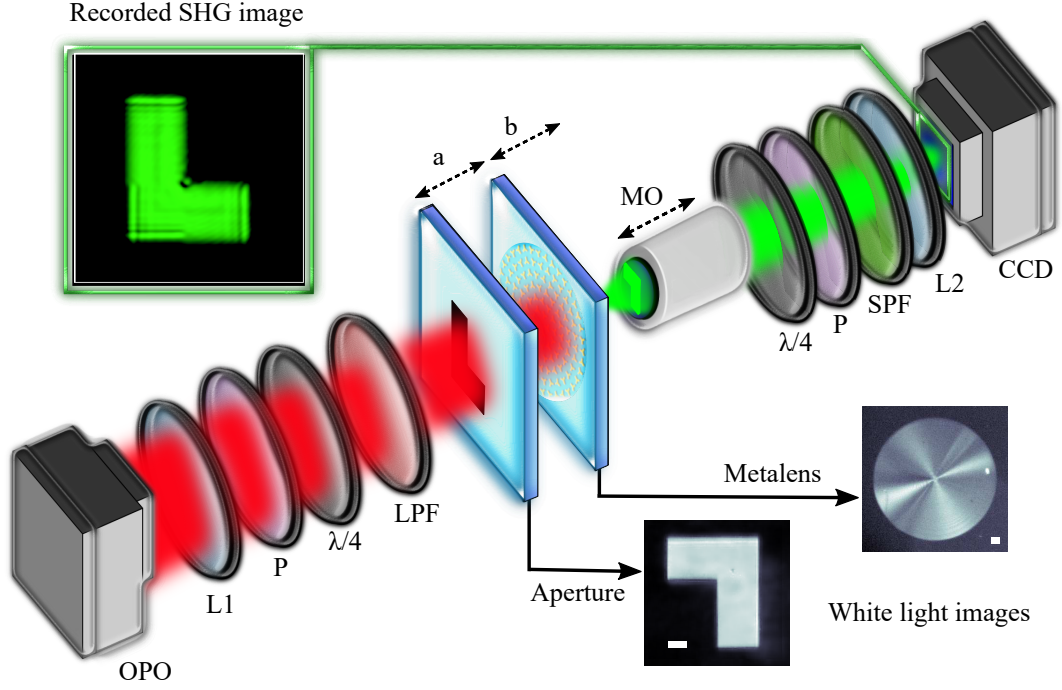


**Figure 3.10: Schematic illustration of the measurement setup.** For the non-linear imaging, different kinds of slot apertures are illuminated with the fundamental beam. The insets show microscopy images of the L-shaped chromium aperture (thickness 100 nm) and of the metalens as well as the simulated SHG image (false color) at the camera position. Acronyms:  $\lambda/4$ , quarter waveplate; CCD, camera; L, lens; LPF, long-pass filter; OPO, optical parametric oscillator; P, polarizer; SPF, short-pass filter; MO, microscope objective lens. The scale bars in the white light images correspond to 20  $\mu\text{m}$ .

the target plane can be calculated. The wave vector in general form reads

$$k_0^2 = k_x^2 + k_y^2 + k_z^2 = \left(\frac{2\pi}{\lambda}\right)^2. \quad (3.14)$$

For the beam propagation along the  $z$ -axis, the  $z$ -component of the wave vector is

$$k_z = \sqrt{k_0^2 - k_x^2 - k_y^2} \approx k - \frac{k_x^2 + k_y^2}{2k}. \quad (3.15)$$

Note that in the implementation the analytical expression for  $k_z$  is used, which leads to imaginary  $k_z$  for  $k^2 < k_x^2 + k_y^2$ . However, most textbooks use the Taylor expanded expression which corresponds to the Slowly Varying Envelope Approximation (SEVA).

Due to the nature of the Fast Fourier Transformation (FFT) the BPM has periodic boundary condition. The general BPM requires three steps to implement the beam propagation to the target plane. Using an appropriate software, the FFT of the  $E$ -field is calculated at the starting plane at  $z = 0$  to

$$E(x, y, z = 0) \rightarrow \tilde{E}(k_x, k_y, z = 0). \quad (3.16)$$

The FFT is then multiplied by the propagator  $\exp(ik_z d)$  leading to an FFT at distance  $z = d$

$$\tilde{E}(k_x, k_y, z = d) = \tilde{E}(k_x, k_y, 0) \exp(ik_z d). \quad (3.17)$$

Then the  $E$ -field at the target plane is calculated with the help of the inverse FFT, resulting in

$$\tilde{E}(k_x, k_y, z = d) \rightarrow E(x, y, z = d). \quad (3.18)$$

Finally, the beam can propagate through the aperture and the nonlinear metalens. Therefore, a mask beam profile for the L-shaped aperture is applied for the incoming beam. Then the  $E$ -field propagates at fundamental wavelength  $\lambda$  to the position of the nonlinear metalens using the general BPM. The spatial distribution of the field  $E_{\text{SHG}}$  generated at the position of the metalens is calculated by

$$E_{\text{SHG}} \sim \exp(i\varphi_{\text{Lens}}) \cdot E^2 \quad \text{with} \quad \varphi_{\text{Lens}} = -\frac{2\pi}{\lambda_{\text{SHG}}} \sqrt{f^2 + r^2}. \quad (3.19)$$

Hereby  $\varphi_{\text{Lens}}$  refers to the phase of the convex nonlinear metalens. Finally, the  $E$ -field propagates at the second harmonic wavelength for various distances to find the image of the original mask with highest contrast. An example calculation is given in appendix C.

#### SHG image formation of an L-shaped aperture

With the help of this method, the nonlinear evolution of the real and virtual image formation can be simulated for specific experimental conditions. It was found in this work that a one-to-one image can be realized with an object distance  $a = -f$  and an image distance  $b = 2f$ . Interestingly, in linear optics this configuration would result in an image formation at infinity because the image distance will diverge. The corresponding calculation with the BPM is shown in appendix C. Based on the predictions of the numerical method the nonlinear imaging progress is experimentally studied in detail by recording the SHG images on the camera while the distance to the metalens is incrementally increased (fig. 3.11 a). For the RCP illumination ( $f = 500 \mu\text{m}$ ), the one-to-one mapping of the upright L-shaped aperture is measured at an image distance of approximately  $b = 1000 \mu\text{m}$ . The simulation (second row) is

in good agreement with the measurement. Note that the interference fringes and the faint upside down L-shaped aperture image in the background come from scattering and refraction effects of the fundamental wave on the metalens and the aperture. These effects disappear for the virtual image formation when the spin state of the fundamental wave is flipped from RCP to LCP and the sign of the focal length is changed, leading to an inverted virtual image of the L located between the L-shaped aperture and the metalens (fig. 3.11 b). In the measurement the virtual image for fundamental LCP light appears at a distance of  $b \approx -300 \mu\text{m}$  with a magnification of  $\Gamma = 0.35$ . These values are close to the simulation results which show an image distance of  $b \approx -333 \mu\text{m}$  and a magnification of  $\Gamma = 0.33$ . Taking these results into account, the image formation can be described empirically for small objects in small distances to the nonlinear metalens approximately by

$$\frac{1}{f} = \frac{1}{b} - \frac{1}{2a}, \quad (3.20)$$

whereas the magnification is given by

$$\Gamma = -\frac{b}{2a}. \quad (3.21)$$

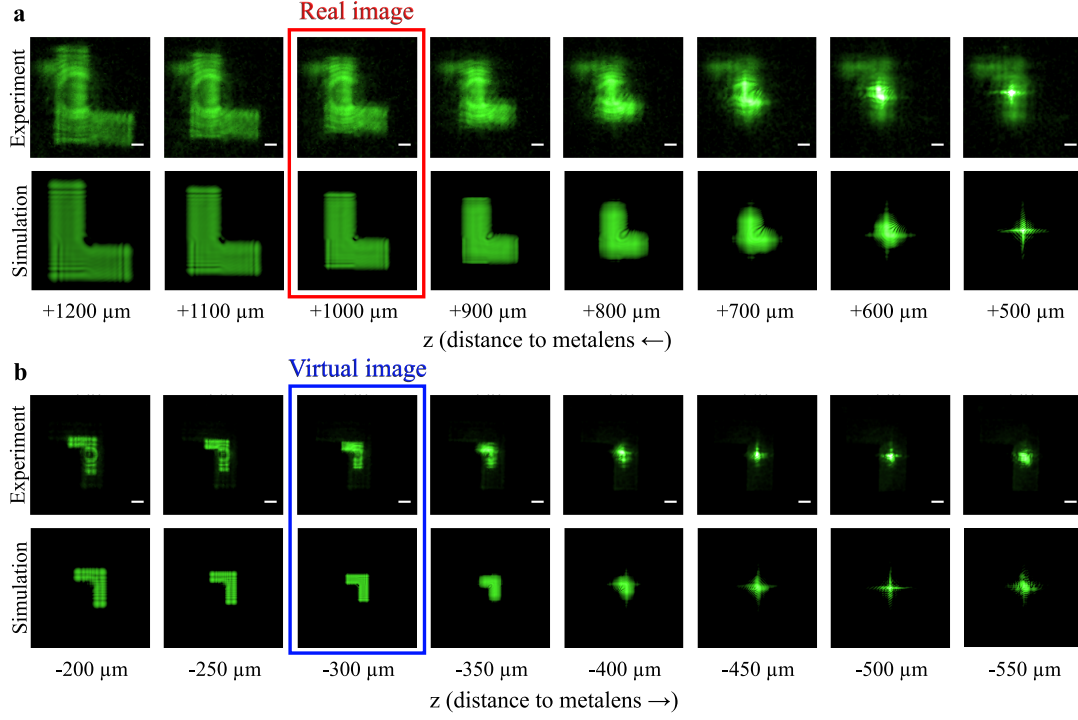


**Figure 3.11: 1:1 spin-dependent object imaging with nonlinear metalens.**

**a** First row: Measured SHG distribution for planes along the  $z$ -propagation direction behind the metalens showing the evolution of the image formation. A clear upright real image of the letter L is formed at  $z \approx 1000 \mu\text{m}$ . Second row: Corresponding Simulation for the SHG distribution along the  $z$ -propagation based on beam propagation method in nonlinear regime. The metalens works as a convex lens for a spin conversion from RCP to LCP so that the real image is formed at  $b = 1000 \mu\text{m}$  behind the metalens with the magnification  $\Gamma = -1$ . **b** For the reversed spin state of the fundamental beam (LCP) the nonlinear metalens acts as a concave lens which images an upside down virtual image of the letter L. The simulation shows a clear image  $300 \mu\text{m}$  before the metalens. The measured image distance is  $b = -300 \mu\text{m}$  with the measured magnification  $\Gamma = 0.35$ . White scale bars correspond to a length of  $20 \mu\text{m}$ . Each single transverse plane is  $200 \times 200 \mu\text{m}^2$  in size and the SHG is encoded in false color on a logarithmic scale for better visibility. Note that all images are reversed by the additional imaging system.

### 3.4.5 Nonlinear plasmonic metalens as 'AND' logic gate

However, compared to a regular lens in the linear regime the nonlinear conversion process at the metalens may affect the image formation. To test the limitations of the nonlinear imaging metalens, different double slit apertures with small gap distances are used to determine the influence of diffraction effects on the image quality. For the double slit apertures the average power is increased to  $\sim 250$  mW. Furthermore, another short-pass filter is inserted in front of the camera to block the fundamental wave. Due to the small feature size, the field distribution of the fundamental wave at the lens exhibits a typical far-field diffraction pattern. For the measurement, an object distance of  $a = -4f$  is set, which is more than  $30\times$  larger than the slit distance between the two slits ( $60\text{ }\mu\text{m}$ ). A sharp real image with the highest contrast is measured in the SHG signal at a distance of  $560\text{ }\mu\text{m}$  with  $\Gamma = -0.12$  behind the metalens (fig. 3.12). The measured values confirm the results from the simulation, which predicts very similar image distance and magnification. However, the SHG image contains a weak third line between the images of the two slits. This additional feature in the image is the result of the nonlinear process at the metalens. It is found that the squaring of the electromagnetic field during the SHG is affecting apertures more, which create an uncompleted interference pattern at the metalens position. Therefore, this imaging limitation depends on the object distance. The effect can be obtained clearly for the measurement of the virtual SHG image with  $\Gamma = 0.11$ . However, such distortions can be reduced by decreasing the object distance or using double slit apertures with larger gap distances. Both would result in less diffraction of the object pattern.

Despite the distortion of imaging due to nonlinear interaction at the metasurface, the nonlinear metalens might have prospective advantages in the subject of nonlinear optical information processing [Der16; Ric10]. Indeed, the experiment above of the nonlinear imaging of the double slits already serves as a demonstration of a 'AND' logic gate if one considers the beams transmitting through the double slits as two input signals, and the weak central line of the nonlinear image as the output signal. The central line is present only if both the signals from the two slits interact nonlinearly at the metasurface, whereas blocking either one or both of the two slits would result in disappearance of the central line. Hence, such nonlinear metalenses might open new possibilities for performing nonlinear mathematical operations (like nonlinear optical Fourier transform) of optical signals.

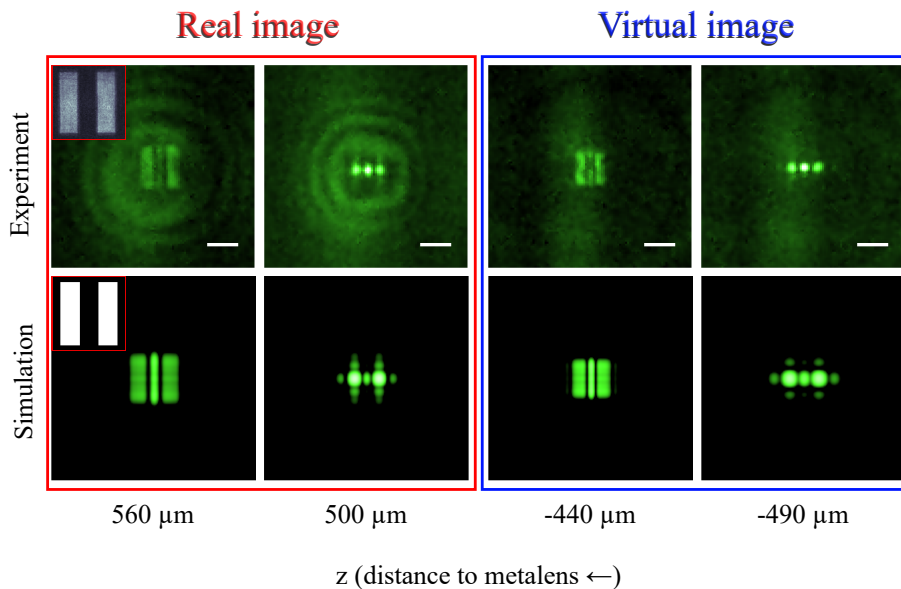


**Figure 3.12: Nonlinear imaging of double slit apertures.** The SHG real image of a double slit aperture with a gap distance of  $60\text{ }\mu\text{m}$  and a slit width of  $30\text{ }\mu\text{m}$  is obtained  $560\text{ }\mu\text{m}$  behind the metalens (red framed). Diffraction orders are observed in the focal distance region at  $z = 500\text{ }\mu\text{m}$ . Reversing the spin state of the fundamental wave (blue framed) results in a virtual image plane as well as the visibility of the diffraction orders at the virtual focal plane at  $z = -440\text{ }\mu\text{m}$  and  $-490\text{ }\mu\text{m}$ , respectively. The second row shows the simulation via beam propagation method. The object distance is  $a = -4f$  and scale bars correspond to  $20\text{ }\mu\text{m}$ .

### 3.5 Further application possibilities for nonlinear plasmonic metasurfaces

In this chapter, further application possibilities for nonlinear plasmonic metasurfaces with 3-fold rotational symmetry are introduced. One publication will be discussed in more detail, since it was also part of this work. Furthermore, a short outlook on the future of this exciting field is offered.

Nonlinear plasmonic metasurfaces offer various and still unexplored application possibilities. Walter et al. proved the usability for real space optical image encoding [Wal17]. Therefore, the Pancharatnam-Berry phase is used to introduce a local interference effect of neighboring meta-atoms that leads to the amplitude modulation of the SHG signal. Only recently, this work continued to demonstrate a nonlinear metasurface for real and Fourier space image encoding [Mao20]. This concept offers independent phase and amplitude control of the SHG and therefore an intriguing

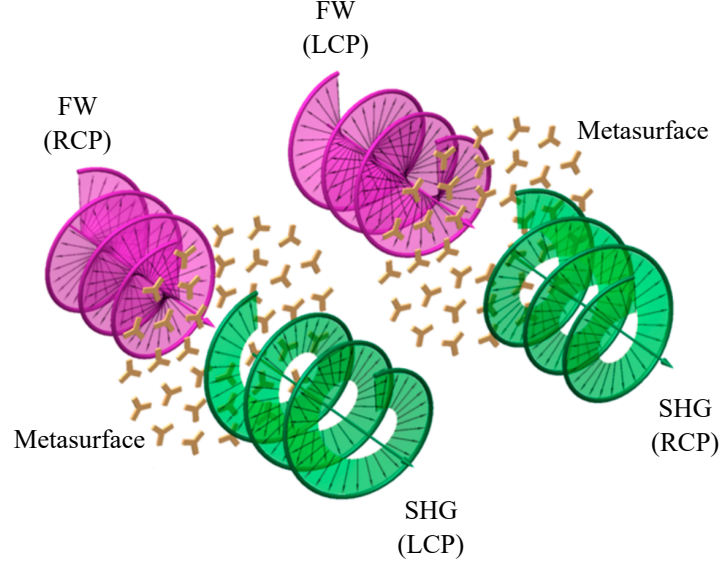


**Figure 3.13: Schematic concept of spin controlled orbital angular momentum generation with a nonlinear plasmonic metasurface.** A fundamental beam (FW) at right or left circular state of polarization (RCP or LCP) is incident onto a nonlinear metasurface consisting of C3 plasmonic meta-atoms that encode the topological charge  $q = 1$ . Compared to the fundamental beam, the second harmonic generation (SHG) that emerges from the metasurface features the opposite circular state of polarization (LCP or RCP) and an orbital angular momentum (OAM) that results in a phase singularity in the center of the beam [Li17a].

platform for optical anticounterfeiting, information encryption and on-chip manipulation of SHG signals. In the future, this concept can even be further developed to realize complex optical fields like propagation invariant optical fields [Gut00; Ker15; Li20] in the nonlinear regime or to investigate nonlinear singular optics [Sos98] with metasurfaces. Singular optics encompasses investigations of structured light with optical singularities, such as optical vortices in scalar optical fields and polarization singularities in vector fields [Nye74; Whe09]. The work of Li et al. can be listed as a first step in the field of nonlinear metasurfaces for singular optics [Li17a]. The schematic concept is shown in fig. 3.13. A nonlinear plasmonic metasurface consisting of gold meta-atoms with 3-fold rotational symmetry is pumped by a circularly polarized fundamental wave. It introduces a nonlinear phase singularity in form of a SHG vortex beam that can be measured in circular cross-polarization. This work provides the first fundamental insight into spin-orbit interaction within a nonlinear process on the nanoscale.

### 3.5.1 Spin angular momentum and orbital angular momentum control

The angular momentum of light is characterized by two components; the spin (SAM) and orbital angular momentum (OAM). Thereby, the SAM of light in free space is associated with either left- or right-circular polarization. There exist different conventions concerning the rotation direction of the electric and magnetic field around the beam axis, which can be observed either from the point of view of the beam source or of the receiver. In fig. 3.13, the view from the receiver is used. Each photon of a right (left) circularly polarized light beam carries the SAM  $+\hbar$  ( $-\hbar$ ), which is directed parallel (anti-parallel) to the beam axis.

In comparison, the OAM features a helical phase front that is characterized by a topological charge. In order to generate the SHG vortex beam three different plasmonic metasurfaces are fabricated that encode different OAM information. The second harmonic phase is given by  $\varphi(x,y) = l \arctan(y/x)$ , where  $l = 1, 2$ , or  $3$  is associated with the topological charge of the OAM or the azimuthal mode index in the SHG (fig. 3.14, first column). Thus, each photon carries an OAM of  $l\hbar$  [All92].

The phase shall be encoded by using the concept of the nonlinear Pancharatnam-Berry phase again, where the phase change for each C3 meta-atom  $3\sigma\theta(x,y)$  only depends on the spatially variant in-plane rotation angle  $\theta(x,y)$ . The parameter  $q = \frac{1}{3}, \frac{2}{3}$ , or  $1$  describes the topological charge of the metasurface. It can be seen in the SEM images that  $q$  implies the number of full rotations of the 3-fold meta-atom on one azimuthal ring (second column).

In the experiment, SHG radiation from the metasurface sample is collected by a microscope objective with its Fourier plane imaged on a camera. The selection rules for plasmonic meta-atoms with 3-fold rotational symmetry illuminated by LCP light specify that SHG is only allowed at RCP light. Now the associated change in the SAM state goes along with the change in the OAM state while the SHG process takes place simultaneously. The SHG vortex beam with increasing radii for larger topological charges can only be detected in cross circular polarization (fig. 3.14, third and forth column). Thereby, the vortex radius scales with the square root of the wavelength and the topological charge  $r_{\text{Vortex}} \propto \sqrt{l\lambda}$  [Blo12]. Hence, the vortex radius is reduced by a factor of  $\sqrt{2}$  compared to a vortex that would emerge from a linear metasurface with the same topological charge.

Conventionally, the experimental measurement of the topological charge involves a Mach-Zehnder interferometer setup that requires the spatial and temporal overlap of optical signals [Gao11]. This is usually a challenging task to do with ultrafast nonlinear signals. However, here another advantage of using metasurfaces based on the PB phase modulation comes into play. By using a linear polarized fundamental wave that is a superposition of both orthogonal circular states of polarization, the phase shift induced by the metasurface works conversely for each circular state of polarization so that the LCP component of the fundamental wave experience a

positive phase modulation with a topological charges of  $l$  while the RCP component undergoes a negative phase modulation with a topological charge of  $-l$ , respectively. While the nonlinear process takes place, both spin states of the fundamental wave are converted to cross-circular polarization and their superposition generates a SH vector beam that is composed of spatially-variant linear states of polarization. After passing through a linear analyzer the interference pattern shows Hermite-Gaussian (HG) modes of light with a petal number of  $2l = 2, 4$  and  $6$  [Yao11]. Thus, the OAM of the SH wave can be qualified experimentally.

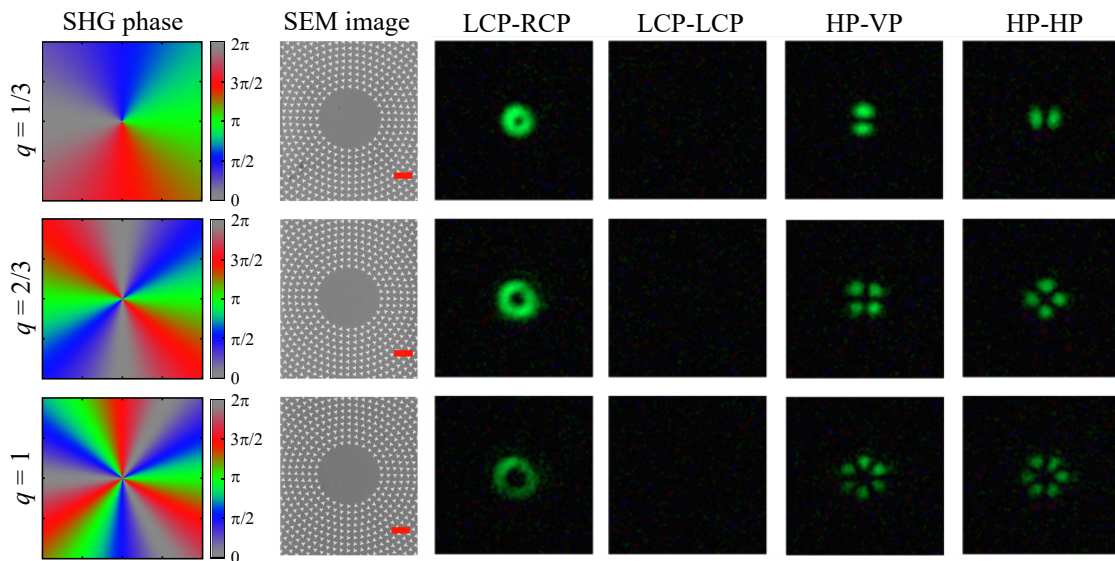


**Figure 3.14: Plasmonic metasurface design and SHG measurements.** The first column shows the real space phase distributions of the SHG that are encoded in different metasurfaces with various topological charges  $q = 1/3, 2/3, 1$ . The second column refers to scanning electron microscope images of those metasurfaces (scale bar: 600 nm). The last four columns show the corresponding SHG intensity distributions measured in the far field for different polarization configurations. For a fundamental wave that is left circularly polarized, the SHG vortex beam can be detected in right circular polarization with increasing radii for larger topological charges. No SHG can be observed in circular co-polarization (LCP-LCP). For a fundamental wave that is horizontally polarized (HP), SHG intensity distributions can be observed with vertical (HP-VP) and horizontal polarization (HP-HP) [Li17a].

### 3.6 Conclusion

In this chapter, different ultrathin nonlinear metasurfaces were demonstrated using second harmonic generation from gold meta-atoms with three-fold rotational symmetry. The desired phase profile was obtained by a nonlinear Pancharatnam-Berry phase that is governed by the meta-atom orientation angle and the spin state of the fundamental wave. All of these findings are related to the understanding of fundamental research according to the nonlinear spin-orbit interaction of light or the nonlinear image formation with nanoscale devices.

In the latter case it was shown that for a near infrared Gaussian laser beam, the spin-dependent focusing effect of SHG waves was experimentally realized at both real and virtual focal planes. Furthermore, real objects, which are illuminated by near infrared light, can be imaged at visible wavelength based on the SHG process

at the nonlinear metalens. Under certain experimental conditions, for example when imaging simple aperture objects located at short object distances, the resulting images in the SHG signal are of a quality that is comparable to performing the experiment with a linear plasmonic metalens. However, the formation of the nonlinear images can no longer be described by the Gaussian lens equation. The experimental results suggest that a modified form of the conventional equation could be applied, which describes the image formation also in the nonlinear regime. The applicability of this equation requires testing for higher nonlinear harmonic processes.

The limitations for the imaging with nonlinear lenses are given by aperture objects which exhibit a strong wave diffraction effect, for example a double slit aperture. The nonlinear interaction of different wave vectors in the plane of the metalens leads to distortions in the nonlinear image. However, these features could be used in the future to realize an 'AND' logic gate. Therefore, the weak central line in the nonlinear image is only present if both signals from the two slits interact nonlinearly, whereas blocking either one or both of the slits switches off the central line.

The symmetry of the meta-atoms only provides the desired Pancharatnam-Berry phase for the nonlinear process leaving the fundamental light unaltered in its propagation. This is in contrast to lenses made of regular nonlinear materials where both beam propagations are manipulated. The concept of nonlinear metalens not only inspires new imaging technologies but also provides a novel platform for generating and modulating nonlinear optical waves.

Furthermore, it could be shown that geometric phase controlled nonlinear metasurfaces can be used to implement many other application possibilities. In this context, a metasurface could be presented for generating SHG signals carrying OAMs. It shows the first simultaneous control of spin and orbital angular momentum of light within a SHG process. Additionally, a new methodology is introduced to measure the SAM-OAM mode in the nonlinear regime with the help of on-chip metasurface interferometry.

The low SHG conversion efficiency from plasmonic metasurfaces could be greatly improved by aligning the optical resonances of metasurfaces with intersub-band transitions of quantum wells. Nonlinear plasmonic metasurfaces, as a complementary alternative to conventional nonlinear optical crystals, may find a wide range of applications in optical switching, information technology, nonlinear wavefront shaping or frequency conversions.

## CHAPTER 4

---

### The nonlinear image formation with nonlinear dielectric metasurfaces

---

Nonlinear metasurfaces are built up as two-dimensional arrangements of subwavelength nanoresonators that have shown the potential to precisely and flexibly control beam parameters like phase, amplitude, polarization, spin, and angular momentum manipulation for the generated nonlinear light [Alm16a; Che10; Ker15; Lee14; Li15; Li17a; Noo16; Tym15; Ye16]. In that way, they incorporate many of the functionalities of their linear counterparts but, at the same time, they perform nonlinear optical transformations. This dual functionality leads to a rather unintuitive physical behavior which is still widely unexplored for many photonic applications. The nonlinear processes render some basic principles governing the functionality of linear metasurfaces not directly applicable, such as the superposition principle and the geometric optics approximation. On the other hand, nonlinear metasurfaces facilitate new phenomena and provide new functionalities that are not possible in the linear regime. In this regard, several peculiar nonlinear phenomena have been reported recently, such as nonlinear holography [Alm16a; Ker15; Rei19], nonlinear optical encryption [Wal17], as well as the image formation not captured by a conventional lens equation [Sch18]. Therefore, fundamental equations like the geometrical-optics thin-lens equation need to be expanded or generalized for nonlinear metalenses working at higher harmonic generations so that a more comprehensive understanding of physics may emerge. With regard to previous chapter 3, a simple continuation of the described plasmonic metalens for the generation of a higher harmonic could not be realized due to the low conversion efficiency and the low damage threshold.

Therefore, the following chapter starts by introducing concepts which are associated with a considerable increase in the efficiency of nonlinear metasurfaces. These so-called all-dielectric metalenses shall enable the imaging of objects at higher harmonic generations [Sch20]. The metalenses consist of silicon nanoparticles that support Mie resonances facilitating the enhancement of the nonlinear conversion efficiency for the third-harmonic process [Gri16; Shc14; Smi16; Yan15]. Real objects are illuminated by infrared light, and their generated images at the visible third-harmonic wavelengths are recorded. The classical lens theory is revisited and a generalized Gaussian lens equation for nonlinear imaging is suggested, which is verified experimentally

and analytically. Additionally, higher-order spatial correlations facilitated by the nonlinear metalens are demonstrated, resulting in additional image features.

#### 4.1 Dielectric versus plasmonic metasurfaces and the paradigm shift in nonlinear optics

In contrast to the plasmonic metasurfaces, the optical response of dielectric nanostructures is not attributed to the plasma resonance [Kra11]. For subwavelength metallic nanoantennas, electric dipoles contribute largely to the Mie scattering, while for dielectric nanostructures, the optical magnetic dipole resonance is of comparable strength and can be included as an additional degree of freedom. The origin of the magnetic dipole lies in the coupling of incoming light to the circular displacement current of the electric field. Therefore, the wavelength needs to be comparable to the optical size of the structure  $\lambda \approx n_s d$  [Kru17]. Hereby a more efficient manipulation of the light can be achieved by interference effects of the different modes. As a consequence of the Huygens' principle, a small nanoantenna that supports a far-field superposition of crossed electric and magnetic dipoles may be considered as a Huygens' source [Gef12] and an array of such particles is termed Huygens' metasurface [Dec15]. In contrast to their plasmonic counterparts, these metasurfaces are not limited by high reflection and absorption losses as well as low polarization-conversion efficiencies. In fact, the highest overall efficiency measured for a linear plasmonic metasurface in transmission mode does not exceed 10% [Kru16]. By including the interaction of scattering contributions of several multipoles (like electric and magnetic dipoles, as well as quadrupoles), a generalized dielectric Huygens metasurface was conceived that offers not only a broad spectral range of operation but also highly efficient functionality. In this regard, single layer transmission metadevices were demonstrated that offer a 100% efficiency in full-wave numerical simulations [Kru16].

Recently, a significant progress has been made in increasing the efficiency of nonlinear processes in metasurfaces by transferring these concepts to the nonlinear regime as the generalized nonlinear Huygens' principle [Wan18]. This is facilitated by designs utilizing high-index dielectric nanoparticles supporting multipolar Mie resonances [Che18a], which offer a paradigm shift in nonlinear optics [Kra18]. This paradigm shift is also evident within this work. Many earlier investigations of intensity-dependent nonlinear optical phenomena were considered to be useless for practical applications because of their complex phase-matching conditions and very low efficiencies. By using optical nonlinear metasurfaces, this hypothesis could be disproved, since especially dielectric metasurfaces offer a breakthrough in the robust implementation of nonlinear optical processes on the nanoscale with simultaneously much higher efficiencies [Wan18].

## 4.2 All dielectric nonlinear metalens for third-harmonic generation

### 4.2.1 Design concept

The theoretical approach for the nonlinear wave-front engineering was developed within an international cooperation and shall therefore only be briefly described here. Electric and magnetic multipolar Mie resonances are used in the frame of the generalized nonlinear Huygens' principle [Wan18].

A planar array of different elliptical nanopillars made from amorphous silicon is employed (150 different nanopillar geometries in total). All nanopillars have the same height of 600 nm and they are arranged into a square lattice with a period of 550 nm. The array is placed on a glass substrate. For linear polarization, all silicon nanopillar resonators are designed to generate a similar intensity of the nonlinear third-harmonic (TH) signal combined with the directional forward scattering. However, the different nanopillars provide different phase delays ranging from 0 to  $2\pi$  via the appearing geometric resonances at the THG frequency. In fig. 4.1 the results of the numerical simulation of the THG amplitude and THG phase for various nanopillar geometries are shown. From this nanostructure library, metalenses of  $200 \times 200 \mu\text{m}^2$  in size are

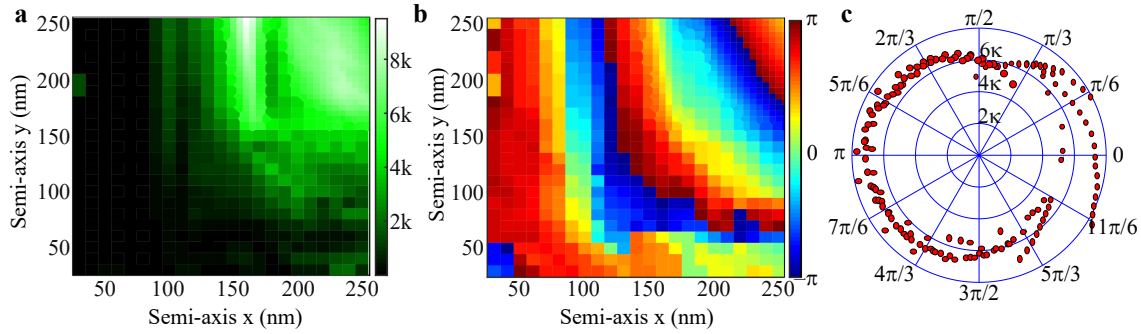


**Figure 4.1: THG amplitude and phase for different nanopillar geometries.**

**a** Numerically simulated THG amplitude and **b** THG phase for different nanopillar semi-axes in both  $x$  and  $y$  directions. **c** Polar plot of numerically simulated THG amplitude (radial) and THG phase (azimuthal) for each nanopillar geometry.

fabricated with focal distances of  $f = 300 \mu\text{m}$  (ML300) and  $400 \mu\text{m}$  (ML400). The corresponding radial phase distribution for each converging lens is given by

$$\varphi(r) = -\frac{2\pi}{\lambda_{\text{THG}}}(\sqrt{f^2 + r^2} - |f|), \quad (4.1)$$

where  $r$  is the radial distance from the center of the lens,  $f$  is the focal length in air and  $\lambda_{\text{THG}}$  is the free-space THG wavelength. The metalenses are designed to work at the telecom wavelength of 1550 nm, which results in a TH wavelength of

approximately 517 nm.

#### 4.2.2 Nanofabrication of the dielectric nonlinear metalens

The nonlinear all-dielectric silicon metalenses are fabricated on a glass substrate following the processes of deposition, patterning, lift-off and etching. At first, a 600-nm-thick amorphous silicon (a-Si) film is prepared with the help of plasma enhanced chemical vapor deposition (PECVD). As a next step, poly-methyl-methacrylate (PMMA) resist layer is spin-coated onto the a-Si film and baked on a hot plate at 170°C for 2 min. Next, the nanopillar structures are patterned by using standard electron beam lithography (EBL). The sample is then developed in 1:3 MIBK:IPA solution and washed with IPA before being coated with a 20-nm-thick chromium layer using electron beam evaporation. Afterwards, a lift-off process in hot acetone was performed. Finally, by using inductively coupled plasma reactive ion etching (ICP-RIE), the structures were transferred from the chromium mask to silicon. The fabricated nanopillars are illustrated in fig. 4.2.

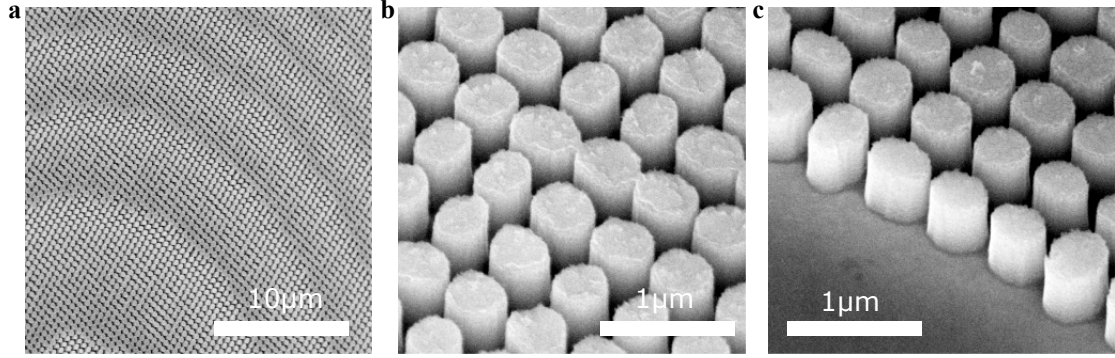


**Figure 4.2: SEM images of a nonlinear dielectric metalens.** Scanning electron microscopy images show different parts of the nonlinear dielectric metalens with a focal length of  $f = 300 \mu\text{m}$ . The nanostructures are imaged at different magnifications ( $M_b = M_c = 10 \times M_a$ ). The depth of field can be enlarged by choosing a smaller aperture. In this way, the sample can be sharply imaged under an angle of  $\pi/4$  to visualize the three-dimensional shape of the structures.

#### 4.2.3 Optical characterization with third-harmonic diffraction efficiency

By only illuminating a small outer part of the metalens by a linearly polarized Gaussian beam, it will locally act as a beam deflector redirecting the TH wave under an angle with regard to the fundamental wavevector (fig. 4.3 a). In this way, the metalens is experimentally verified by multispectral  $k$ -space analysis over the fundamental wavelengths from 1400 nm to 1700 nm. The THG diffraction angle is

determined by

$$\sin(\theta) = \left| \frac{k_x}{k_0} \right| = \frac{\lambda_{\text{THG}}}{\Lambda_{2\pi}(r)}, \quad (4.2)$$

where  $\Lambda_{2\pi}(r)$  is the local 0 to  $2\pi$  phase period, which depends on the radius  $r$ .

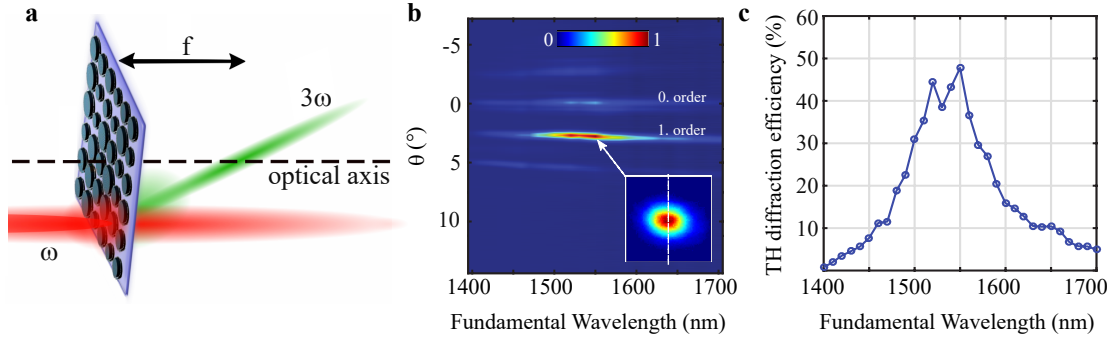


**Figure 4.3: TH diffraction efficiency.** **a** Conceptual image of a small outer segment of a lens working as a beam deflector. **b** Measured spectra of the THG directionality from a metalens obtained in this scenario. **c** measured THG diffraction efficiency

In all optical experiments, the nonlinear metalens is pumped with linearly polarized 40 femtosecond (fs) pulses from an optical parametric amplifier (OPA). The laser repetition rate is 1 MHz and the used average power for the nonlinear measurements is  $\approx 1.8$  mW (pulse energy: 1.8 nJ, peak power: 42.3 kW). Then the fs laser beam of each wavelength is focused by an achromatic condenser lens ( $f_0 = 75$  mm) that leads to a peak power density of  $1.5 \frac{\text{GW}}{\text{cm}^2}$ . The metalens is illuminated at normal incidence and the nonlinear response from the metalens in forward direction is collected by an infinity corrected microscope objective ( $\times 20 / 0.45$ ). The TH signal is filtered by two short-pass filters to remove the fundamental light. A  $4f$  configuration is used in order to image the MO's back focal plane onto the ultra-low noise sCMOS camera (Andor Zyla 5.5<sup>1</sup>).

The nonlinear metalenses reach a maximum diffraction efficiency for the THG of 48 % (fig. 4.3 c). The experimentally measured THG conversion efficiency is of the order of  $10^{-6}$ . With regard to previous work [Sch18], image formation with an appropriate plasmonic nonlinear metalens for higher harmonic generations was not demonstrated before due to the low conversion efficiency and the low damage threshold.

<sup>1</sup> <https://andor.oxinst.com/products/scmos-camera-series/zyla-5-5-scmos>

#### 4.2.4 Focusing of Gaussian beams by a THG metalens

Next, the focusing of Gaussian beams by the nonlinear metalens is studied experimentally. A schematic illustration is shown in fig. 4.4a. A fundamental wave at frequency  $\omega$  converted to a third-harmonic wave at frequency  $3\omega$  and focused by the nonlinear metalens. As an example, the transverse THG intensity distribution at the focal distance of ML400 is shown on a logarithmic scale (fig. 4.4b). In fig. 4.4c the one dimensional intensity distribution through the focal point is measured.

Furthermore, the THG intensity distribution can be traced behind the metasurface on a camera (fig. 4.4d). Therefore, the transverse 2D intensity distribution is measured every  $15\text{ }\mu\text{m}$  in the  $z$ -direction by changing the axial position of microscope objective position. Subsequently, by a cut through every single transverse intensity distribution in horizontal direction, the obtained intensity profiles are plotted in the axial direction. By splitting the beam path the intensity distribution of the pump beam in the near-infrared range is also imaged on an additional infrared camera. Consequently, the propagation of the fundamental beam and the third-harmonic wave can be determined along the optical axis. The experiment is repeated for ML300 (fig. 4.4e).

In both measurements, the fundamental wave (red) with wavelength  $\lambda = 1550\text{ nm}$  is loosely focused by a regular lens with a focal length of  $500\text{ mm}$  to the metasurface so that the beam waist at the sample position is slightly larger than the size of the metalens. The Gaussian fit of the fundamental wave shows a FWHM of  $111.3\text{ }\mu\text{m}$  (fig. 4.4f). The inset in fig. 4.4f illustrates that the beam is slightly blurred for a larger distance to the center.

There are several ways to characterize the beam width in a plane perpendicular to the beam axis, for example, the full width at half maximum (FWHM),  $1/e^2$ -width,  $D4\sigma$  width, knife-edge width or  $D86$  width, to name a few [Sie98]. In most works on metalenses, the simple experimental determination of the FWHM is used, which is compared with the calculation of the diffraction-limited Airy disk FWHM of  $0.51 \frac{\lambda}{\text{NA}}$  [Lia18].

In fig. 4.4g, the TH intensity distribution at the transverse plane of the focal spot (blue spheres) is plotted on a 2D Gaussian surface fit (green). The averaged TH Gaussian full width at half maximum (FWHM) is determined to  $1.3\text{ }\mu\text{m}$ . That corresponds to the Gaussian root mean square (RMS) width of [Alm16a]

$$c = \frac{\text{FWHM}}{2\sqrt{2\ln 2}} \approx 0.5\text{ }\mu\text{m}. \quad (4.3)$$

These values are near to the theoretical value of a TH diffraction limited spot:

$$\text{FWHM}_0 = 0.51 \frac{\lambda_{\text{THG}}}{\text{NA}} \approx 0.8\text{ }\mu\text{m} \text{ and } c_0 = 0.4\text{ }\mu\text{m}, \quad (4.4)$$

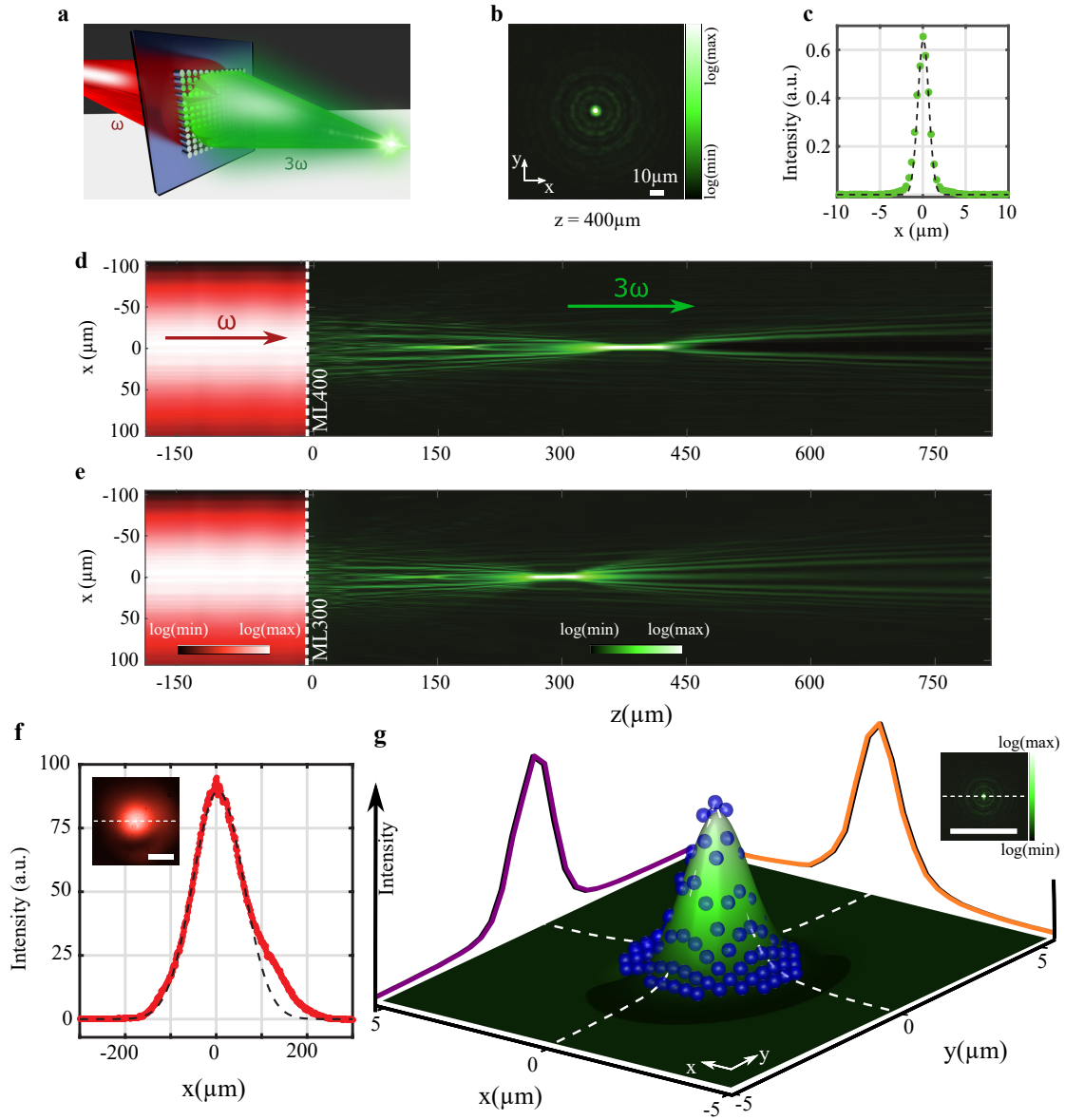


**Figure 4.4: Nonlinear conversion and focusing of the fundamental Gaussian beam.** **a** Conceptual illustration of the fundamental wave at frequency  $\omega$  converted to a third-harmonic wave at frequency  $3\omega$  and focused by the metasurface lens. **b** Measured TH intensity distribution of the focal spot at  $z = 400 \mu\text{m}$  (logarithmic scale). **c** 1D TH intensity profile showing a Gaussian RMS spot size of  $0.6 \mu\text{m}$ . **d** Experimental distribution of the fundamental (red, left side) and third-harmonic (green, right side) intensities along the optical axis for the fundamental wavelength of  $1550 \text{ nm}$  and metalens focal distance of  $f = 400 \mu\text{m}$ . **e** The same experiment is shown for the metalens with a focal distance of  $f = 300 \mu\text{m}$ . **f** 1D transverse intensity distribution of the fundamental beam  $105 \mu\text{m}$  in front of the nonlinear metalens. The inset shows the 2D intensity distribution (scale bar:  $100 \mu\text{m}$ ) **g** Measured 2D transverse intensity distribution (blue spheres) of the TH focus spot together with a Gaussian surface fit (green). The inset shows the measured 2D THG intensity on a logarithmic scale (scale bar:  $100 \mu\text{m}$ ).

where  $d = 200 \mu\text{m}$  is the diameter of the metalens and  $\text{NA} = \sin(\arctan(\frac{d}{2f}))$  is the numerical aperture. The focal Gaussian RMS spot size of ML400 is found to be  $0.6 \mu\text{m}$ . This result is also close to the respective diffraction limited RMS spot sizes of  $0.5 \mu\text{m}$ .

As a next step, the pump beam size is narrowed down (FWHM of  $50 \mu\text{m}$ ) and the beam is shifted from the optical axis, as shown in fig. 4.5. The corresponding focusing and transverse shift of the THG beam are traced experimentally for both nonlinear metalenses. This experiment demonstrates how the fundamental Gaussian beam is converted into the TH secondary beam: it is deflected, focused at  $z = f$  to a FWHM spot size of  $3.5 \mu\text{m}$  and after a propagation length of  $z = 2f$ , the TH secondary beam waist of  $28 \mu\text{m}$  can be obtained, which is very close to an analytical prediction of  $\frac{50\mu\text{m}}{\sqrt{3}} \approx 29 \mu\text{m}$ . The analytical calculation will be discussed in the following section.

#### 4.2.5 Derivation of nonlinear lens equation based on the imaging of a single Gaussian beam waist

In order to describe the nonlinear behavior of this new type of nonlinear image construction, the 'imaging' of a Gaussian beam waist is analyzed. The advantage of using Gaussian beams to illustrate the nonlinear functionality is that the concept of the nonlinear beam propagation method can be used in order to solve the image formation analytically [Van81]. At first, it is shown how this mathematical concept works in the linear regime for a conventional lens. Therefore, a one-dimensional electromagnetic field distribution  $E_i(x)$  is considered at an object distance  $a$  from a linear lens with a focal length  $f$ . Now, the question is at which distance one can observe a reconstruction of the Gaussian beam waist. This specific distance is called the image distance  $b$ . The output field  $E_f(x)$  can be calculated by the beam propagation method. To apply this method here, one can separate it into three parts: the propagation over the object distance  $a$  to the lens position, the effect of the lens' phase profile and the propagation over the image distance  $b$ . For a simple propagation over an arbitrary distance  $z$  the input field is Fourier transformed to the  $k$ -space, multiplied with the propagator  $e^{ik_z z}$  and back-transformed to the spatial domain. This gives rise to the following equation that describes the imaging of an electromagnetic field distribution  $E_i(x)$  with a linear lens.

$$E_f(x) = \mathcal{F}^{-1}[\mathcal{F}[\mathcal{F}^{-1}[\mathcal{F}[E_i(x), k] e^{-ik_z a}, x] e^{i\sigma k_0 \sqrt{f^2 + x^2}}, k] e^{ik_z b}, x] \quad (4.5)$$

where  $k_0$  is the length of the wave vector,  $k_z$  the longitudinal component of the wave vector and  $\sigma = \pm 1$  stands for a concave or convex phase profile. In most of the literature, a Taylor expanded expression is used, which corresponds to the slowly varying envelope approximation (SVEA). The use of an analytical expression for  $k_z$

can lead to an imaginary  $k_z$  if  $k_0^2 < k_x^2$ . Here, the following expressions are used:

$$k_0^2 = k_x^2 + k_z^2 = \left(\frac{2\pi}{\lambda}\right)^2 \rightarrow k_z = \sqrt{k_0^2 - k_x^2} \approx k_0 - \frac{k_x^2}{2k_0}. \quad (4.6)$$

This also leads to the approximation for small  $x$ , so that

$$\sqrt{f^2 + x^2} \approx f + \frac{x^2}{2f}. \quad (4.7)$$

In the simplest case, the input field is just a Gaussian function  $E_i(x) = e^{-wx^2}$  where the parameter  $w$  determines the width of the Gaussian beam. The intensity is proportional to  $I_i \propto |e^{-wx^2}|^2 = e^{-2wx^2}$  with the full width at half maximum  $\text{FWHM}_i = 2\sqrt{\frac{\ln 2}{2w}} \propto \frac{1}{\sqrt{w}}$ . The first Fourier transformation is given by

$$\mathcal{F}_x[e^{-wx^2}](k) = \frac{1}{\sqrt{2w}} e^{-\frac{k^2}{4w}}, \quad (4.8)$$

which shows that the Gaussian character is preserved. Following eq. (4.5) and applying eq. (4.6)-eq. (4.8) will result in the full analytical solution of the electromagnetic output field. The output intensity is proportional to square of the amplitude:

$$I_f \propto \exp \left[ \frac{-2wf^2k_0^2x^2}{4w^2(b(f - a\sigma) - fa)^2 + k_0^2(b\sigma + f)^2} \right]. \quad (4.9)$$

Comparing the fraction  $I_f$  and  $I_i = e^{-2wx^2}$  leads to the condition that the denominator's term  $4w^2(b(f - a\sigma) - fa)^2$  needs to be canceled in order to reconstruct the object in the output field, since it should not have any dependence on the width of the input Gaussian function. This leads directly to the conventional lens equation.

$$-\sigma \frac{1}{f} = -\frac{1}{a} + \frac{1}{b} \quad \text{with} \quad \sigma = \begin{cases} -1 & \text{convex lens} \\ +1 & \text{concave lens} \end{cases} \quad (4.10)$$

To calculate the magnification  $\Gamma$  one has to compare the beam widths of the input and output intensity. The input FWHM is proportional to the reciprocal square root of  $w$ , so input and output exponent can be divided and the reciprocal square root is taken:

$$\Gamma = \left( \sqrt{\frac{f^2k_0^2}{k_0^2(b\sigma + f)^2}} \right)^{-1} = \left( \frac{f}{b\sigma + f} \right)^{-1} = \frac{b}{a}. \quad (4.11)$$

In the last conversion, one needs to input the lens equation for  $f$ . These equations fully solve the image formation in the linear regime.

If the beam propagation method in the nonlinear regime with harmonic generation order  $n$  is taken into account, the electromagnetic output field changes to

$$E_f^{(nl)}(x, n) = \mathcal{F}^{-1} \left[ \mathcal{F} \left[ \left( \mathcal{F}^{-1} \left[ \mathcal{F} [E_i(x), k] e^{-ik_z a}, x \right] \right)^n e^{i\sigma n k_0 \sqrt{f^2 + x^2}}, k \right] e^{ink_z b}, x \right]. \quad (4.12)$$

Following the same path as in the linear case leads to a very similar output intensity of

$$I_f^{(nl)} \propto \exp \left[ \frac{-2wnf^2k_0^2x^2}{4w^2(b(f - a\sigma) - fa)^2 + k_0^2(b\sigma + f)^2} \right]. \quad (4.13)$$

The only difference is the harmonic generation order  $n$  in the numerator of the exponent. This expression leads to the linear lens equation as well because the denominator is completely the same as before. As a basic example, the 1:1 image formation of a single Gaussian beam waist is compared: In the linear case, the rule to observe a 1:1 image is  $b_{1:1}^{(l)} = 2\sigma f$ . The situation is very different in the nonlinear case: It can be found that  $b_{1:1}^{(nl)} = \pm\sqrt{n}a = \frac{f}{\sigma\pm\sqrt{n}}$ . That means the 1:1 image of a Gaussian beam appears to have two solutions. For instance, a convex ( $\sigma = -1$ ) THG metalens ( $n = 3$ ) with a focal length of  $f = 400 \mu\text{m}$  has two configurations to observe the 1:1 image of a Gaussian beam waist:

1.  $b_{1:1}^{(nl)} \approx +546 \mu\text{m}$  and  $a \approx -315 \mu\text{m}$  or
  2.  $b_{1:1}^{(nl)*} \approx -146 \mu\text{m}$  and  $a^* \approx -85 \mu\text{m}$ .
- (4.14)

This shows that the nonlinear convex lens can be used to form an inverted real 1:1 image (first case) as well as an upright virtual 1:1 image (so that object and image appear on the same side of the lens (second case)). In general, the nonlinear magnification for the Gaussian beam is

$$\Gamma^{(nl)} = \frac{b}{\sqrt{na}}. \quad (4.15)$$

This result is conform to the observations in the experiment of the single Gaussian beam waist 'imaging'. In fig. 4.5 the nonlinear beam waist conversion for the metalens with focal length of  $f = 300 \mu\text{m}$  is shown. The incident fundamental Gaussian beam with a width of  $w = 50 \mu\text{m}$  is shifted  $36 \mu\text{m}$  in x-direction from the lens center (fig. 4.5 a). Similar results can be observed for using the second nonlinear metalens (ML400, b). The nonlinear metalens position at  $z = 0 \mu\text{m}$  can be verified by taking the white light illuminated microscopic image (fig. 4.5 c). The incident fundamental Gaussian beam hits the nonlinear metalens at the position marked with a red cross.

The lens is locally acting as a beam deflector, which diffracts the THG beam in the direction of the lens center. In a distance of  $2f$  behind the metalens, the image of the Gaussian beam waist with a width that is reduced by the factor of  $\frac{1}{\sqrt{n}}$  is obtained. Here, the TH beam width of  $27\text{ }\mu\text{m}$  is measured. The measurement in e shows similar results. In this case, the nonlinear metalens ML400 generates the TH Gaussian beam in a distance of  $2f = 800\text{ }\mu\text{m}$  and with a FWHM of  $29\text{ }\mu\text{m}$ .

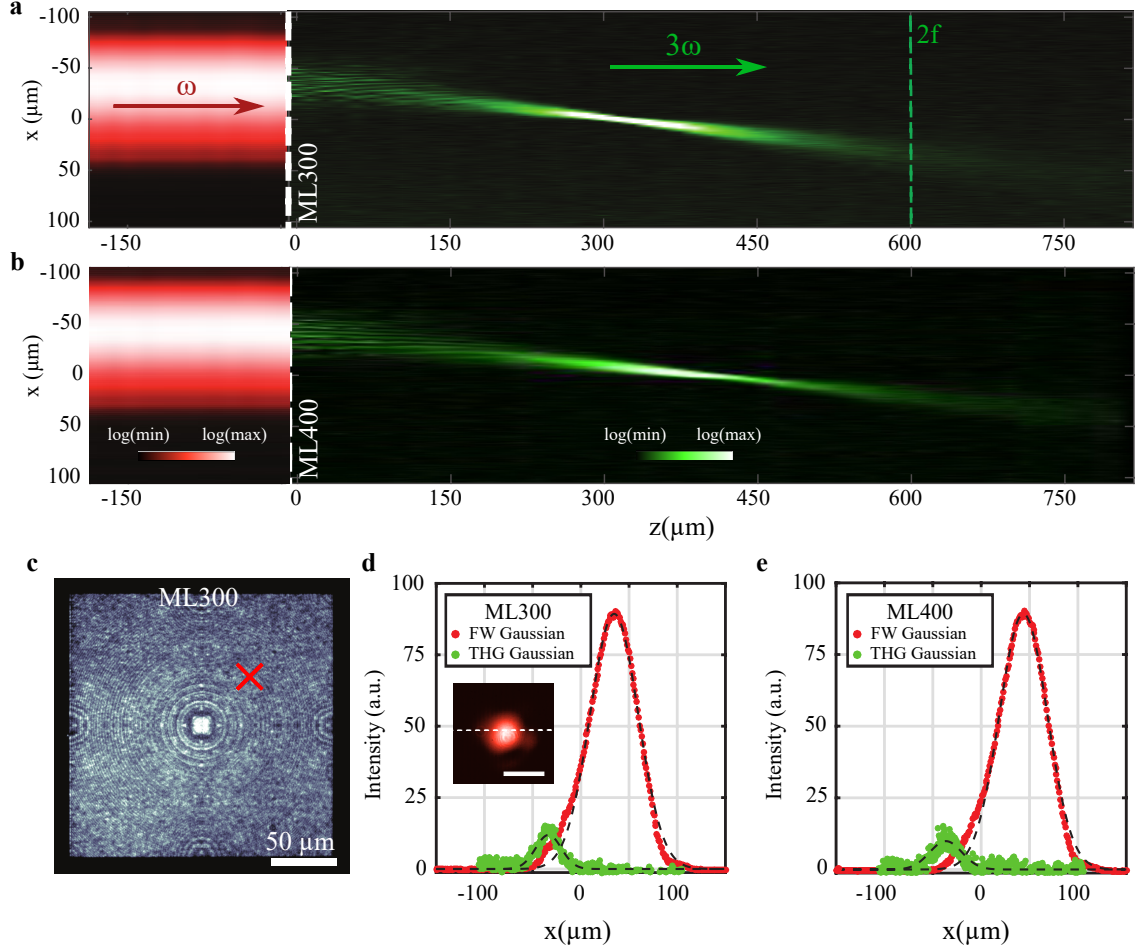


**Figure 4.5: Image formation of a single Gaussian beam waist.** **a** Experimentally obtained THG intensity distribution (green color) for the imaging of an off-axis fundamental Gaussian beam (red color) by the nonlinear metalens with focal length of  $f = 300 \mu\text{m}$ . **b** The same experiment is shown for the metalens with a focal distance of  $f = 400 \mu\text{m}$ . **c** Microscopic white-light image of the nonlinear metalens **d** Measured 1D transverse intensity distribution of the fundamental wave intensity and the TH intensity at  $2f = 600 \mu\text{m}$  distance (ML300). The inset shows the measured 2D fundamental wave intensity (scale bar:  $100 \mu\text{m}$ ). **e** Measured intensities as in d but for the metalens ML400. The THG Gaussian beam is obtained in a distance of  $2f = 800 \mu\text{m}$ .

### 4.3 Generalized Gaussian lens equation

It is difficult to describe the image formation of simple real objects analytically because the Fourier transformation is more complex than for Gaussian beams. Therefore, a general analytical solution for the nonlinear image formation of shaped apertures cannot be provided. However, under the assumption that a simple object is illuminated by a plane wave very near to the metalens position, one can neglect the diffraction of the object for the propagation distance to the metalens. Thus, the fundamental intensity distribution on the metasurface does not change much compared to the object plane [Meh17]. It can still be assumed as a binary step function consisting only of ones and zeros. In this case, the raise to the  $n$ th power of the electromagnetic field can be neglected. This will simplify the mathematical derivation of the nonlinear lens equation. By removing the exponent  $n$  the equation becomes solveable. The nonlinear electromagnetic output field for plane wave (pw) illumination reads:

$$E_{\text{pw}}^{(\text{nl})}(x, n) = \mathcal{F}^{-1} \left[ \mathcal{F} \left[ \left( \mathcal{F}^{-1} \left[ \mathcal{F} [E_{\text{pw}}(x), k] e^{-ik_z a}, x \right] \right)^n e^{i\sigma n k_0 \sqrt{f^2 + x^2}}, k \right] e^{ink_z b}, x \right]. \quad (4.16)$$

Solving this approach leads to a modified form of the Gaussian lens equation, the generalized nonlinear lens equation:

$$\frac{1}{f} = \frac{1}{b} - \frac{1}{n \cdot a}. \quad (4.17)$$

The simplification can be supported with the help of a numerical BPM simulation. In fig. 4.6 the THG image of an L-shaped aperture is shown in the image distance. In the left picture the raise to the third power of the electromagnetic field is taken into account, while in the second one it is left out. It can be seen that the intensity distributions differ only slightly and therefore the simplification introduced above can be adopted. To demonstrate the imaging of real objects experimentally, the L-shaped aperture is placed it in a very short distance ( $a=300 \mu\text{m}$ ) to the metalens sample (ML300). Note that in linear optics this should result in an image formation at infinity. The aperture is illuminated with the broader fundamental beam waist (FWHM  $\approx 111 \mu\text{m}$ , condenser lens focal length:  $f_0 = 500 \text{ mm}$ ). Then the THG intensity distribution in different transverse planes on the optical axis is measured (fig. 4.7). At the metalens position ( $z = 0$ ), it is observed that the L-shape intensity distribution does not change much. One part of the THG intensity is converted and contributes to the image formation process, while the other part comes from the silicon itself and does not contain the phase information of the metalens. Therefore, its change in propagation direction is only caused by diffraction of the aperture. For a distance larger than  $z = 100 \mu\text{m}$  from the lens position, one can distinguish

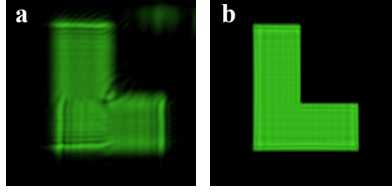


**Figure 4.6: Numerical simulation of the THG image formation.** **a** Simulated TH intensity obtained by taking into account the raise to the third power of the electromagnetic field. **b** Simulation results obtained by neglecting the raise to the third power of the electromagnetic field. The parameters are object distance  $a = -300 \mu\text{m}$ , image distance  $b = 450 \mu\text{m}$ , and focal length  $f = 300 \mu\text{m}$ .

between the converted and the unconverted part of the THG. The converted part is focused at the focal length of  $f = 300 \mu\text{m}$ . The sharpest L-shape image is detected at  $z \approx 450 \mu\text{m}$  with a magnification  $\Gamma^{(\text{nl})} \approx -0.5$ . This is in perfect agreement with the generalized nonlinear lens equation and magnification equation:

$$b = \left( \frac{1}{f} + \frac{1}{3a} \right)^{-1} = 450 \mu\text{m} \quad \text{and} \quad \Gamma^{(\text{nl})} = \frac{b}{3a} \approx -0.5. \quad (4.18)$$

Interestingly, a small amount of THG features a negative phase profile (compare fig. 4.3, -1 diffraction order). The resulting concave lens-like phase profile forms a virtual nonlinear image at the image distance  $b^*$  in front of the metalens ML300 with focal length of  $f^* = -300 \mu\text{m}$ . In accordance to the generalized nonlinear lens equation, this distance is determined by

$$b^* = \left( \frac{1}{f^*} + \frac{1}{3a} \right)^{-1} = -225 \mu\text{m} \quad \text{and} \quad \Gamma^{(\text{nl})*} = \frac{b^*}{3a} \approx -0.25. \quad (4.19)$$

In the measurement, the sharpest image formation can be clearly detected between  $z = -220 \mu\text{m}$  and  $z = -230 \mu\text{m}$ . The the corresponding simulation with BPM just utilizes a negative phase profile.

These experimental measurements of the THG real image formation were repeated for greater object distances  $a = (-400, -500) \mu\text{m}$  (see fig. 4.8). The sharpest THG image is detected at  $z = 380 \mu\text{m}$  (for  $a = -500 \mu\text{m}$ ), or rather  $z = 400 \mu\text{m}$  (for  $a = -400 \mu\text{m}$ ). It turns out that a configuration with small  $|a|/l$  parameter (where  $l$  is the size of the aperture) is beneficial for the nonlinear image formation. In this way, the nonlinear autocorrelation (which will be demonstrated in section 4.4) is weak and thus the nonlinear image quality is similar to its linear counterpart.

As an overview, the most important results are summarized in fig. 4.9. It is

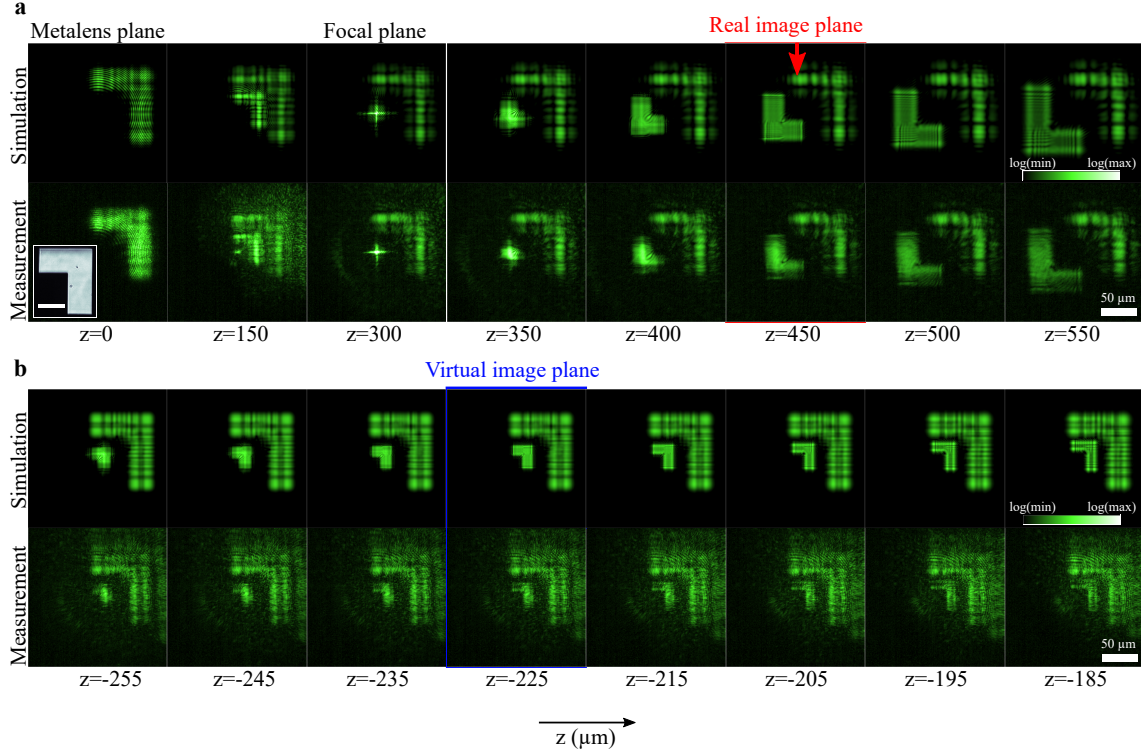


**Figure 4.7: Simulation and measurement of the THG image formation for an L-shaped aperture.** **a** The first row shows the simulation and the second row the corresponding measurement. An L-shaped aperture (white inset) is placed in a small object distance ( $a = -300 \mu\text{m}$ ) to the nonlinear metalens ML300. The THG intensity distribution is measured on the optical axis. The upper right corner shows the THG just originating from the silicon without any lens-like phase profile. At  $z = 450 \mu\text{m}$  the sharpest THG image is detected. **b** The simulation for the same configuration but with a negative phase profile (concave lens) results in a virtual image formation at  $z = -225 \mu\text{m}$ . The second row verifies that a small part of the generated THG features a negative lens profile, which forms the corresponding virtual image in accordance to a generalized lens equation.

demonstrated how the optical information of an upside-down L-shaped aperture (a), which is illuminated with the fundamental wave, is first subjected to a nonlinear optical Fourier transformation by the nonlinear metalens ML300 (b), and then the optical information is reproduced in the image plane as an upright real image in the THG (c). These experimental findings are supported by theoretical calculations employing the nonlinear beam propagation method fig. 4.9 (d-f). All the measurements of the nonlinear image formation for different object distances  $a = (-300, -400, -500) \mu\text{m}$  are plotted on the function  $b(a) = (\frac{1}{f} + \frac{1}{3a})^{-1}$ , which confirms the validity of the generalized Gaussian lens equation. An interesting conse-

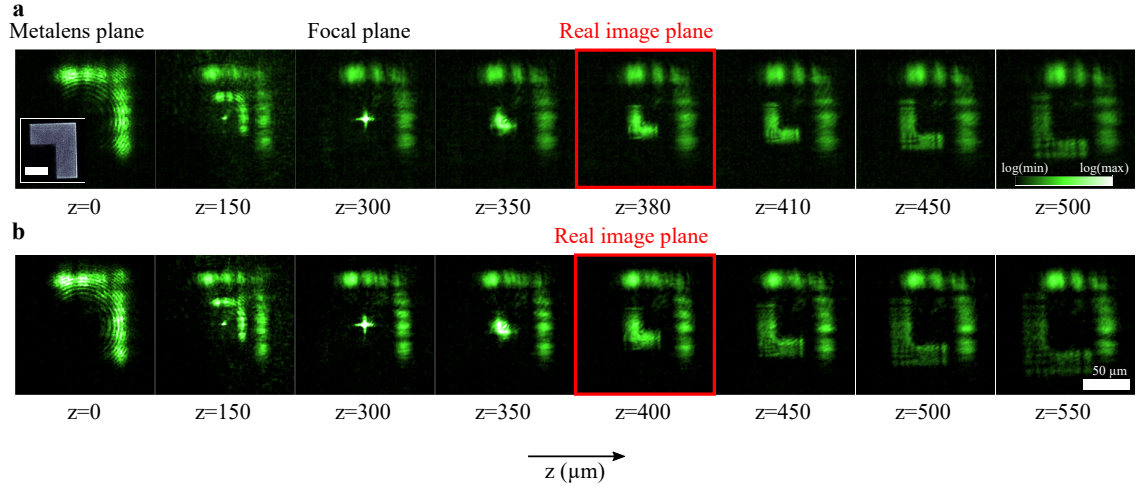


**Figure 4.8: Measurement of the THG image formation for different object distances.** **a** An L-shaped aperture (white inset) is placed in an object distance ( $a = -500 \mu\text{m}$ ) to the nonlinear metalens ML300. The THG intensity distribution is measured on the optical axis. The upper right corner shows the THG just originating from the silicon without any lens-like phase profile. At  $z = 380 \mu\text{m}$  the sharpest THG image is detected. **b** THG image formation for a different object distance ( $a = -400 \mu\text{m}$ ). The image plane is measured at  $z = 400 \mu\text{m}$ .

quence of the generalized nonlinear lens equation is the shift of the image formation to shorter object distances  $|a|$  depending on the order of the nonlinear process  $n$ . The resulting graphs for the image distance  $b(n, a)$  for linear metalens (red), SHG metalens (green), and THG metalens (blue) are shown in fig. 4.10a. All lenses have a focal length of  $f = 300 \mu\text{m}$  and can produce a 1:1 image at an image distance of  $b = 2f = 600 \mu\text{m}$  (black rectangular dots). Note that the image distance  $b$  always diverges for  $a = f/n$ . The configurations used in the previous measurements and simulations for the THG lens are illustrated as blue dots in the graph for the THG image formation. A special case is the generation of a virtual image using a convex converging lens (fig. 4.10b). This has already been demonstrated for linear metalenses [Che12]. However, the generalized nonlinear lens equation now offers the possibility to generalize this prescription as well. For this, the object must be placed at an object distance of  $a < f/n$ . Such case is marked as a magenta point in the graph. The L-shaped aperture is located in an object distance of only  $a = -f/6 = -50 \mu\text{m}$ . According to the generalized lens equation, the THG image should be formed at an image distance of  $b = -f = -300 \mu\text{m}$ . Such a short object distance  $|a|$  is difficult to realize experimentally. However, it can be confirmed by numerical simulation using the BPM. It is shown that the virtual image formation in the third-harmonic signal features a magnification of  $\Gamma^{(\text{nl})} = b/3a = 2$  at the expected image distance of

$b = -300\text{ }\mu\text{m}$  (fig. 4.10c). The image is oriented in the same way as the aperture.

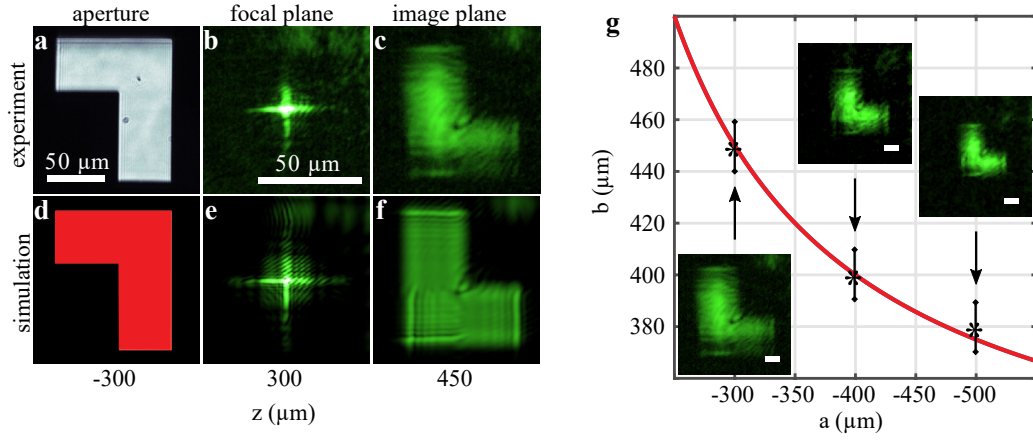


**Figure 4.9: Nonlinear imaging governed by the generalized Gaussian lens equation.** Upper row: **a** Microscopic white light image (transmission) of the fabricated L-shaped aperture placed at an object distance  $a = -f = -300 \mu\text{m}$  in front of the metalens (ML300). In this configuration, a conventional lens equation predicts an image formation at infinity distance. **b** Focusing of the THG at  $z = 300 \mu\text{m}$  back focal plane of the metalens. **c** TH image formation of the L-shaped aperture at an image distance of  $b = 450 \mu\text{m}$ . The real image appears inverted and demagnified in full agreement with the generalized lens equation. **d-f** Corresponding numerical simulation with beam propagation method on the same length scale. **g** Plot of image distances  $b$  versus object distances  $a$ . THG image formation measurement is shown for different object distances  $a = (-300, -400, -500) \mu\text{m}$ .

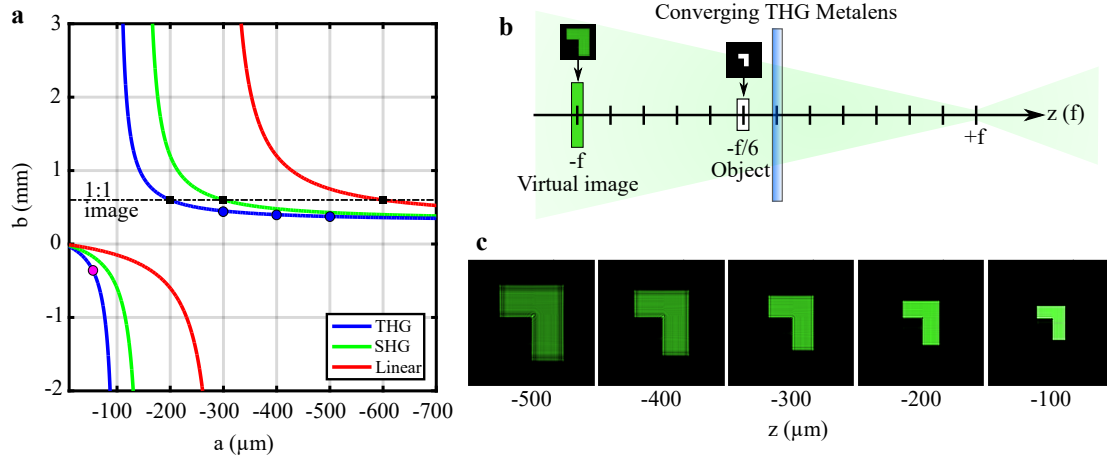


**Figure 4.10: Nonlinear virtual image formation with converging THG metalens.** **a** Plot of image distances  $b(n, a)$  versus object distances  $a$  in accordance to the generalized nonlinear lens equation. Linear (red), SHG (green), and THG image formation (blue) are shown for the same focal length of  $f = 300 \mu\text{m}$ . All produce a 1:1 image at an image distance of  $b = 2f = 600 \mu\text{m}$  (black rectangular dots). The blue dots indicate configurations used in the previous measurements and simulations for the THG lens. **b** Schematic illustration of a virtual image formation with a converging THG metalens. The object is placed at  $a = -f/6$  leading to a virtual image at  $b = -f$ . **c** Corresponding numerical simulation with beam propagation method that refers to the magenta point in **a**. Virtual THG image is formed at an image distance of  $b = -f = -300 \mu\text{m}$ .

## 4.4 Higher order nonlinear spatial correlations

In this section, further physical phenomena will be illustrated with regard to the image formation with THG metalenses. In the experiment, these were first noticed when objects were tried to be imaged from a relatively large object distance. Unlike the plasmonic SHG lens, several additional features appeared in the THG image that can be linked to higher order nonlinear spatial correlations. The phenomena become particularly clear in numerical simulations, in which two Gaussian beams cause interference phenomena on the metasurface.

### 4.4.1 TH imaging of multiple Gaussian beams interfering on the metalens

As a first step, the image formation of a ‘two-point source’ is numerically investigated: the interaction of a pair of Gaussian beams, whose beam waists are located in an object distance  $a = -500 \mu\text{m}$  in front of the metalens. The angle of incidence with respect to the metasurface is five degrees so both beams interfere exactly at the metalens position. In this example, the focal length of the metalens is chosen to be  $f = 250 \mu\text{m}$ . Then the nonlinear image formation from the metalens position at  $z = 0$  to  $z = 600 \mu\text{m}$  behind the metalens is simulated in the linear (red) and the nonlinear (THG, green) case (fig. 4.11 a, b). The interpolated surface plots of the intensity distribution in the axial direction are plotted for the linear regime (fig. 4.11 c, frequency  $\omega$ ), for third-harmonic generation (fig. 4.11 d, frequency  $3\omega$ ) and for second harmonic generation (fig. 4.11 e, frequency  $2\omega$ ). It can be observed that both Gaussian beams are imaged in the linear case at an image distance of  $b = 500 \mu\text{m}$  behind the metalens. In the nonlinear regime, an image of both Gaussian beams with the reduced FWHM (factor  $\frac{1}{\sqrt{n}}$ ) can be obtained at the same distance  $b$ . However, an additional central signal between both Gaussian beams for the SH case and two additional signals for the TH case can be found, which propagate exactly at the vertically opposed half-angle ( $2.5^\circ$ ) with respect to the metasurface. This behavior can be explained by the interaction of different  $k$ -vectors at the nonlinear generation process. In the case of SHG (e), the outer circles are formed by  $2\omega$ -photons generated by  $\omega$ -photons from one Gaussian beam (both photons from either the left or the right beam). The central signal originates from  $2\omega$ -photons generated by two  $\omega$ -photons from each input Gaussian beam (e.g. one  $\omega$ -photon from the left beam and one  $\omega$ -photon from the right beam). The case of THG can be explained in the same way as a three photon mixing process. In fig. 4.11 f, the one-dimensional intensity distribution of the two input Gaussian beams at the object distance  $z = -500 \mu\text{m}$  (red) is shown and its autocorrelation (blue) is calculated mathematically. The cross-correlation of the input intensity distribution and its autocorrelation is calculated as well (green). Herein, fig. 4.11 demonstrates how the nonlinear metalenses can be used to optically execute mathematical operations that resemble autocorrelations (SHG metalens) or higher-order autocorrelations (THG metalens).

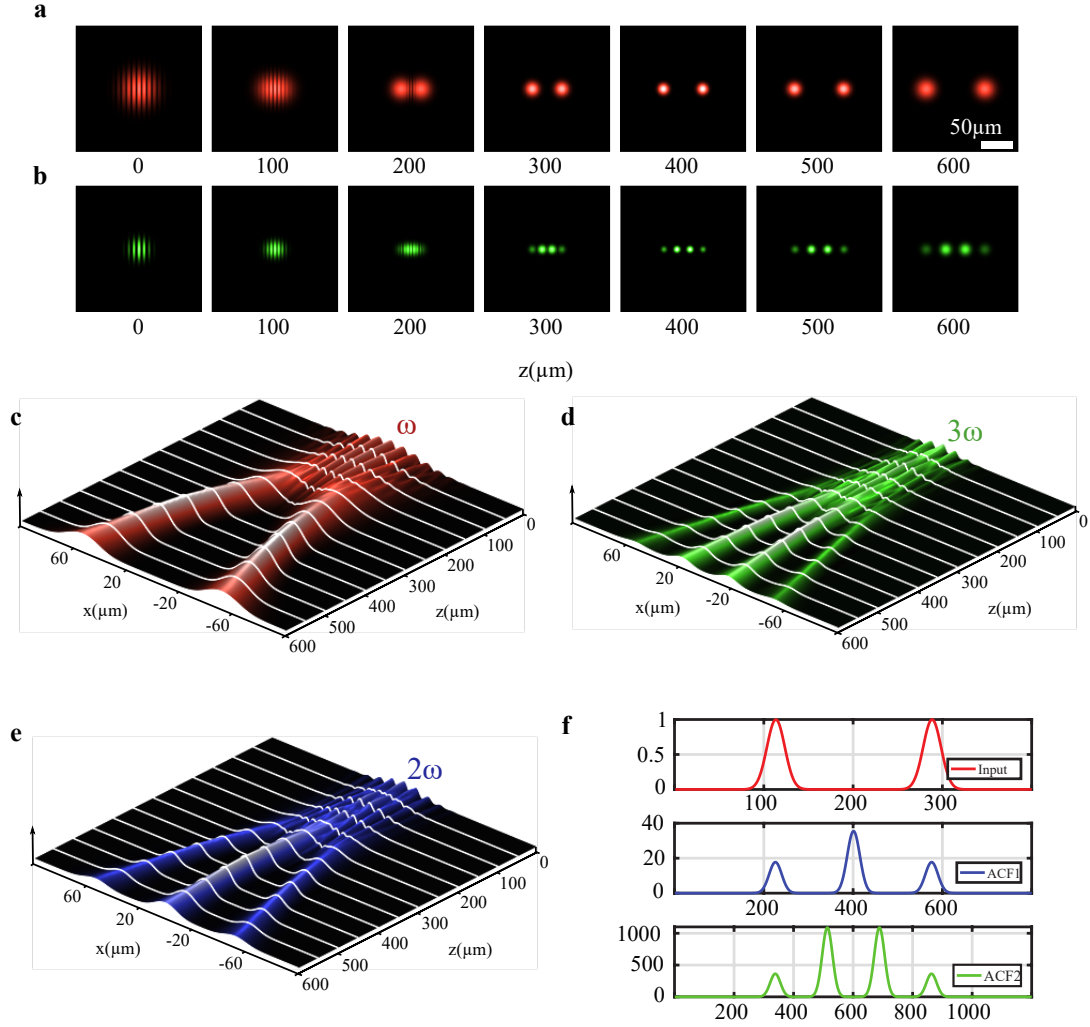


**Figure 4.11: Simulation of the image formation of two Gaussian beams.** **a-b** Simulation of different transverse intensity distributions along the optical axis with the help of the beam propagation method in the linear (red) and the nonlinear case with a metalens for THG (green). The metalens is illuminated by two Gaussian beams, which interfere at the lens position. **c-e** corresponding interpolated surface plots for the image formation in the linear case (red), for THG (green) and SHG (blue). **f** The 1D intensity distribution of two Gaussian beams (Input, red) is taken as an input for the mathematical execution of an autocorrelation function (ACF1, blue) and a higher-order autocorrelation function (ACF2, green), which is just the cross-correlation function of the input and ACF1.

#### 4.4.2 Experimental demonstration of TH imaging of two apertures

The actual interaction of multiple Gaussian beams on the metasurface has also been investigated experimentally. It required the use of an additional tunable delay line to adjust the temporal coherence of the two beams. However, the experiment proved to be unfeasible so far because the home-built delay line was too inaccurate. Therefore, to verify the simulations experimentally, circular apertures are used as real objects in front of the nonlinear metalens to represent multiple Gaussian beams. The apertures are fabricated with standard electron beam lithography and etching into a 100 nm thick chromium layer. Each circular aperture has a diameter of 60  $\mu\text{m}$  and the distance between them is 140  $\mu\text{m}$ .

The fundamental light propagates through the two apertures and diffracts during the propagation in the linear regime (see fig. 4.12a, b). To obtain the interaction of many different  $k$ -vectors, interferential effects at the metalens position are increased by choosing a comparatively large object distance of  $a = -3\text{ mm}$ . The signal interferes at the metalens surface and is partially converted to the third-harmonic wavelength. The added spatial phase information by the metasurface results in a focusing of the TH light. The resulting distribution of the THG signal along the optical axis is shown in fig. 4.12c. Since the fundamental light reaching the metalens possesses spatial coherence, the generated nonlinear signal possess new spatial frequencies leading to two additional maxima of the TH signal in the image plane (see fig. 4.12d). Hence, the nonlinear image formation can be associated with a higher-order nonlinear correlation process. At the location of the image plane ( $z = 465\text{ }\mu\text{m}$ ), four THG intensity maxima instead of two expected spots for linear optics are observed. The resulting THG image can be understood in the following way: the larger outer circles are formed by  $3\omega$ -photons generated by  $\omega$ -photons all coming from the same aperture (either top or bottom). Both inner smaller circles originate from three  $\omega$ -photons generated by  $\omega$ -photons from both apertures (e.g. one  $\omega$ -photon from the bottom aperture and two  $\omega$ -photons from the top aperture). Hence, the image formation is associated with a third-order spatial autocorrelation function of the apertures, carrying information about spatial coherence of light coming from the object. The magnitude of the higher-order auto-correlation features found at the image plane grows with the increase of the ratio  $\frac{|a|}{l}$ . The experimental results are supported with numerical calculations using a beam propagation method. The results of the corresponding theoretical calculations are shown in Fig. 4e-h.

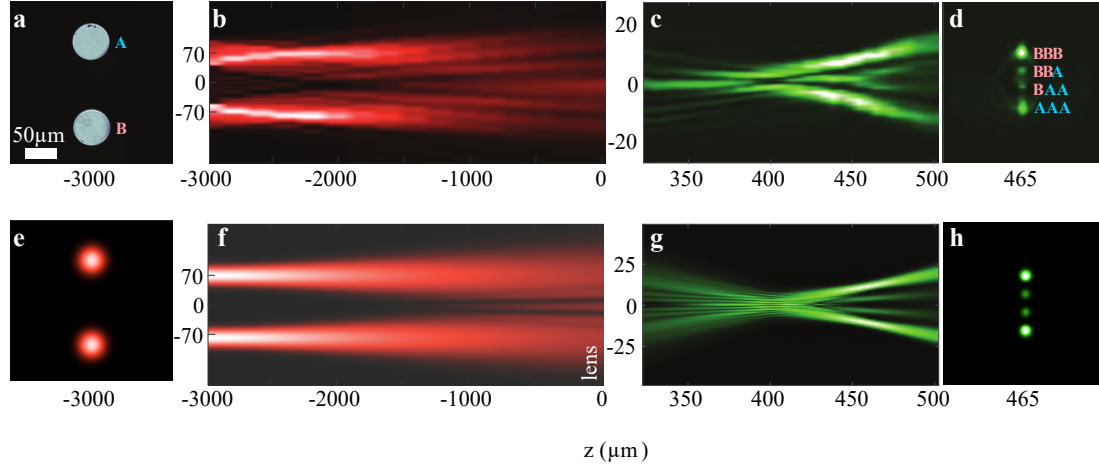


**Figure 4.12: Nonlinear imaging and spatial correlation for two apertures.**

Upper row: **a** White light image of the two circular apertures (A and B) in front of the metalens. **b** Measured axial intensity distribution of the fundamental wave between object and metalens position. Both apertures are simultaneously illuminated with a weakly collimated beam at  $\lambda = 1550 \text{ nm}$ . **c** Measured intensity distribution of the THG intensity along the optical axis near the focusing and imaging planes of the two apertures. **d** Cross-section of the corresponding TH intensity  $465 \mu\text{m}$  after the metalens showing the formation of four maxima associated with the third-order spatial autocorrelation function of the object. **e-h** Corresponding numerical simulation with nonlinear beam propagation method: beam waist of two Gaussian beams is located in the object plane. The fundamental and third-harmonic axial intensity distribution as well as the image plane cross-section is illustrated.

#### 4.4.3 Experimental demonstration of TH imaging of three apertures

A more complex photon interaction is investigated by adding a third circular aperture to the object (aperture C in fig. 4.13a). At a distance of  $b = 465 \mu\text{m}$  behind the metalens a similar higher order correlation process can be observed (fig. 4.13b), which shows two additional maxima on every side of the triangular arrangement. The distance between the additional maxima on the longer side  $AC$  is greater than on the shorter sides  $BC$  and  $AB$ . Additionally, one can find one central maximum at frequency  $3\omega$  resulting from three  $\omega$ -photons coming from each of the three circular apertures. This experiment is matched with theoretical calculations using the nonlinear beam propagation method (fig. 4.13c, d).

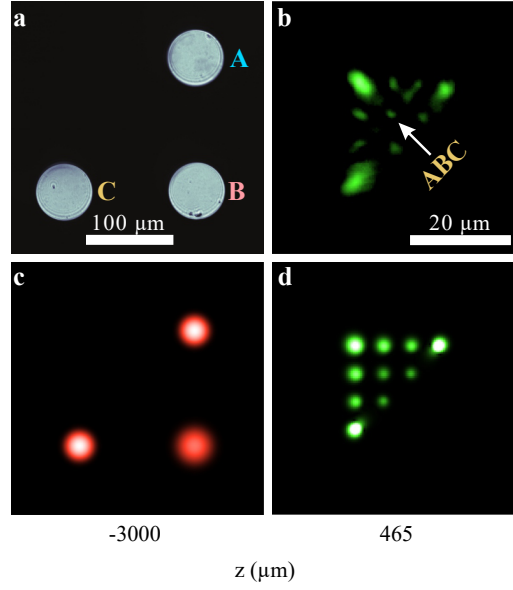


**Figure 4.13: Nonlinear imaging and higher-order spatial correlations for three apertures.** Upper row: **a** Microscopic image of three apertures, illuminated simultaneously at the object distance  $a = -3$  mm. **b** The corresponding experimentally obtained TH intensity distribution at  $b = 465$   $\mu\text{m}$  behind the metalens shows the formation of 10 maxima associated with the third-order autocorrelation. The marked spot corresponds to the THG signal obtained via nonlinear conversion of  $\omega$  photons from all three apertures. **c-d** Corresponding numerical results obtained with the beam propagation method. Beam waists of three Gaussian beams are located in the object plane. The waist and the intensity of the lower right beam is chosen to be slightly different to the other two beams to reproduce experiment more accurately.

## 4.5 Conclusion

In summary, the imaging with a nonlinear all-dielectric metalens was demonstrated, both experimentally and theoretically. An efficient design of a nonlinear dielectric metalens is employed based on the generalized Huygens' principle. This nonlinear metalens facilitates higher-order spatial correlation effects originating from the nonlinear frequency conversion not available in the linear regime. The conditions to maximize and minimize the additional higher-order autocorrelation features at the image plane were illustrated. Based on the experimental observations, a generalized form of the Gaussian lens equation is formulated for imaging through general nonlinear lenses, which is in analogy to the well-known thin-lens equation in linear ray optics. The modified lens equation predicts correctly the size and location of the formed nonlinear image in the experiments. However, this model is limited to

---

simplifications by assuming an object position close to the lens and a plane-wave illumination. Nonlinear metalenses provide a future platform for applications in nonlinear information processing, including pattern recognition based on higher-order spatial correlations [McL68]; all-optical higher-order Fourier transformations; short laser pulse diagnostics; and spatial photon correlation and coherence measurements.



# CHAPTER 5

---

## Linear metalenses for integration in optical tweezers

---

Dynamic control of compact chip-scale contactless manipulation of particles for bioscience applications remains a challenging endeavor, which is restrained by the balance between trapping efficiency and scalable apparatus. Metasurfaces offer the implementation of feasible optical tweezers on a planar platform for shaping the exerted optical force by a microscale-integrated device. In this chapter a highly efficient silicon-based metalens for two-dimensional optical trapping in the near-infrared is experimentally demonstrated [Cha20]. The use of high-efficiency metalenses in optical tweezers provides a user-friendly and easy-to-implement application in the linear regime that can be realized with continuous wave lasers. At the same time, the fabricated metalenses also offer new functionalities that cannot be realized with traditional optical tweezers. The metalens concept is based on the Pancharatnam-Berry phase, which enables polarization-sensitive particle manipulation. The optical trapping setup is capable of adjusting the position of both the metasurface lens and the particle chamber freely in three directions, which offers great freedom for optical trap adjustment and alignment. Two-dimensional (2D) particle manipulation is done with a relatively low-numerical-aperture metalens ( $\text{NA}_{\text{ML}} = 0.6$ ), which allows for 2D polarization-sensitive drag and drop manipulation of polystyrene particles suspended in water. Furthermore, the transfer of angular orbital momentum to these particles with a single tailored beam is experimentally demonstrated. These functionalities may open new possibilities for lab-on-a-chip optical trapping for bioscience applications and microscale to nanoscale optical tweezers.

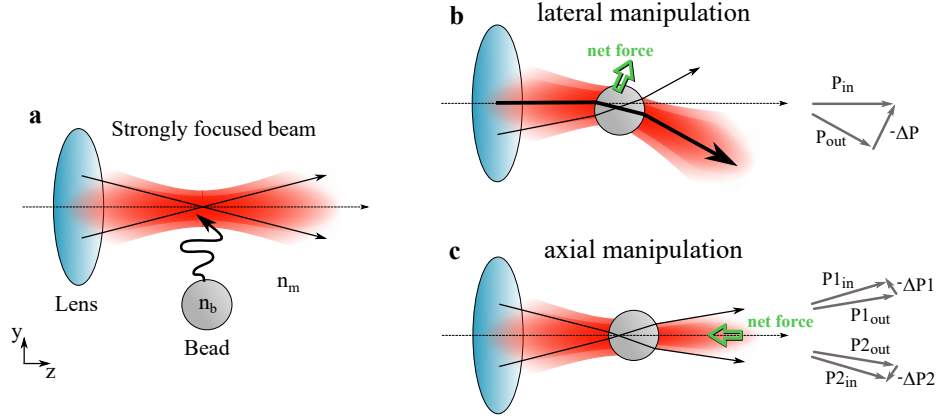


**Figure 5.1: Ray optics explanation of the momentum conservation in optical tweezers.** **a** Dielectric particle with refractive index  $n_b$  is freely suspended in water with lower refractive index  $n_m = 1.33$ . It enters an optical trap created from a strongly focused beam. **b** Individual rays of light are refracted at the interfaces of the bead and the surrounding medium. When the bead is laterally displaced from the beam center (in  $xy$ -dimension), more intense rays are refracted away from the beam center indicating a momentum change  $\Delta P$ . There is an equal and opposite momentum change  $-\Delta P$  on the particle resulting in a net force that pulls the particle to the center of the beam. **c** When the bead is axially displaced from the beam center (in  $z$ -dimension), rays of light are symmetrically refracted resulting in a momentum change  $\Delta P_1 + \Delta P_2$  that causes an axial net force on the particle towards the beam center.

## 5.1 A short introduction to optical tweezers

Nowadays, optical tweezers as a cutting-edge technology pave the way to new intriguing application opportunities in the fields of biophotonics and biomedical research, such as studies of cell interaction, embryology, cancer research, or molecular motor characterization [Dho11; Joh16; Li19; Sur05]. In this context, optical micromanipulation includes not only trapping by a noncontact force but also single-cell manipulation, alignment, and sorting of mostly micrometer-sized dielectric particles [Chi05; Gri03; Mac03]. Furthermore, digital holographic optical tweezers can be used to generate individual traps to transfer orbital or spin angular momentum and enable particle circulation and spinning [Gar02; Mag18; Pad11]. To obtain a stable trapping potential, the gradient force of a tightly focused beam must balance the scattering force exerted on the particle by Fresnel reflections [Ash70]. Particles are attracted along the electric field gradient to the focal region of most intensity. A physical explanation is provided by the conservation of momentum in the ray optics model (fig. 5.1). However, it can only be used if the particle sizes are significantly larger

than the optical wavelength  $\lambda$ . The model is presented by a dielectric particle with refractive index  $n_b$  that moves randomly into an optical trap of strongly focused laser radiation. Individual rays of light are refracted at the interfaces of the bead and the surrounding medium causing a change in the direction of the light propagation. In case of a particle displaced from the beam axis (fig. 5.1 b), stronger rays are refracted in the direction of the displacement. According to Newton's third law, the induced change of light's momentum  $\Delta P$  evokes an equal and opposite lateral net force on the particle [Cha06]. In case of an axial displacement of the bead (fig. 5.1 c), both rays are symmetrically refracted resulting in a momentum change  $\Delta P_1 + \Delta P_2$  that causes an opposite axial net force on the particle towards the beam center. While the lateral manipulation of the particle can also be realized by the intensity distribution of an unfocused laser beam, the axial manipulation requires strongly focused laser beams. In the incident cone of light, rays close to the optical axis contribute little to the trapping, but much to the scattering force (associated to reflection and absorption) [Afz92]. Thus, especially beams that are strongly diffracted by the lens contribute sufficiently to the backward axial net force on the particle. Therefore, particle manipulation is typically accomplished with the use of high-numerical-aperture (NA) microscope objectives. Current research on optical tweezers is directed towards the design flexibility and versatility in the field of applications, which can be greatly enhanced by replacing bulky and expensive optical elements, such as microscope objectives and spatial light modulators, with miniaturized devices in truly compact setups, suitable for integration into lab-on-a-chip systems. Benefitting from high degrees of freedom in phase modulation and manipulation of the focal characteristics, a polarization-sensitive plasmonic metalens was used to replace bulky refractive elements [Mar18; Suw19]. However, the relatively low diffraction efficiency of the plasmonic metasurfaces, which directly affects the optical trap efficiency, limits their applicability in optical trapping [Che15; Che12; Ni13a].

In recent years, all-dielectric metasurfaces made of low-loss and high-refractive-index materials have been introduced [Kho15; Kho16; Sau15; Yu15]. Compared to their plasmonic counterparts, they feature higher diffraction efficiency, lower absorption loss, and a larger optical damage threshold, making them a suitable candidate for application in optical tweezers [Xu18]. The utilization of a silicon metalens in optical trapping has been shown recently [Tka18]. The work demonstrated optical trapping with a reflection-based silicon metalens in a microfluidic environment. However, such reflection-based focusing elements require a double pass of the light through the fluidic system, which can increase damage to biological samples and reduce the focal spot quality by additional scattering processes.

## 5.2 Dielectric metasurfaces for integration in optical tweezers: Schematic Concept, Metasurface Design, and Nanofabrication

Here a versatile optical tweezers setup based on transmission-type all-dielectric silicon metasurface lenses is presented. This technique not only allows optical trapping of microbeads at a fixed position but also optical manipulation without using traditional optical elements. The shaping of the trapping beam intensity profile is done by adding a spatially variant phase modulation to the incident beam, which is based on the known Pancharatnam-Berry phase concept (see section 2.2.2). The abrupt phase change follows for circularly polarized light that is converted to its opposite helicity [Bom02]. This concept enables this device to work either as a convex or concave lens based on the used input circular polarization state [Che12; Ma17; Yu14]. In this way, polarization-sensitive two-dimensional (2D) drag and drop manipulation of polystyrene microbeads suspended in water is demonstrated. Furthermore, the concept is expanded to realize a dielectric vortex metalens, which was used to create a donut-shaped intensity distribution in the focal region without the need for an additional phase mask (q plate). Theoretical concepts for the orbital angular momentum (OAM) transfer with dielectric vortex metalenses already exist but have not yet been experimentally demonstrated [Ma17]. In this work, it is shown that optically trapped particles can indeed rotate in a circular motion based on the topological charge of the helical phase front. With this approach, metasurface-enhanced optical tweezers are demonstrated, which show a high transmission efficiency with simultaneous flexibility in beam shaping that can be used for a broad range of applications in miniaturized “lab-on-a-chip-ready” systems [Fig00].

### 5.2.1 Schematic Concept

The concept of the metalens optical tweezers is shown schematically in fig. 5.2a. An incident right circularly polarized Gaussian beam at 800 nm wavelength is collected by an ultrathin planar metalens and converted to a left circularly polarized beam that is focused at the designed focal length. Polystyrene microbeads, which have a refractive index higher than water, are optically trapped near the focal plane.

To implement the metalens, a 2D circular nanofin array made of amorphous silicon was designed and fabricated. The radially changing rotation angle  $\theta(r)$  of the nanofins is determined by the desired PB phase modulation  $\varphi(r) = 2\sigma\theta(r)$ , such that  $\theta(r)$  for a lens-like phase profile is

$$\theta(r) = \frac{\sigma}{2}k_0(\sqrt{f^2 + r^2} - |f|), \quad (5.1)$$

where  $\sigma = \pm 1$  stands for left or right circular polarization (LCP or RCP),  $k_0 = \frac{2\pi}{\lambda}$  is the free-space wave vector,  $r$  is the distance of the nanofin from the center of the lens and  $f$  is the focal length of the metalens [Che15; Che12].

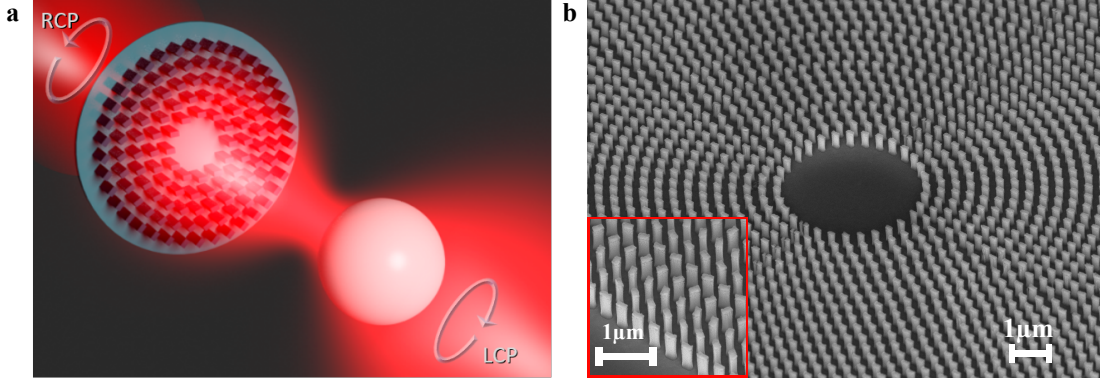


**Figure 5.2: Schematic concept and SEM image of the all-dielectric metalens.** **a** The conceptual image illustrates the trapping of a polystyrene microbead with the help of an all-dielectric metalens, that converts an RCP incident Gaussian beam to a focused LCP beam. **b** SEM image of the fabricated metalens that consists of amorphous silicon nanofin array. The red inset shows a region at the edge of the metalens.

### 5.2.2 Rigorous Coupled Wave Analysis

By using rigorous coupled-wave analysis (RCWA) with periodic boundary conditions, the optimal structure sizes were found for silicon nanofins on a glass substrate. The method is based on a Fourier modal method as a special frequency solver, which numerically solves the time-harmonic Maxwell's equations for the design wavelength [Wei11]. A nanofin scatterer with length  $L$ , width  $W$ , and height  $H$  is placed in the center of a quadratic unit cell with a periodicity  $P$  (center-to-center spacing). In order to keep the compatibility with top-down nano-fabrication, the parameter sweep for  $L$ ,  $W$  and  $P$  is done while keeping the height  $H$  fixed. As described in section 2.2.2, efficient Pancharatnam-Berry phase control requires nanostructures to work as local half-wave plates. Therefore, the transmission efficiency for a polarization conversion from one circular state of polarization to the other needs to be maximized [Geo19]:

$$T_{\text{cross}} = \frac{1}{4} |t_{xx} - t_{yy} + i(t_{xy} + t_{yx})|^2, \quad (5.2)$$

where the transmission matrix is

$$t = \begin{pmatrix} t_{xx} & t_{yx} \\ t_{xy} & t_{yy} \end{pmatrix}. \quad (5.3)$$

Details of the design optimization method can be found in an earlier work [Geo19]. Accordingly, the nanofin geometries are set to the length of  $L = 200$  nm, the width

of  $W = 120$  nm, and the center-to-center spacing of  $P = 360$  nm (fig. 5.2 b).

### 5.2.3 Nanofabrication

Three different kinds of all-dielectric silicon metasurfaces were used for the experimental study. A metalens, a linear phase gradient metasurface, and a vortex metalens were fabricated on a 1.1 mm thick glass substrate using silicon deposition, electron beam patterning, and reactive ion etching [Rei19]. At first, a 600-nm-thick amorphous silicon (a-Si) film was prepared through plasma-enhanced chemical vapor deposition (PECVD). Then poly-methyl-methacrylate (PMMA) resist layer was spin-coated onto the a-Si film and baked on a hot plate at 170°C for 2 minutes. Next, the nanofin structures were patterned by using standard electron beam lithography (EBL). The sample was then developed in 1:3 Methyl isobutyl ketone (MIBK): Isopropyl alcohol (IPA) solution and washed with IPA before being coated with a 20-nm-thick chromium layer using electron beam evaporation. Thereafter, a lift-off process in acetone was executed to remove the remaining PMMA from the surface. Inductively coupled plasma reactive ion etching (ICP-RIE) was used to transfer the structures from the chromium mask to silicon. After dry etching the silicon, a thin layer of chromium mask was left on top of the silicon nanofins and a wet etching process was used to remove the residual chromium mask completely ( see fig. 5.2 b).

### 5.2.4 Optical Characterization of the Metalens and Vortex Metalens

In fig. 5.3 a-b the impact of the polarization-dependent phase modulation is shown by measuring the beam intensity profile along the propagation direction  $z$  for different circularly polarized beams incident on the metalens (see also fig. 5.6 b). For that, snapshots of the transverse intensity profiles in incremental steps of 5  $\mu\text{m}$  over the total distance of 825  $\mu\text{m}$  were taken (for RCP and LCP incident light, respectively). The profiles correspond to axial cross-sections of image stacks obtained from different transverse planes. Nearly identical real and virtual focal spots with an FWHM of 0.9  $\mu\text{m}$  are observed at the designed real and virtual focal planes of  $z = f = \pm 530$   $\mu\text{m}$  (fig. 5.3 c-f). The numerical aperture of the metalens in air is  $\text{NA} \approx 0.6$ . The diameter of the metalens is 800  $\mu\text{m}$ .

The metalens diffraction efficiency is crucial for the application in optical tweezers. Note that any polarization-unconverted light (same polarization as the incident polarization state) does not carry the metalens phase information and therefore is not contributing to the focusing. It only increases the radiation pressure on the particle and decreases the trap efficiency. The metasurface diffraction efficiency was measured by using a metasurface diffraction grating, which is fabricated with silicon nanofin parameters identical to those of metasurface lenses on the same substrate. A conceptual schematic of the measurement is illustrated in fig. 5.4a. A focused circularly polarized Gaussian beam incident on the grating is partly converted to the cross-circular polarization at the metasurface position (RCP to LCP or LCP

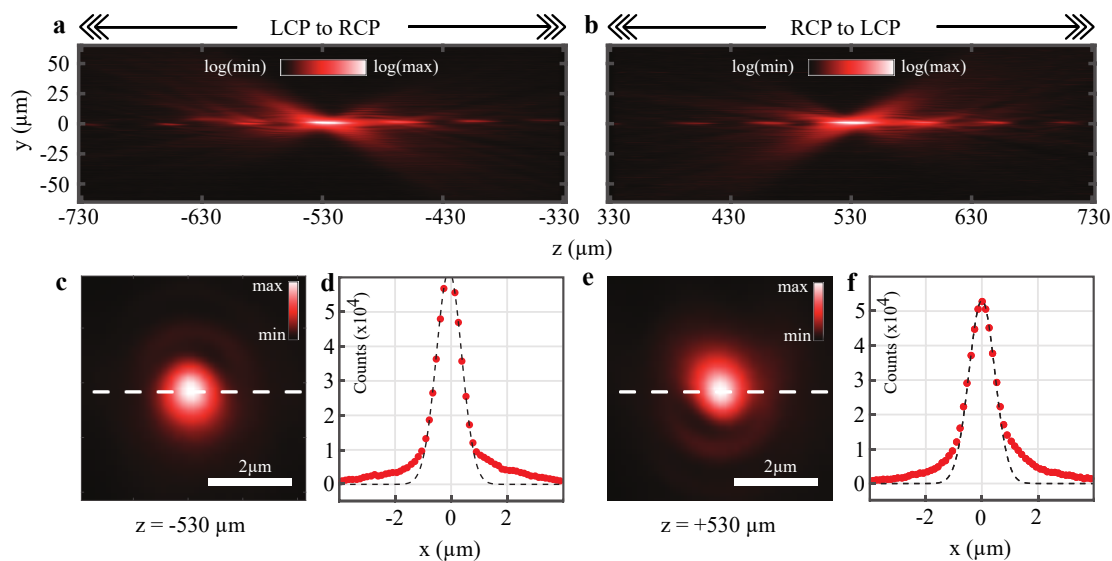


**Figure 5.3: Optical characterization of the all-dielectric metalens.** **a** and **b** Cross-sections of the intensity distribution of the focused beam along the optical axis for incident beams with different circular polarizations, drawn on a logarithmic scale. For LCP (RCP) illumination, the metalens acts as a concave (convex) lens, which results in a virtual (real) focal point at  $z = -530 \mu\text{m}$  ( $z = +530 \mu\text{m}$ ). The metalens is located at  $z=0$ . **c** and **e** Transverse intensity distributions at the virtual (real) focal point position, drawn on a linear scale. **d** and **f** Red dots: 1D intensity cross-sections along the white dashed line shown in panel **c** and **e**, respectively. Black dashed line: Gaussian fits to the measured data points, which provide an FWHM of  $0.9 \mu\text{m}$  in both considered cases.

to RCP) and then deflected by the introduced phase grating into the 1st or -1st diffraction order, while the unconverted part of the incident beam causes the 0th diffraction-order in co-circular polarization (RCP to RCP or LCP to LCP). To determine the diffraction efficiency, the k-space intensity distribution was measured for all combinations of input and output circular polarization states (fig. 5.4b, see also fig. 5.6c for detailed experimental setup). The diffraction efficiency is defined by the ratio of the desired cross-polarized light intensity that is diffracted into the first order to the total amount of light that was transmitted by the metasurface. Diffraction efficiencies of 82.1% for LCP and 83.7% for RCP input light are obtained. From that, the polarization conversion efficiency is determined by multiplying the diffraction efficiency by the transmission coefficient [Qin16]. The transmission coefficient is defined by the ratio of the total intensity transmitted through the metasurface compared to the intensity transmitted through the glass substrate. From these values, the overall conversion efficiency for the converging metalens and vortex

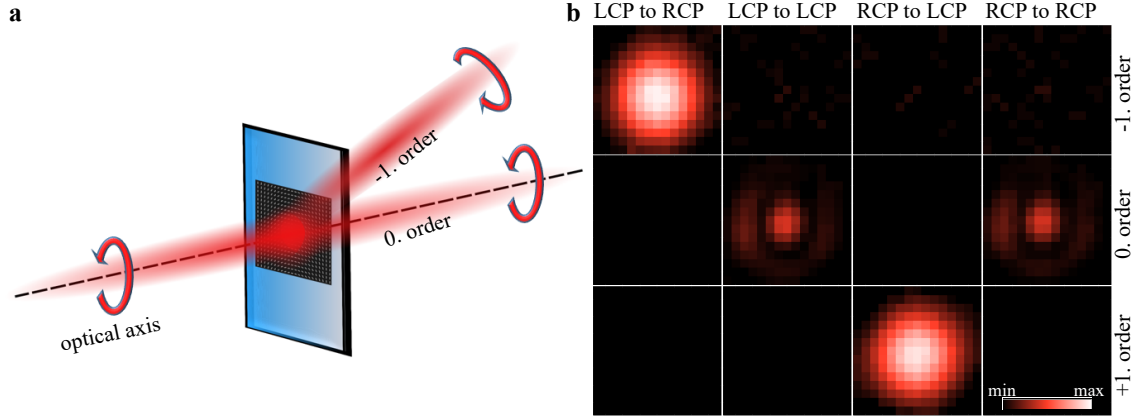


**Figure 5.4: Measurement of the metasurface diffraction efficiency.** **a** Schematic image of the diffraction efficiency measurement: The metasurface diffraction grating with LCP incident light deflects the RCP beam to the  $-1$ st order of diffraction, while the unconverted LCP part remains at 0th diffraction order. **b** The cross-section intensity distribution of 1st, 0th and -1st order of diffraction for the incident LCP and RCP beams, further divided into the respective co- and cross-polarization states.

metalens was estimated to be 70.8%.

As a next step, the optical properties of the vortex metalens were characterized in the same way as for the regular metalens (fig. 5.5a-f). For fabricating the vortex metalens, the metasurface design flexibility can be used to superimpose the spherical phase profile of the regular lens with a helical phase factor  $\varphi_{\text{hp}}(x,y) = m \arctan(x/y)$  that generates a high-quality donut-shaped intensity distribution with a topological charge of  $m = \pm 4$ , whereas  $x$  and  $y$  are the center coordinates of each nanofin (fig. 5.5 c-f) [Ma17]. Depending on the input circular polarization, the phase modulation of the vortex metalens is reversed resulting in either a real focusing vortex beam with a topological charge of  $m = +4$  for an incident RCP beam or a virtual focusing vortex beam with inverted OAM helicity ( $m = -4$ ) for an incident LCP beam. The vortex metalens has a diameter of  $d_{\text{max}} = 400 \mu\text{m}$  and a focal length of  $f_{\text{ML}} = 545 \mu\text{m}$ , corresponding to a numerical aperture of  $\text{NA} \approx 0.35$ .

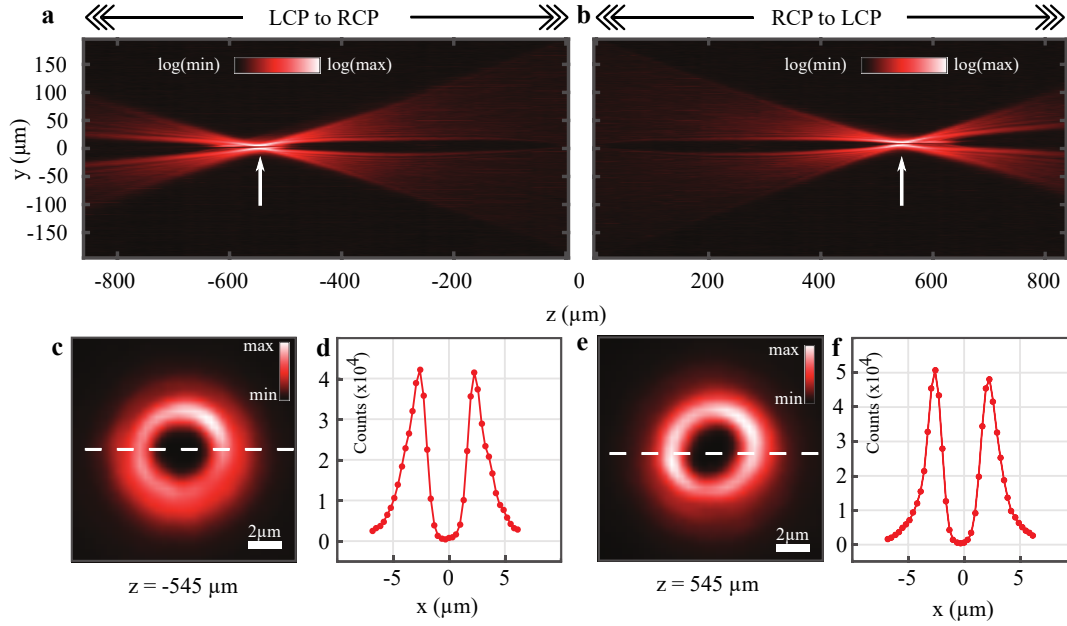


**Figure 5.5: Optical characterization of the vortex metalens.** **a** and **b** The cross-section intensity distributions of the beams converted by the vortex metalens along the optical axis on a logarithmic scale for better visibility. For LCP to RCP (RCP to LCP) conversion, the metalens acts as a concave (convex) vortex lens, which results in a virtual (real) focal point at  $z = -545 \mu\text{m}$  ( $z = +545 \mu\text{m}$ ). The helical phase factor results in zero intensity on the optical axis in the focal region. **c** and **e** Transverse intensity distributions of the donut-shaped beam profiles at the focal point positions indicated by white arrows in panels **a**, **b** drawn on a linear scale. **d** and **f** Red dots: 1D intensity cross-sections along the white dashed lines shown in panels **c** and **e**, respectively.

### 5.3 Metasurface enhanced optical tweezers for two-dimensional particle manipulation

Next, the performance of the different fabricated metalenses is characterized for the optical trapping of microbeads.

#### 5.3.1 Experimental Setup

The metalens optical tweezers setup is shown in fig. 5.6a. A continuous-wave Ti:sapphire laser at a fixed output wavelength of 800 nm was used as the light source. The laser power was adjusted with a HWP placed in front of a fixed Glan-Taylor polarizer. By adjusting the QWP, different input circular polarizations can be generated. The laser beam was weakly focused by a regular convex lens ( $f_1 = 500 \text{ mm}$ ) in such a way that the beam waist was slightly larger than the metalens diameter. A

non-polarizing 50:50 beam splitter directed both the circularly polarized input beam and the collimated white light illumination onto the sample. The laser beam reflected from the beam splitter was used for power measurement. The metalens focused the RCP beam into the polystyrene microbeads solution contained in a sample chamber formed by a concavity glass slide and a cover glass. Both the metalens and the sample chamber were adjusted freely using independent three-dimensional translation stages. The laser beam profile and the white light image of the microbeads at the same lateral plane were imaged on the CMOS camera (Thorlabs DCC1545M) by a Nikon CFI60 Plan Epi infinity-corrected microscope objective ( $\times 100/0.8$ ) and a tube lens ( $f_{\text{TL}} = 200$  mm). To block the laser power and track the particle positions, a short-pass filter was placed in front of the camera. The experimental setup can be easily switched to the optical characterization measurements, such as the propagation experiment (fig. 5.6b) and the diffraction efficiency measurement (fig. 5.6c).

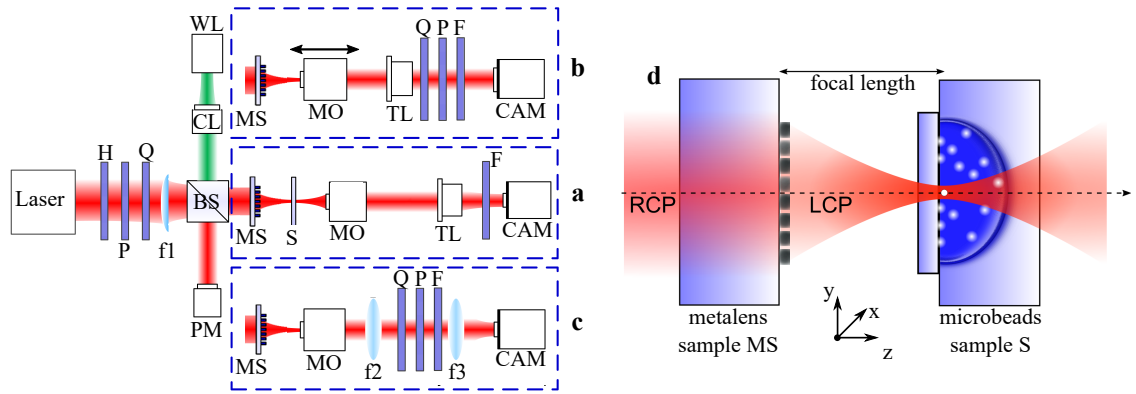


**Figure 5.6: Schematic illustration of the measurement setup.** A non-polarizing beam splitter (BS) is used to insert white light (WL) for sample illumination at the front side of the metasurface (MS - either metalens, vortex metalens, or metasurface diffraction grating) and to measure the incident laser power with a power meter (PM). Three different configurations can be used (blue dashed boxes): **a** Metalens-based optical tweezers system. Laser light with the desired polarization state is focused by the metalens onto the microbeads sample (S) while the focal plane of the metalens is imaged on the camera (CAM) through a microscope objective (MO) and a tube lens (TL). The polarization states were separated by a polarization analyzer consisting of a quarter-wave plate and a linear polarizer. **b** Optical propagation measurement setup. **c** Setup for efficiency measurement with the metasurface diffraction grating. **d** Arrangement of the MS and S in the metalens-based optical tweezers system. H - half-wave plate; Q - quarter-wave plate; P - linear polarizer; CL - collimating lens; F - filter;  $f_{1,2,3}$  - lenses.

### 5.3.2 Experimental Results and Discussions

For demonstrating the optical trapping, polystyrene microbeads (Polysciences Polybeads) were dispersed in purified water and the resulting suspension was loaded into a concavity glass slide (cavity depth 1.2 - 1.5 mm), which is sealed with a 140- $\mu\text{m}$  thick cover glass. In the experimental setup, the metalens sample and this cover glass were faced towards each other (fig. 5.6d). Hence, the working distance of the trapping metalens had to cover a small air gap between the metalens and the microbeads sample covered by the 140  $\mu\text{m}$  thickness of the cover glass. The real focal spot was then generated inside the spherical concavity. This configuration was the reason for working with a relatively large focal length ( $f > 500 \mu\text{m}$ ), but at the same time, it also offered great flexibility in the trap center adjustment and simple and easy switching between particles of different sizes. To switch to different particles, only the microbeads sample needs to be replaced but the metalens sample remains exactly in the focal plane of the incident beam.

#### Metalens optical tweezers for 2D Polarization dependent drag and drop

For the measurement, the metalens real focal spot is adjusted in an x-y-plane where polystyrene microbeads were attracted to the cover glass surface. Such surface adhesion forces like van der Waals and electrostatic interaction forces are known as DLVO forces [Pra17]. In a horizontal beam path configuration, the transverse (lateral) gradient force generated by the metalens focus was strong enough to maintain a stable trap in 2D at a laser power of 30 mW. It also stabilized the particles against the force of gravity that tried to pull the particles out of the trap in the  $y$ -direction. By tuning the input circular polarization, particles were either be trapped and dragged in the medium (operation as converging metalens) or they were attracted by the surface of the cover glass (operation as concave metalens). Therefore, the 2D gradient force as well as the radiation pressure can be tuned actively by the ellipticity of the polarization state. The converging metalens for RCP input generated a focal spot that was smaller than the particle diameter. Thus, the radiation pressure on the particle increased while it was also partly counteracting the attraction between particle and cover glass. For the 2D lateral trapping, the particle was attracted by the trap center and could be dragged through the solution by moving the microbeads glass slide sample. To drop the particle at the intended location, only the input circular state of polarization was changed, so that the metalens would now work as a concave lens and the beam diverges. Therefore, the radiation pressure on the particle vanished and the particle stuck to the cover glass again. For demonstration purpose, different lateral pattern in the form of the letters M, E, T and A were arranged with

different particle diameters ranging from 2.0 to 4.5  $\mu\text{m}$  (fig. 5.7a-d).<sup>1</sup>

The lateral trapping stiffness was evaluated by standard calibration methods that are based on the particle motion in a stationary optical trap (fig. 5.7e) [Mal02; Ost10]. For that, the MATLAB UmUTracker was used to track particle trajectories of the polystyrene microbeads that freely sank to the bottom in the horizontal optical tweezers setup (particle diameter 4.5  $\mu\text{m}$ ) [Zha17]. These results were compared with particles that sank through the 2D optical trap generated by the metalens of  $\text{NA} \approx 0.6$ . The velocity with which the particle was attracted to the trap is tracked for different laser powers from 20 to 90 mW. The power  $P$  in the trapping plane is reduced due to the metasurface overall efficiency and interface reflections. It was found that the maximum lateral trapping forces acting on the bead are lower than  $F^{\text{max}} < 2$  pN. The accuracy of the calibration procedure depends on the precision of particle position tracking, which in the system is limited by the magnification of the imaging system and the framerate of the used camera. It is assumed that the trapping potential is harmonic following a linear dependence of the lateral optical force on the particle distance from the beam axis. The linear fit of the radial stiffness  $k_r$  versus power  $P$  yields the power normalized radial stiffness of  $K_r \approx 7.53$   $\text{pN}\mu\text{m}^{-1}\text{W}^{-1}$ , which agrees with values reported in other works under similar experimental conditions [Mar18]. The trapping efficiency is

$$Q_r = k_r r_{\text{max}} \frac{c}{n_m P}, \quad (5.4)$$

where  $\frac{c}{n_m}$  is the speed of light in the viscous medium and  $r_{\text{max}}$  is the maximum displacement. An efficiency of  $Q_r \approx 0.004$  was obtained. The measurement results are confirmed with radial stiffness simulation based on the Generalized Lorentz-Mie theory (GLMT), [Nie07] which is illustrated in fig. 5.7f. As input parameters, the focal spot size from the optical characterization measurement is broadened by a factor of four in the actual metalens optical tweezers system (fig. 5.6a). Furthermore, the wavelength was set to 800 nm, and the focal length to 530  $\mu\text{m}$ . The simulation shows the trap stiffness landscape for different particle diameters and relative refractive indices. For polystyrene particles in water, the relative refractive index is  $\Delta n \approx 1.19$  and for a particle diameter of 4.5  $\mu\text{m}$  the power normalized radial stiffness is found to be  $K_r \approx 9.5$   $\text{pN}\mu\text{m}^{-1}\text{W}^{-1}$ . Note that the model predicts that small changes in particle size lead to large changes in trapping stiffness and therefore, simulation and experiment should be compared with caution.

---

<sup>1</sup> Video files of the M-shaped particle arrangement can be found in the supplementary material of the original work[Cha20] (Visualization 1)

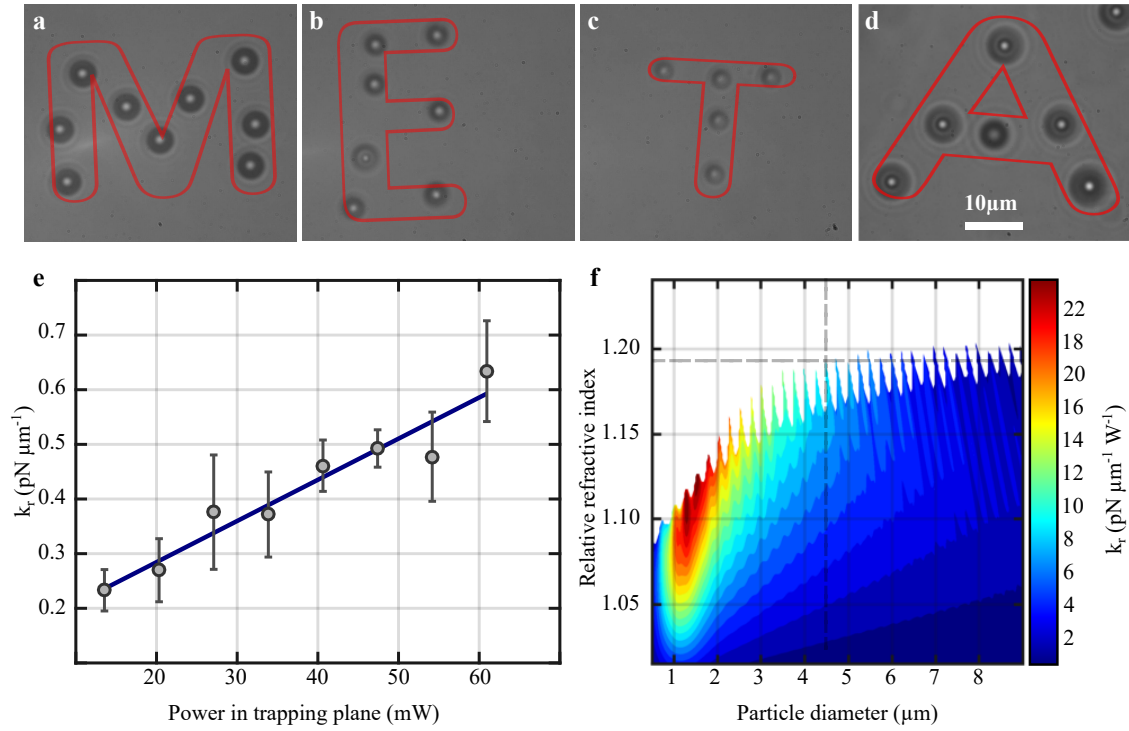


**Figure 5.7: Metasurfaces for 2D polarization-sensitive drag and drop manipulation of particles.** Polystyrene particles with a diameter of **a** 4.5 μm, **b** 3.0 μm, **c** 2.0 μm, and **d** 4.5 μm are dispersed in water and arranged by polarization-sensitive drag and drop using the metasurfaces. **e** Radial stiffness  $k_r$  vs power in trapping plane  $P$  for polystyrene particles with a diameter of 4.5 μm. **f** GLMT simulation for the radial stiffness of optical trap with different particle refractive indices and various particle diameters. Dashed lines indicate the experimental values of the particle size and the relative refractive index.

### 5.3.3 Vortex Metasurfaces for OAM transfer with a single tailored beam

In a second metasurface optical tweezers experiment, the OAM transfer from the vortex metasurface to a polystyrene microbead is studied. The optical trapping part of the setup (marked with the blue dashed box in fig. 5.6a) is rotated by 90 degrees so that the gravitational force does not disturb the lateral rotation movement of particles in the x-y-plane (vertical optical tweezers setup with the gravitational force parallel to the z-axis). Only the sample with polystyrene microbeads of 4.5 μm diameter is used. The vortex focal spot with the topological charge of  $m = +4$  was adjusted to the lateral region where particles stuck to the cover glass (fig. 5.8a). The donut-shaped intensity distribution is marked with red dashed lines and a short-pass filter is put in front of the camera to block the laser radiation. The microbeads sample is moved laterally to trap only one particle onto the donut-shaped intensity distribution.

Next, it was observed that the polystyrene bead is undergoing a rotational movement along with the vortex beam profile at 19 mW laser power, consistent with the topological charge of the beam (see [Cha20], Visualization 2). The movement is tracked in the x-y-plane with the help of MATLAB UmUTracker (fig. 5.8b). However, the particle was pushed in the axial direction and left the lateral trap potential after approximately 35 seconds. The transient confinement might be caused by inhomogeneous illumination of the vortex metalens, which led to regions on the donut-shaped intensity distribution with lower intensity. After 30 seconds the microscope objective was readjusted about 12.5  $\mu\text{m}$  in the z-direction. Nevertheless, a clear movement along a circular path given by the intensity profile could be observed during that time. Lastly, the power dependence of the radial trap stiffness was calculated by repeating the calibration method for the vortex metalens (fig. 5.8c). The linear fit now yields a power normalized radial stiffness, which is reduced to  $K_r \approx 4.28 \text{ pN}\mu\text{m}^{-1}\text{W}^{-1}$  and a trapping efficiency of  $Q_r \approx 0.002$ .

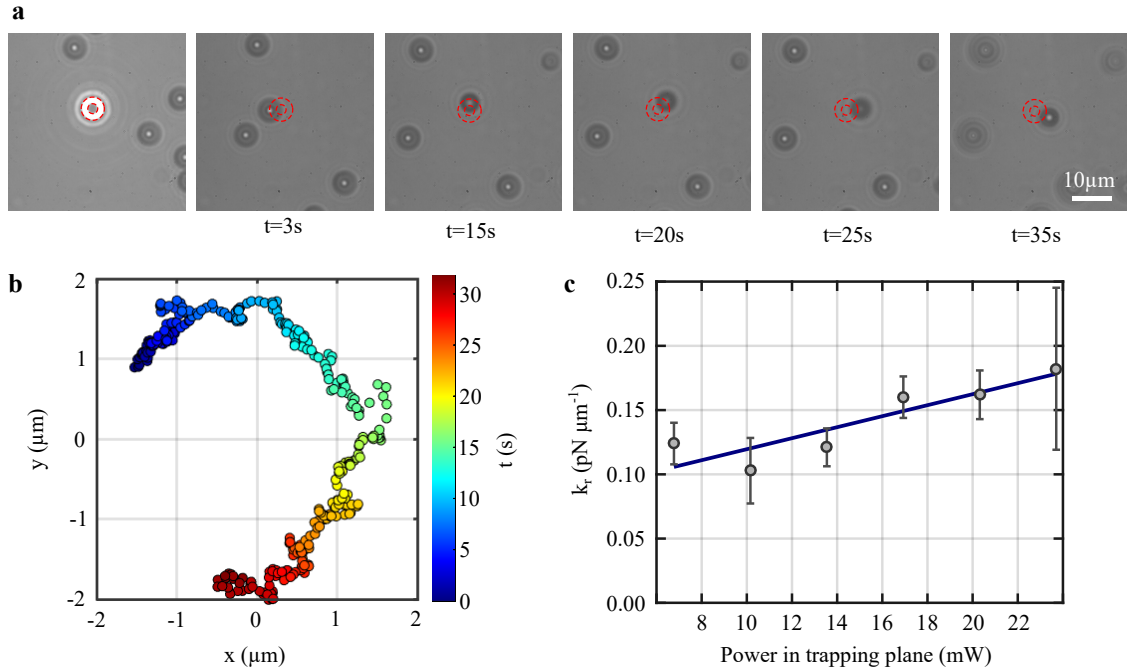


**Figure 5.8: Vortex metalens for OAM transfer** **a** Vortex metalens with a numerical aperture of  $\text{NA} = 0.35$  is used to generate a donut-shaped intensity distribution in the focal spot region. At  $t = 0\text{s}$  a particle ( $4.5 \mu\text{m}$  diameter) is attracted by the lateral gradient force. The orbital angular momentum is transferred onto the particle resulting in a clockwise rotational movement. Simultaneously, the particle is slowly pushed out of the trap in the axial direction **b** Trajectory plot of the particle's rotational movement. **c** Radial stiffness  $k_r$  of the vortex trap versus power in trapping plane  $P$ .

## 5.4 Conclusion

In summary, an efficient all-dielectric transmission-type metasurface made of Si nanofins was demonstrated for optical micromanipulation in 2D optical tweezers. The geometric Pancharatnam-Berry phase was utilized to enable a switchable metalens functionality. The metalens functions as a convex or a concave lens based on the circular input polarization. This concept was used to realize a polarization-sensitive drag and drop manipulation of polystyrene microparticles dispersed in water at a power-normalized radial stiffness of  $K_r \approx 7.53 \text{ pN}\mu\text{m}^{-1}\text{W}^{-1}$ . Furthermore, the OAM transfer onto particles was shown with the help of a vortex metalens, realizing both vortex beam generation and focusing by one single metasurface element. The radial stiffness per unit power was measured to  $K_r \approx 4.28 \text{ pN}\mu\text{m}^{-1}\text{W}^{-1}$ . Hence, no additional phase masks for beam shaping were required. The presented work may pave the way for future devices based on metalens optical tweezers with possible integration of electronically addressable liquid crystals. These can be utilized to switch the polarity of the metalens and to enable fully remotely controlled lab-on-chip optical tweezers.



# CHAPTER 6

---

## Summery and Outlook

---

The present work describes the realization and characterization of plasmonic and dielectric metalenses for various nanophotonic applications such as image formation using a nonlinear lens and integration into optical tweezers.

This work is motivated in particular by the fundamental question of how the principle of imaging changes when the conventional lens is replaced by an optical lens made of a nonlinear material. The answer to this scientific question is by no means trivial, since geometrical optics, on which the foundations of imaging in the linear regime are based, do not take into account the wave character of nonlinear optical processes. Experimentally answering the question with conventional nonlinear optical materials is not feasible because the phase-matching conditions of a lens-shaped bulky nonlinear crystal cannot be met. At this point, nonlinear plasmonic metasurfaces are introduced, since their subwavelength thickness significantly relaxes phase-matching requirements. In this context, nonlinear metasurfaces can contribute significantly to the understanding of fundamental research with regard to the nonlinear image formation with nanoscale devices.

Based on the selection rules for the generation of a nonlinear harmonic processes under illumination with circularly polarized light, ultrathin gold nanoantennas with three-fold rotational symmetry generate an instantaneous SHG response of the metasurface in the circular cross-polarization. At the same time, the fundamental light is unaltered in its propagation. This is in contrast to lenses made of regular nonlinear materials where linear and nonlinear beam propagation were manipulated. To achieve the arrangement of the C3 nanoantennas, a PMMA mask was selectively patterned by electron beam lithography followed by a subsequent metallization and the removal of the resist mask. The nanostructures were studied in more detail using linear and nonlinear spectroscopic methods. The maximum SHG signal is measured for a fundamental wavelength of approximately 1115 nm and it is stronger than that at the surface plasmon polariton resonance at 1085 nm. This redshift is a result of the resonance that measures the wavelength dependent strength of the far-field enhancement, while the nonlinear conversion is sensitive to the near field enhancement.

The desired phase profile was realized by a nonlinear Pancharatnam-Berry phase

that is governed by the meta-atom orientation angle and the spin state of the fundamental wave. Thus, the spin-dependent focusing effect of SHG waves was experimentally realized at both real and virtual focal planes at approximately  $\pm 100$ ,  $\pm 200$  and  $\pm 500$   $\mu\text{m}$ . Furthermore, real objects, which are illuminated by near infrared light, can be imaged at visible wavelengths based on the SHG process at the nonlinear metalens. Thus, illumination and detection wavelength are in different spectral ranges. The nonlinear lens offers a spin-dependent dual polarity that allows both virtual and real image formation. Simulations using beam propagation method in the nonlinear regime as well as the experimental results show an image formation which is not governed by the Gaussian lens equation. In particular, a real one-to-one image of the L-shaped slot-aperture was realized, where the object distance corresponds to the focal length. Interestingly, in linear optics this configuration would result in an image formation at infinity because the image distance would diverge.

Further experiments and simulations on the imaging of a double slit aperture reveal a central line in addition to the image in the SHG. This additional feature in the image is the result of the nonlinear process at the metalens that affects apertures which create an interference pattern at the metalens position. Despite the image distortion the experiment also serves as a demonstration of an 'AND' logic gate in the nonlinear regime. The weak central line is only present if both the signals from the two slits interact nonlinearly at the metasurface, whereas blocking either one or both of the two slits would result in disappearance of the central line.

The concept of nonlinear metalens not only inspires new imaging technologies but also provides a novel platform for generating and modulating nonlinear optical waves. In particular, nonlinear information processing could benefit from such concepts, like optical nonlinear Fourier transformation in integrated optical circuits.

Furthermore, it was shown that geometric phase controlled nonlinear metasurfaces based on C3 nanoantennas can be used for many other application possibilities. In this context, a metasurface for generating SHG signals carrying OAMs was demonstrated. It shows the first simultaneous control of spin and orbital angular momentum of light within a SHG process. Additionally, a new methodology is introduced to measure the SAM-OAM mode in the nonlinear regime with the help of on-chip metasurface interferometry.

The low SHG conversion efficiency from plasmonic metasurfaces could be greatly improved by aligning the optical resonances of metasurfaces with intersub-band transitions of quantum wells. In this way, nonlinear plasmonic metasurfaces, as a complementary alternative to conventional nonlinear optical crystals, may find a wide range of applications in optical switching, information technology, nonlinear wavefront shaping or frequency conversions.

The study of image formation in conjunction with a nonlinear process at the metasurface represents a new application of nonlinear metasurfaces and attracted a

lot of attention in the scientific community. Unlike many previous scientific works, well-known linear optical phenomena were not simply translated into the nonlinear regime, but rather the nonlinear process provides additional functionalities and physical insight into fundamental textbook physics of image formation. The topic was pursued further by also investigating image formation for higher harmonic processes (THG).

The image formation with an appropriate plasmonic nonlinear metalens for higher harmonic generations could not be demonstrated due to the low conversion efficiency and the low damage threshold. However, a more efficient design of a nonlinear all-dielectric metalens is employed based on the generalized Huygens' principle. Therefore, nonlinear all-dielectric metalenses are fabricated on a glass substrate following the processes of deposition, patterning, lift-off and etching. Employing silicon nanorods, a very common, in-expensive and extremely important semiconductor, provides high damage threshold for the nonlinear conversion in strong laser fields. For a linear input polarization, the silicon nanopillar resonators are designed to generate similar intensities of the nonlinear third-harmonic signal combined with directional forward scattering. Additionally, the different nanopillars provide different phase delays ranging from 0 to  $2\pi$  via the appearing geometric resonances at the THG frequency. The nonlinear metalenses reach a maximum diffraction efficiency for the THG of 48% at the design wave length of 1550 nm. The experimentally measured THG conversion efficiency is of the order of  $10^{-6}$ .

For the first time imaging with an all-dielectric metalens for THG was demonstrated experimentally and theoretically. Based on the experimental observations that also include former results from the plasmonic nonlinear lens, a generalized form of the lens equation is formulated for the imaging through general nonlinear lenses, which is in analogy to the well-known Gaussian lens equation in linear ray optics. The modified lens equation predicts correctly the size and location of the formed nonlinear image in the experiments. Additionally, it nicely demonstrates how fundamental concepts of image formation can be altered to describe also the nonlinear imaging processes.

Furthermore, the limiting effects of nonlinear image formation, already known from the plasmonic lens, were investigated in more detail. All nonlinear metalenses facilitate higher-order spatial correlation effects originating from the nonlinear frequency conversion that are not available in the linear regime. The conditions to maximize and minimize the additional higher-order autocorrelation features at the image plane were illustrated. Nonlinear metalenses provide a future platform for applications in nonlinear information processing, including pattern recognition based on higher-order spatial correlations, all-optical higher-order Fourier transformations, short laser pulse diagnostics, and spatial photon correlation and coherence measurements.

In addition to nonlinear imaging, there are other interesting applications for dielectric metalenses. Due to their high efficiencies, the integration into optical

tweezers as an ultracompact device is a natural choice. In this context, an efficient all-dielectric transmission-type metasurface made of Si nanofins was demonstrated for optical micromanipulation in 2D optical tweezers.

The metalens is characterized by an overall conversion efficiency of more than 70 % at the design wavelength of 800 nm. The geometric Pancharatnam-Berry phase was utilized again to enable a switchable metalens functionality. Based on the circular input polarization the lens features both a convex and a concave phase profile. This concept was used to realize a polarization-sensitive drag and drop manipulation of polystyrene microparticles dispersed in water at a power-normalized radial stiffness of  $K_r \approx 7.53 \text{ pN}\mu\text{m}^{-1}\text{W}^{-1}$ .

Furthermore, the OAM transfer onto particles was shown with the help of a vortex metalens, realizing both vortex beam generation and focusing by one single metasurface element. The radial stiffness per unit power was measured to  $K_r \approx 4.28 \text{ pN}\mu\text{m}^{-1}\text{W}^{-1}$ . Hence, no additional phase masks for beam shaping were required.

For practical usage in the fields of biomedical research or biophotonics it is necessary to produce metalenses with a higher numerical aperture. This can be done for example by immersion metalenses. It would be advantageous to produce the nanostructures in such a way that they are surrounded by a synthetic material that has the same refractive index as the solution in which the particles are located. In this context, it would be very interesting to also improve the metalens design in such a way that the outer k-vectors of the lens contribute more efficiently and thus also enable 3D trapping of particles. Nevertheless, the concept allows exciting possibilities in the fields of integrated nano-optoelectronics, lab-on-a-chip and microfluidic optical tweezers. It may pave the way for future devices with possible integration of electronically addressable liquid crystals. These can be utilized to switch the polarity of the metalens and to enable fully remotely controlled lab-on-chip optical tweezers.

---

## Bibliography

---

- [Afz92] ROBERT S AFZAL and E BRIAN TREACY: ‘Optical tweezers using a diode laser’. *Review of scientific instruments* (1992), vol. 63(4): pp. 2157–2163 (cit. on p. 91).
- [Aie12] FRANCESCO AIETA, PATRICE GENEVET, MIKHAIL A KATS, NANFANG YU, ROMAIN BLANCHARD, ZENO GABURRO, and FEDERICO CAPASSO: ‘Aberration-free ultrathin flat lenses and axicons at telecom wavelengths based on plasmonic metasurfaces’. *Nano letters* (2012), vol. 12(9): pp. 4932–4936 (cit. on p. 2).
- [All92] LES ALLEN, MARCO W BEIJERSBERGEN, RJC SPREEUW, and JP WOERDMAN: ‘Orbital angular momentum of light and the transformation of Laguerre-Gaussian laser modes’. *Physical review A* (1992), vol. 45(11): p. 8185 (cit. on p. 59).
- [Alm16a] EUCLIDES ALMEIDA, ORA BITTON, and YEHIAM PRIOR: ‘Nonlinear metamaterials for holography’. *Nature communications* (2016), vol. 7: p. 12533 (cit. on pp. 3, 42, 63, 68).
- [Alm16b] EUCLIDES ALMEIDA, GUY SHALEM, and YEHIAM PRIOR: ‘Subwavelength nonlinear phase control and anomalous phase matching in plasmonic metasurfaces’. *Nature communications* (2016), vol. 7: p. 10367 (cit. on pp. 3, 30, 42).
- [Ara92] PK ARAVIND: ‘A simple proof of Pancharatnam’s theorem’. *Optics communications* (1992), vol. 94(4): pp. 191–196 (cit. on p. 24).
- [Arb15] AMIR ARBABI, YU HORIE, MAHMOOD BAGHERI, and ANDREI FARAON: ‘Dielectric metasurfaces for complete control of phase and polarization with subwavelength spatial resolution and high transmission’. *Nature nanotechnology* (2015), vol. (cit. on p. 41).
- [Arb16] EHSAN ARBABI, AMIR ARBABI, SEYEDEH MAHSA KAMALI, YU HORIE, and ANDREI FARAON: ‘Multiwavelength polarization-insensitive lenses based on dielectric metasurfaces with meta-molecules’. *Optica* (2016), vol. 3(6): pp. 628–633 (cit. on p. 42).
- [Ash70] ARTHUR ASHKIN: ‘Acceleration and trapping of particles by radiation pressure’. *Physical Review Letters* (1970), vol. 24(4): p. 156 (cit. on p. 90).

- [Bar19] JONATHAN BAR-DAVID and URIEL LEVY: ‘Nonlinear diffraction in asymmetric dielectric metasurfaces’. *Nano letters* (2019), vol. 19(2): pp. 1044–1051 (cit. on p. [36](#)).
- [Bar13] CHRISTOPHER BARSİ and JASON W FLEISCHER: ‘Nonlinear abbe theory’. *Nature Photonics* (2013), vol. 7(8): pp. 639–643 (cit. on p. [30](#)).
- [Ber87] MICHAEL V BERRY: ‘The adiabatic phase and Pancharatnam’s phase for polarized light’. *Journal of Modern Optics* (1987), vol. 34(11): pp. 1401–1407 (cit. on p. [42](#)).
- [Bha72] S BHAGAVANTAM and P CHANDRASEKHAR: ‘Harmonic generation and selection rules in nonlinear optics’. *Proceedings of the Indian Academy of Sciences-Section A*. Vol. 76. 1. Springer. 1972: pp. 13–20 (cit. on p. [37](#)).
- [Bia12] PAOLO BIAGIONI, JER-SHING HUANG, and BERT HECHT: ‘Nanoantennas for visible and infrared radiation’. *Reports on Progress in Physics* (2012), vol. 75(2): p. 024402 (cit. on p. [16](#)).
- [Bie02] GABRIEL BIENER, AVI NIV, VLADIMIR KLEINER, and EREZ HASMAN: ‘Formation of helical beams by use of Pancharatnam–Berry phase optical elements’. *Optics letters* (2002), vol. 27(21): pp. 1875–1877 (cit. on p. [23](#)).
- [Bla11] ROMAIN BLANCHARD, SVETLANA V BORISKINA, PATRICE GENEVET, MIKHAIL A KATS, JEAN-PHILIPPE TETIENNE, NANFANG YU, MALLAN O SCULLY, LUCA DAL NEGRO, and FEDERICO CAPASSO: ‘Multi-wavelength mid-infrared plasmonic antennas with single nanoscale focal point’. *optics express* (2011), vol. 19(22): pp. 22113–22124 (cit. on p. [45](#)).
- [Blo12] NOA VOLOCH BLOCH, KEREN SHEMER, ASIA SHAPIRA, ROY SHILOH, IRIT JUWILER, and ADY ARIE: ‘Twisting light by nonlinear photonic crystals’. *Physical review letters* (2012), vol. 108(23): p. 233902 (cit. on p. [59](#)).
- [Bom02] ZE’EV BOMZON, GABRIEL BIENER, VLADIMIR KLEINER, and EREZ HASMAN: ‘Space-variant Pancharatnam–Berry phase optical elements with computer-generated subwavelength gratings’. *Optics Letters* (2002), vol. 27(13): pp. 1141–1143 (cit. on pp. [42](#), [92](#)).
- [Bor13] MAX BORN and EMIL WOLF: *Principles of optics: electromagnetic theory of propagation, interference and diffraction of light*. Elsevier, 2013 (cit. on p. [8](#)).
- [Boy20] ROBERT W BOYD: *Nonlinear optics*. Academic press, 2020 (cit. on pp. [33](#), [35](#), [36](#)).

- 
- [Cam16] ROCIO CAMACHO-MORALES, MOHSEN RAHMANI, SERGEY KRUK, LEI WANG, LEI XU, DARIA A SMIRNOVA, ALEXANDER S SOLNTSEV, ANDREY MIROSHNICHENKO, HARK HOE TAN, and FOUAD KAROUTA: ‘Nonlinear generation of vector beams from AlGaAs nanoantennas’. *Nano letters* (2016), vol. 16(11): pp. 7191–7197 (cit. on p. 42).
- [Car19] JOSÉ VICENTE CARRIÓN, JORGE ALBERO, MACIEJ BARANSKI, CHRISTOPHE GORECKI, and NICOLAS PASSILLY: ‘Microfabrication of axicons by glass blowing at a wafer-level’. *Optics letters* (2019), vol. 44(13): pp. 3282–3285 (cit. on p. 11).
- [Cha06] YI-REN CHANG, LONG HSU, and SIEN CHI: ‘Optical trapping of a spherically symmetric sphere in the ray-optics regime: a model for optical tweezers upon cells’. *Applied optics* (2006), vol. 45(16): pp. 3885–3892 (cit. on p. 91).
- [Cha20] TEANCHAI CHANTAKIT\*, CHRISTIAN SCHLICKRIEDE\*, BASUDEB SAIN, FABIAN MEYER, THOMAS WEISS, NATTAPORN CHATTHAM, and THOMAS ZENTGRAF: ‘All-dielectric silicon metalens for two-dimensional particle manipulation in optical tweezers’. *Photonics Research* (2020), vol. 8(9): pp. 1435–1440 (cit. on pp. 89, 100, 102).
- [Che16] HOU-TONG CHEN, ANTOINETTE J TAYLOR, and NANFANG YU: ‘A review of metasurfaces: physics and applications’. *Reports on progress in physics* (2016), vol. 79(7): p. 076401 (cit. on p. 2).
- [Che10] PAI-YEN CHEN and ANDREA ALÙ: ‘Optical nanoantenna arrays loaded with nonlinear materials’. *Physical Review B* (2010), vol. 82(23): p. 235405 (cit. on p. 63).
- [Che14a] SHUMEI CHEN, GUIXIN LI, FRANZISKA ZEUNER, WING HAN WONG, EDWIN YUE BUN PUN, THOMAS ZENTGRAF, KOK WAI CHEAH, and SHUANG ZHANG: ‘Symmetry-selective third-harmonic generation from plasmonic metacrystals’. *Physical Review Letters* (2014), vol. 113(3): p. 033901 (cit. on p. 37).
- [Che18a] SHUMEI CHEN, MOHSEN RAHMANI, KING FAI LI, ANDREY MIROSHNICHENKO, THOMAS ZENTGRAF, GUIXIN LI, DRAGOMIR NESHEV, and SHUANG ZHANG: ‘Third harmonic generation enhanced by multipolar interference in complementary silicon metasurfaces’. *ACS Photonics* (2018), vol. 5(5): pp. 1671–1675 (cit. on p. 64).
- [Che20] WEI TING CHEN, ALEXANDER Y ZHU, and FEDERICO CAPASSO: ‘Flat optics with dispersion-engineered metasurfaces’. *Nature Reviews Materials* (2020), vol. 5(8): pp. 604–620 (cit. on pp. 11, 15, 25, 26).

- [Che18b] WEI TING CHEN, ALEXANDER Y ZHU, VYSHAKH SANJEEV, MOHAMMADREZA KHORASANINEJAD, ZHUJUN SHI, ERIC LEE, and FEDERICO CAPASSO: ‘A broadband achromatic metalens for focusing and imaging in the visible’. *Nature nanotechnology* (2018), vol. 13(3): pp. 220–226 (cit. on p. 2).
- [Che15] XIANZHONG CHEN, MING CHEN, MUHAMMAD QASIM MEHMOOD, DANDAN WEN, FUYONG YUE, CHENG–WEI QIU, and SHUANG ZHANG: ‘Longitudinal multifoci metalens for circularly polarized light’. *Advanced Optical Materials* (2015), vol. 3(9): pp. 1201–1206 (cit. on pp. 42, 91, 92).
- [Che13] XIANZHONG CHEN, LINGLING HUANG, HOLGER MÜHLENBERND, GUIXIN LI, BENFENG BAI, QIAOFENG TAN, GUOFAN JIN, CHENG–WEI QIU, THOMAS ZENTGRAF, and SHUANG ZHANG: ‘Reversible Three–Dimensional Focusing of Visible Light with Ultrathin Plasmonic Flat Lens’. *Advanced Optical Materials* (2013), vol. 1(7): pp. 517–521 (cit. on p. 42).
- [Che12] XIANZHONG CHEN, LINGLING HUANG, HOLGER MÜHLENBERND, GUIXIN LI, BENFENG BAI, QIAOFENG TAN, GUOFAN JIN, CHENG–WEI QIU, SHUANG ZHANG, and THOMAS ZENTGRAF: ‘Dual–polarity plasmonic metalens for visible light’. *Nature Communications* (2012), vol. 3: p. 1198 (cit. on pp. 27, 41, 42, 78, 91, 92).
- [Che14b] XIANZHONG CHEN, YAN ZHANG, LINGLING HUANG, and SHUANG ZHANG: ‘Ultrathin metasurface laser beam shaper’. *Advanced Optical Materials* (2014), vol. 2(10): pp. 978–982 (cit. on p. 42).
- [Chi05] PEI YU CHIOU, AARON T OHTA, and MING C WU: ‘Massively parallel manipulation of single cells and microparticles using optical images’. *Nature* (2005), vol. 436(7049): p. 370 (cit. on p. 90).
- [Coh19] ELIAHU COHEN, HUGO LAROCQUE, FRÉDÉRIC BOUCHARD, FARSHAD NEJADSATTARI, YUVAL GEFEN, and EBRAHIM KARIMI: ‘Geometric phase from Aharonov–Bohm to Pancharatnam–Berry and beyond’. *Nature Reviews Physics* (2019), vol. 1(7): pp. 437–449 (cit. on pp. 19, 24, 40).
- [Col84] EDWARD COLLETT: ‘Measurement of the four Stokes polarization parameters with a single circular polarizer’. *Optics communications* (1984), vol. 52(2): pp. 77–80 (cit. on p. 131).
- [Dec15] MANUEL DECKER, ISABELLE STAUDE, MATTHIAS FALKNER, JASON DOMINGUEZ, DRAGOMIR N NESHEV, IGAL BRENER, THOMAS PERTSCH, and YURI S KIVSHAR: ‘High-efficiency dielectric Huygens’ surfaces’. *Advanced Optical Materials* (2015), vol. 3(6): pp. 813–820 (cit. on p. 64).

- 
- [Der16] STANISLAV A DEREVYANKO, JAROSLAW E PRILEPSKY, and SERGEI K TURITSYN: ‘Capacity estimates for optical transmission based on the nonlinear Fourier transform’. *Nature Communications* (2016), vol. 7: p. 12710 (cit. on p. 56).
- [Dho11] K DHOLAKIA and T ČIŽMÁR: ‘Shaping the future of manipulation’. *Nature Photonics* (2011), vol. 5(6): p. 335 (cit. on p. 90).
- [Din15] XUMIN DING, FRANCESCO MONTICONE, KUANG ZHANG, LEI ZHANG, DONGLIANG GAO, SHAH NAWAZ BUROKUR, ANDRE de LUSTRAC, QUN WU, CHENG-WEI QIU, and ANDREA ALÙ: ‘Ultrathin Pancharatnam–Berry metasurface with maximal cross-polarization efficiency’. *Advanced Materials* (2015), vol. 27(7): pp. 1195–1200 (cit. on pp. 19, 25).
- [Dre02] MARTIN DRESSEL and GEORGE GRÜNER: *Electrodynamics of solids: optical properties of electrons in matter*. American Association of Physics Teachers, 2002 (cit. on p. 16).
- [Ebb98] THOMAS W EBBESEN, HENRI J LEZEC, HF GHAEMI, TINEKE THIO, and PETER A WOLFF: ‘Extraordinary optical transmission through sub-wavelength hole arrays’. *Nature* (1998), vol. 391(6668): pp. 667–669 (cit. on p. 16).
- [Eng20] JACOB ENGELBERG and URIEL LEVY: ‘The advantages of metalenses over diffractive lenses’. *Nature communications* (2020), vol. 11(1): pp. 1–4 (cit. on pp. 9, 10).
- [Erg10] TOLGA ERGIN, NICOLAS STENGER, PATRICE BRENNER, JOHN B PENDRY, and MARTIN WEGENER: ‘Three-dimensional invisibility cloak at optical wavelengths’. *Science* (2010), vol. 328(5976): pp. 337–339 (cit. on p. 41).
- [Fan05] NICHOLAS FANG, HYESOG LEE, CHENG SUN, and XIANG ZHANG: ‘Sub-diffraction-limited optical imaging with a silver superlens’. *Science* (2005), vol. 308(5721): pp. 534–537 (cit. on p. 41).
- [Fig00] DANIEL FIGEYS and DEVANAND PINTO: *Lab-on-a-chip: a revolution in biological and medical sciences*. 2000 (cit. on p. 92).
- [Gao11] CHUNQING GAO, XIAOQING QI, YIDONG LIU, JINGTAO XIN, and LEI WANG: ‘Sorting and detecting orbital angular momentum states by using a Dove prism embedded Mach–Zehnder interferometer and amplitude gratings’. *Optics Communications* (2011), vol. 284(1): pp. 48–51 (cit. on p. 59).

- [Gar02] V GARCÉS-CHAVEZ, DAVID MCGLOIN, H MELVILLE, WILSON SIBBETT, and KISHAN DHOLAKIA: ‘Simultaneous micromanipulation in multiple planes using a self-reconstructing light beam’. *Nature* (2002), vol. 419(6903): p. 145 (cit. on p. 90).
- [Gar05] FJ GARCIA-VIDAL, ESTEBAN MORENO, JA PORTO, and L MARTIN-MORENO: ‘Transmission of light through a single rectangular hole’. *Physical review letters* (2005), vol. 95(10): p. 103901 (cit. on p. 19).
- [Gef12] JEAN-MICHEL GEFFRIN, B GARCÍA-CÁMARA, R GÓMEZ-MEDINA, P ALBELLA, LS FROUFE-PÉREZ, CHRISTELLE EYRAUD, AMELIE LITMAN, RODOLPHE VAILLON, F GONZÁLEZ, M NIETO-VESPERINAS, et al.: ‘Magnetic and electric coherence in forward-and back-scattered electromagnetic waves by a single dielectric subwavelength sphere’. *Nature communications* (2012), vol. 3(1): pp. 1–8 (cit. on p. 64).
- [Gen17] PATRICE GENEVET, FEDERICO CAPASSO, FRANCESCO AIETA, MOHAMMADREZA KHORASANINEJAD, and ROBERT DEVLIN: ‘Recent advances in planar optics: from plasmonic to dielectric metasurfaces’. *Optica* (2017), vol. 4(1): pp. 139–152 (cit. on pp. 2, 16).
- [Geo19] PHILIP GEORGI, MARCELLO MASSARO, KAI-HONG LUO, BASUDEB SAIN, NICOLA MONTAUT, HARALD HERRMANN, THOMAS WEISS, GUIXIN LI, CHRISTINE SILBERHORN, and THOMAS ZENTGRAF: ‘Metasurface interferometry toward quantum sensors’. *Light: Science & Applications* (2019), vol. 8(1): pp. 1–7 (cit. on p. 93).
- [Goo05] JOSEPH W GOODMAN: *Introduction to Fourier optics*. Roberts and Company Publishers, 2005 (cit. on pp. 7, 8).
- [Gri03] DAVID G GRIER: ‘A revolution in optical manipulation’. *Nature* (2003), vol. 424(6950): p. 810 (cit. on p. 90).
- [Gri16] GUSTAVO GRINBLAT, YI LI, MICHAEL P NIELSEN, RUPERT F OULTON, and STEFAN A MAIER: ‘Enhanced third harmonic generation in single germanium nanodisks excited at the anapole mode’. *Nano letters* (2016), vol. 16(7): pp. 4635–4640 (cit. on p. 63).
- [Guo08] HONGCANG GUO, TODD P MEYRATH, THOMAS ZENTGRAF, NA LIU, LIWEI FU, HEINZ SCHWEIZER, and HARALD GIESSEN: ‘Optical resonances of bowtie slot antennas and their geometry and material dependence’. *Optics express* (2008), vol. 16(11): pp. 7756–7766 (cit. on p. 19).
- [Gut00] JULIO C GUTIÉRREZ-VEGA, MD ITURBE-CASTILLO, and S CHÁVEZ-CERDA: ‘Alternative formulation for invariant optical fields: Mathieu beams’. *Optics letters* (2000), vol. 25(20): pp. 1493–1495 (cit. on p. 58).

- 
- [Hau80] PS HAUGE, ROLF H MULLER, and CG SMITH: ‘Conventions and formulas for using the Mueller-Stokes calculus in ellipsometry’. *Surface science* (1980), vol. 96(1-3): pp. 81–107 (cit. on pp. [19](#), [21](#)).
  - [Hec02] EUGENE HECHT: *Optics*. Addison Wesley, 2002 (cit. on p. [30](#)).
  - [Hua13a] LINGLING HUANG, XIANZHONG CHEN, BENFENG BAI, QIAOFENG TAN, GUOFAN JIN, THOMAS ZENTGRAF, and SHUANG ZHANG: ‘Helicity dependent directional surface plasmon polariton excitation using a metasurface with interfacial phase discontinuity’. *Light: Science & Applications* (2013), vol. 2(3): e70 (cit. on pp. [25](#), [41](#)).
  - [Hua12] LINGLING HUANG, XIANZHONG CHEN, HOLGER MÜHLENBERND, GUIXIN LI, BENFENG BAI, QIAOFENG TAN, GUOFAN JIN, THOMAS ZENTGRAF, and SHUANG ZHANG: ‘Dispersionless phase discontinuities for controlling light propagation’. *Nano letters* (2012), vol. 12(11): pp. 5750–5755 (cit. on pp. [2](#), [42](#)).
  - [Hua13b] LINGLING HUANG, XIANZHONG CHEN, HOLGER MÜHLENBERND, HAO ZHANG, SHUMEI CHEN, BENFENG BAI, QIAOFENG TAN, GUOFAN JIN, KOK-WAI CHEAH, CHENG-WEI QIU, JENSEN LI, THOMAS ZENTGRAF, and SHUANG ZHANG: ‘Three-dimensional optical holography using a plasmonic metasurface’. *Nature communications* (2013), vol. 4(1): pp. 1–8 (cit. on pp. [2](#), [41](#), [42](#)).
  - [Joh16] PATRICK LIE JOHANSEN, FEDERICO FENAROLI, LASSE EVENSEN, GARETH GRIFFITHS, and GERBRAND KOSTER: ‘Optical micromanipulation of nanoparticles and cells inside living zebrafish’. *Nature Communications* (2016), vol. 7(1): pp. 1–8 (cit. on p. [90](#)).
  - [Joh72] PETER B JOHNSON and R-WJPRB CHRISTY: ‘Optical constants of the noble metals’. *Physical review B* (1972), vol. 6(12): p. 4370 (cit. on pp. [16](#), [17](#)).
  - [Kar14] EBRAHIM KARIMI, SEBASTIAN A SCHULZ, ISRAEL DE LEON, HAMMAM QASSIM, JEREMY UPHAM, and ROBERT W BOYD: ‘Generating optical orbital angular momentum at visible wavelengths using a plasmonic metasurface’. *Light: Science & Applications* (2014), vol. 3(5): e167–e167 (cit. on p. [19](#)).
  - [Kau12] MARTTI KAURANEN and ANATOLY V ZAYATS: ‘Nonlinear plasmonics’. *Nature Photonics* (2012), vol. 6(11): pp. 737–748 (cit. on p. [35](#)).
  - [Ke16] YOUNGANG KE, YACHAO LIU, JUNXIAO ZHOU, YUANYUAN LIU, HAILU LUO, and SHUANGCHUN WEN: ‘Optical integration of Pancharatnam–Berry phase lens and dynamical phase lens’. *Applied Physics Letters* (2016), vol. 108(10): p. 101102 (cit. on p. [42](#)).

- [Ker15] SHAY KEREN-ZUR, ORI AVAYU, LIOR MICHAELI, and TAL ELLENBOGEN: ‘Nonlinear beam shaping with plasmonic metasurfaces’. *ACS Photonics* (2015), vol. 3(1): pp. 117–123 (cit. on pp. [42](#), [58](#), [63](#)).
- [Kho15] M KHORASANINEJAD, W ZHU, and KB CROZIER: ‘Efficient polarization beam splitter pixels based on a dielectric metasurface’. *Optica* (2015), vol. 2(4): pp. 376–382 (cit. on p. [91](#)).
- [Kho17] MOHAMMADREZA KHORASANINEJAD and FEDERICO CAPASSO: ‘Metalenses: Versatile multifunctional photonic components’. *Science* (2017), vol. 358(6367) (cit. on p. [2](#)).
- [Kho16] MOHAMMADREZA KHORASANINEJAD, WEI TING CHEN, ROBERT C DEVLIN, JAEWON OH, ALEXANDER Y ZHU, and FEDERICO CAPASSO: ‘Metalenses at visible wavelengths: Diffraction-limited focusing and sub-wavelength resolution imaging’. *Science* (2016), vol. 352(6290): pp. 1190–1194 (cit. on pp. [10](#), [11](#), [25](#), [42](#), [91](#)).
- [Kho14] MOHAMMADREZA KHORASANINEJAD and KENNETH B CROZIER: ‘Silicon nanofin grating as a miniature chirality-distinguishing beam-splitter’. *Nature communications* (2014), vol. 5(1): pp. 1–6 (cit. on p. [25](#)).
- [Kon14] KUNIAKI KONISHI, TAKUYA HIGUCHI, JIA LI, JAKOB LARSSON, SHUNTARO ISHII, and MAKOTO KUWATA-GONOKAMI: ‘Polarization-controlled circular second-harmonic generation from metal hole arrays with three-fold rotational symmetry’. *Physical review letters* (2014), vol. 112(13): p. 135502 (cit. on p. [39](#)).
- [Kra11] ALEKSANDR E KRASNOK, ANDREI E MIROSHNICHENKO, PAVEL A BELOV, and YURI S KIVSHAR: ‘Huygens optical elements and Yagi-Uda nanoantennas based on dielectric nanoparticles’. *JETP letters* (2011), vol. 94(8): pp. 593–598 (cit. on p. [64](#)).
- [Kra18] ALEXANDER KRASNOK, MYKHAILO TYMCHENKO, and ANDREA ALU: ‘Nonlinear metasurfaces: a paradigm shift in nonlinear optics’. *Materials Today* (2018), vol. 21(1): pp. 8–21 (cit. on pp. [3](#), [31](#), [64](#)).
- [Kru16] SERGEY KRUK, BEN HOPKINS, IVAN I KRAVCHENKO, ANDREY MIROSHNICHENKO, DRAGOMIR N NESHEV, and YURI S KIVSHAR: ‘Invited Article: Broadband highly efficient dielectric metadevices for polarization control’. *Apl Photonics* (2016), vol. 1(3): p. 030801 (cit. on p. [64](#)).
- [Kru17] SERGEY KRUK and YURI KIVSHAR: ‘Functional meta-optics and nanophotonics governed by Mie resonances’. *ACS Photonics* (2017), vol. 4(11): pp. 2638–2649 (cit. on p. [64](#)).

- 
- [Kur13] P YU KURYOZ, LV POPERENKO, and VG KRAVETS: ‘Correlation between dielectric constants and enhancement of surface plasmon resonances for thin gold films’. *physica status solidi (a)* (2013), vol. 210(11): pp. 2445–2455 (cit. on p. 16).
- [Lar12] STÉPHANE LAROCHE, YU-JU TSAI, TALMAGE TYLER, NAN M JOKERST, and DAVID R SMITH: ‘Infrared metamaterial phase holograms’. *Nature Materials* (2012), vol. 11(5): pp. 450–454 (cit. on p. 42).
- [Lee10] BYOUNGHO LEE, IL-MIN LEE, SEYOON KIM, DONG-HO OH, and LAMBERTUS HESSELINK: ‘Review on subwavelength confinement of light with plasmonics’. *Journal of Modern Optics* (2010), vol. 57(16): pp. 1479–1497 (cit. on p. 16).
- [Lee14] JONGWON LEE, MYKHAILO TYMCHENKO, CHRISTOS ARGYROPOULOS, PAI-YEN CHEN, FENG LU, FREDERIC DEMMERLE, GERHARD BOEHM, MARKUS-CHRISTIAN AMANN, ANDREA ALU, and MIKHAIL A BELKIN: ‘Giant nonlinear response from plasmonic metasurfaces coupled to inter-subband transitions’. *Nature* (2014), vol. 511(7507): p. 65 (cit. on pp. 42, 47, 63).
- [Li15] GUIXIN LI, SHUMEI CHEN, NITIPAT PHOLCHAI, BERNHARD REINEKE, POLIS WING HAN WONG, EDWIN YUE BUN PUN, KOK WAI CHEAH, THOMAS ZENTGRAF, and SHUANG ZHANG: ‘Continuous control of the nonlinearity phase for harmonic generations’. *Nature materials* (2015), vol. 14(6): p. 607 (cit. on pp. 37, 39, 42, 47, 63).
- [Li17a] GUIXIN LI, LIN WU, KING F LI, SHUMEI CHEN, CHRISTIAN SCHLICK-RIEDE, ZHENGJI XU, SIYA HUANG, WENDI LI, YANJUN LIU, EDWIN YB PUN, THOMAS ZENTGRAF, KOK W. CHEAH, YU LUO, and SHUANG ZHANG: ‘Nonlinear metasurface for simultaneous control of spin and orbital angular momentum in second harmonic generation’. *Nano letters* (2017), vol. 17(12): pp. 7974–7979 (cit. on pp. 58, 61, 63).
- [Li17b] GUIXIN LI, SHUANG ZHANG, and THOMAS ZENTGRAF: ‘Nonlinear photonic metasurfaces’. *Nature Reviews Materials* (2017), vol. 2(5): p. 17010 (cit. on pp. 3, 31, 38, 47).
- [Li19] XIAO LI, JUN CHEN, ZHIFANG LIN, and JACK NG: ‘Optical pulling at macroscopic distances’. *Science Advances* (2019), vol. 5(3): eaau7814 (cit. on p. 90).
- [Li20] ZHI LI, WENWEI LIU, GUANGZHOU GENG, ZHANCHENG LI, JUNJIE LI, HUA CHENG, SHUQI CHEN, and JIANGUO TIAN: ‘Multiplexed Nondiffracting Nonlinear Metasurfaces’. *Advanced Functional Materials* (2020), vol.: p. 1910744 (cit. on p. 58).

- [Lia18] HAOWEN LIANG, QIAOLING LIN, XIANGSHENG XIE, QIAN SUN, YIN WANG, LIDAN ZHOU, LIN LIU, XIANGYANG YU, JIANYING ZHOU, THOMAS F KRAUSS, et al.: ‘Ultrahigh numerical aperture metalens at visible wavelengths’. *Nano letters* (2018), vol. 18(7): pp. 4460–4466 (cit. on p. 68).
- [Lin14] DIANMIN LIN, PENGYU FAN, EREZ HASMAN, and MARK L BRONGERSMA: ‘Dielectric gradient metasurface optical elements’. *science* (2014), vol. 345(6194): pp. 298–302 (cit. on pp. 19, 25).
- [Liu19] BO LIU, KERUI SONG, and JIANGNAN XIAO: ‘Two-dimensional optical metasurfaces: From plasmons to dielectrics’. *Advances in Condensed Matter Physics* (2019), vol. 2019 (cit. on p. 2).
- [Liu14] LIXIANG LIU, XUEQIAN ZHANG, MITCHELL KENNEY, XIAOQIANG SU, NINGNING XU, CHUNMEI OUYANG, YUNLONG SHI, JIAGUANG HAN, WEILI ZHANG, and SHUANG ZHANG: ‘Broadband metasurfaces with simultaneous control of phase and amplitude’. *Advanced Materials* (2014), vol. 26(29): pp. 5031–5036 (cit. on p. 41).
- [Liu16] SHENG LIU, MICHAEL B SINCLAIR, SINA SARAVI, GORDON A KEELER, YUANMU YANG, JOHN RENO, GREGORY M PEAKE, FRANK SETZPFANDT, ISABELLE STAUDE, and THOMAS PERTSCH: ‘Resonantly enhanced second-harmonic generation using III–V semiconductor all-dielectric metasurfaces’. *Nano letters* (2016), vol. 16(9): pp. 5426–5432 (cit. on p. 42).
- [Liu18] SHENG LIU, POLINA P VABISHCHEVICH, ALEKSANDR VASKIN, JOHN L RENO, GORDON A KEELER, MICHAEL B SINCLAIR, ISABELLE STAUDE, and IGAL BRENER: ‘An all-dielectric metasurface as a broadband optical frequency mixer’. *Nature communications* (2018), vol. 9(1): pp. 1–6 (cit. on p. 37).
- [Ma17] YANBAO MA, GUANGHAO RUI, BING GU, and YIPING CUI: ‘Trapping and manipulation of nanoparticles using multifocal optical vortex metalens’. *Scientific Reports* (2017), vol. 7(1): p. 14611 (cit. on pp. 92, 96).
- [Mac03] MICHAEL P MACDONALD, GABRIEL C SPALDING, and KISHAN DHO-LAKIA: ‘Microfluidic sorting in an optical lattice’. *Nature* (2003), vol. 426(6965): p. 421 (cit. on p. 90).
- [Mag18] HERNANDO MAGALLANES and ETIENNE BRASSELET: ‘Macroscopic direct observation of optical spin-dependent lateral forces and left-handed torques’. *Nature Photonics* (2018), vol. 12(8): pp. 461–464 (cit. on p. 90).

- 
- [Mai07] STEFAN ALEXANDER MAIER: *Plasmonics: fundamentals and applications*. Springer Science & Business Media, 2007 (cit. on pp. 16, 17).
  - [Mal02] NUNZIA MALAGNINO, GIUSEPPE PESCE, ANTONIO SASSO, and ENNIO ARIMONDO: ‘Measurements of trapping efficiency and stiffness in optical tweezers’. *Optics Communications* (2002), vol. 214(1-6): pp. 15–24 (cit. on p. 100).
  - [Mao20] NINGBIN MAO, JUNHONG DENG, XUECAI ZHANG, YUTAO TANG, MINGKE JIN, YANG LI, XUAN LIU, KINGFAI LI, TUN CAO, KOKWAI CHEAH, HONG WANG, JACK NG, and GUIXIN LI: ‘Nonlinear Diatomic Metasurface for Real and Fourier Space Image Encoding’. *Nano Letters* (2020), vol. 20(10): pp. 7463–7468 (cit. on p. 57).
  - [Mar18] HEN MARKOVICH, IVAN I SHISHKIN, NETTA HENDLER, and PAVEL GINZBURG: ‘Optical manipulation along an optical axis with a polarization sensitive meta-lens’. *Nano Letters* (2018), vol. 18(8): pp. 5024–5029 (cit. on pp. 91, 100).
  - [Mar06] LORENZO MARRUCCI, C MANZO, and D PAPARO: ‘Optical spin-to-orbital angular momentum conversion in inhomogeneous anisotropic media’. *Physical Review Letters* (2006), vol. 96(16): p. 163905 (cit. on p. 42).
  - [McL68] JOHN A McLAUGHLIN and JOSEF RAVIV: ‘Nth-order autocorrelations in pattern recognition’. *Information and Control* (1968), vol. 12(2): pp. 121–142 (cit. on p. 87).
  - [Meh17] SOHEIL MEHRABKHANI and THOMAS SCHNEIDER: ‘Is the Rayleigh-Sommerfeld diffraction always an exact reference for high speed diffraction algorithms?’ *Optics express* (2017), vol. 25(24): pp. 30229–30240 (cit. on p. 75).
  - [Min18] ALEXANDER E MINOVICH and ANATOLY V ZAYATS: ‘Geometric-phase metasurfaces based on anisotropic reflection: generalized design rules’. *ACS Photonics* (2018), vol. 5(5): pp. 1755–1761 (cit. on pp. 25, 132).
  - [Mue17] JP BALTHASAR MUELLER, NOAH A RUBIN, ROBERT C DEVLIN, BENEDIKT GROEVER, and FEDERICO CAPASSO: ‘Metasurface polarization optics: independent phase control of arbitrary orthogonal states of polarization’. *Physical Review Letters* (2017), vol. 118(11): p. 113901 (cit. on p. 19).
  - [Ni12] XINGJIE NI, NARESH K EMANI, ALEXANDER V KILDISHEV, ALEXANDRA BOLTASSEVA, and VLADIMIR M SHALAEV: ‘Broadband light bending with plasmonic nanoantennas’. *Science* (2012), vol. 335(6067): pp. 427–427 (cit. on pp. 3, 41).

- [Ni13a] XINGJIE NI, SATOSHI ISHII, ALEXANDER V KILDISHEV, and VLADIMIR M SHALAEV: ‘Ultra-thin, planar, Babinet-inverted plasmonic metalenses’. *Light: Science & Applications* (2013), vol. 2(4): e72 (cit. on pp. [42](#), [91](#)).
- [Ni13b] XINGJIE NI, ALEXANDER V KILDISHEV, and VLADIMIR M SHALAEV: ‘Metasurface holograms for visible light’. *Nature Communications* (2013), vol. 4 (cit. on p. [42](#)).
- [Nie07] TIMO A NIEMINEN, VINCENT LY LOKE, ALEXANDER B STILGOE, GREGOR KNÖNER, AGATA M BRAŃCZYK, NORMAN R HECKENBERG, and HALINA RUBINSZTEIN-DUNLOP: ‘Optical tweezers computational toolbox’. *Journal of Optics A* (2007), vol. 9(8): S196 (cit. on p. [100](#)).
- [Noo16] NISHANT NOOKALA, JONGWON LEE, MYKHAILO TYMCHENKO, J SEBASTIAN GOMEZ-DIAZ, FREDERIC DEMMERLE, GERHARD BOEHM, KUEIFU LAI, GENNADY SHVETS, MARKUS-CHRISTIAN AMANN, ANDREA ALU, and MIKHAIL BELKIN: ‘Ultrathin gradient nonlinear metasurface with a giant nonlinear response’. *Optica* (2016), vol. 3(3): pp. 283–288 (cit. on p. [63](#)).
- [Nov12] LUKAS NOVOTNY and BERT HECHT: *Principles of nano-optics*. Cambridge university press, 2012 (cit. on pp. [16](#), [19](#)).
- [Nye74] JOHN FREDERICK NYE and MICHAEL VICTOR BERRY: ‘Dislocations in wave trains’. *Proceedings of the Royal Society of London. A. Mathematical and Physical Sciences* (1974), vol. 336(1605): pp. 165–190 (cit. on p. [58](#)).
- [Olm12] ROBERT L OLMON, BRIAN SLOVICK, TIMOTHY W JOHNSON, DAVID SHELTON, SANG-HYUN OH, GLENN D BOREMAN, and MARKUS B RASCHKE: ‘Optical dielectric function of gold’. *Physical Review B* (2012), vol. 86(23): p. 235147 (cit. on p. [17](#)).
- [Ost10] NATAN OSTERMAN: ‘TweezPal—optical tweezers analysis and calibration software’. *Computer Physics Communications* (2010), vol. 181(11): pp. 1911–1916 (cit. on p. [100](#)).
- [Pad11] MILES PADGETT and RICHARD BOWMAN: ‘Tweezers with a twist’. *Nature Photonics* (2011), vol. 5(6): p. 343 (cit. on p. [90](#)).
- [Pan56] SHIVARAMAKRISHNAN PANCHARATNAM: ‘Generalized theory of interference and its applications’. *Proceedings of the Indian Academy of Sciences—Section A*. Vol. 44. 6. Springer. 1956: pp. 398–417 (cit. on pp. [19](#), [23](#), [26](#), [42](#)).

- 
- [Pan18] RAMON PANIAGUA-DOMINGUEZ, YE FENG YU, EGOR KHAIDAROV, SUMIN CHOI, VICTOR LEONG, REUBEN M BAKKER, XINAN LIANG, YUAN HSING FU, VYTAUTAS VALUCKAS, LEONID A KRIVITSKY, and ARSENIY I KUZNETSOV: ‘A metalens with a near-unity numerical aperture’. *Nano letters* (2018), vol. 18(3): pp. 2124–2132 (cit. on p. 14).
- [Pra17] PRANEET PRAKASH and MANOJ VARMA: ‘Trapping/Pinning of colloidal microspheres over glass substrate using surface features’. *Scientific Reports* (2017), vol. 7(1): pp. 1–10 (cit. on p. 99).
- [Qin16] FEI QIN, LU DING, LEI ZHANG, FRANCESCO MONTICONE, CHAN CHOY CHUM, JIE DENG, SHENGTAO MEI, YING LI, JINGHUA TENG, MINGHUI HONG, SHUANG ZHANG, ANDREA ALU, and QIU CHENG-WEI: ‘Hybrid bilayer plasmonic metasurface efficiently manipulates visible light’. *Science Advances* (2016), vol. 2(1): e1501168 (cit. on p. 95).
- [Rei19] BERNHARD REINEKE, BASUDEB SAIN, RUIZHE ZHAO, LUCA CARLETTI, BINGYI LIU, LINGLING HUANG, COSTANTINO DE ANGELIS, and THOMAS ZENTGRAF: ‘Silicon metasurfaces for third harmonic geometric phase manipulation and multiplexed holography’. *Nano letters* (2019), vol. 19(9): pp. 6585–6591 (cit. on pp. 63, 94).
- [Ric10] DAVID J RICHARDSON: ‘Filling the light pipe’. *Science* (2010), vol. 330(6002): pp. 327–328 (cit. on p. 56).
- [Sai19] BASUDEB SAIN, CEDRIK MEIER, and THOMAS ZENTGRAF: ‘Nonlinear optics in all-dielectric nanoantennas and metasurfaces: a review’. *Advanced Photonics* (2019), vol. 1(2): p. 024002 (cit. on pp. 31, 38).
- [Sal19] BAHAA EA SALEH and MALVIN CARL TEICH: *Fundamentals of photonics*. John Wiley & Sons, 2019 (cit. on pp. 11, 19, 24).
- [Sau15] JURGEN SAUTTER, ISABELLE STAUDE, MANUEL DECKER, EVGENIA RUSAK, DRAGOMIR N NESHEV, IGAL BRENER, and YURI S KIVSHAR: ‘Active tuning of all-dielectric metasurfaces’. *ACS Nano* (2015), vol. 9(4): pp. 4308–4315 (cit. on p. 91).
- [Sch07] BETH SCHAEFER, EDWARD COLLETT, ROBERT SMYTH, DANIEL BARRETT, and BETH FRAHER: ‘Measuring the Stokes polarization parameters’. *American Journal of Physics* (2007), vol. 75(2): pp. 163–168 (cit. on pp. 21–23).
- [Sch20] CHRISTIAN SCHLICKRIEDE, SERGEY S KRUK, LEI WANG, BASUDEB SAIN, YURI KIVSHAR, and THOMAS ZENTGRAF: ‘Nonlinear imaging with all-dielectric metasurfaces’. *Nano Letters* (2020), vol. 20(6): pp. 4370–4376 (cit. on pp. 3, 63).

- [Sch18] CHRISTIAN SCHLICKRIEDE, NAOMI WATERMAN, BERNHARD REINEKE, PHILIP GEORGI, GUIXIN LI, SHUANG ZHANG, and THOMAS ZENTGRAF: ‘Imaging through nonlinear metalens using second harmonic generation’. *Advanced Materials* (2018), vol. 30(8): p. 1703843 (cit. on pp. 33, 63, 67).
- [Seg15] NADAV SEGAL, SHAY KEREN–ZUR, NETTA HENDLER, and TAL ELLENBOGEN: ‘Controlling light with metamaterial–based nonlinear photonic crystals’. *Nature Photonics* (2015), vol. 9(3): pp. 180–184 (cit. on p. 42).
- [Shc14] MAXIM R SHCHERBAKOV, DRAGOMIR N NESHEV, BEN HOPKINS, ALEXANDER S SHOROKHOV, ISABELLE STAUDE, ELIZAVETA V MELIK-GAYKAZYAN, MANUEL DECKER, ALEXANDER A EZHOV, ANDREY E MIROSHNICHENKO, IGAL BRENER, ANDREY A FEDYANIN, and YURI S KIVSHAR: ‘Enhanced third-harmonic generation in silicon nanoparticles driven by magnetic response’. *Nano letters* (2014), vol. 14(11): pp. 6488–6492 (cit. on p. 63).
- [Shc15] MAXIM R SHCHERBAKOV, POLINA P VABISHCHEVICH, ALEXANDER S SHOROKHOV, KATIE E CHONG, DUK–YONG CHOI, ISABELLE STAUDE, ANDREY E MIROSHNICHENKO, DRAGOMIR N NESHEV, ANDREY A FEDYANIN, and YURI S KIVSHAR: ‘Ultrafast all–optical switching with magnetic resonances in nonlinear dielectric nanostructures’. *Nano letters* (2015), vol. 15(10): pp. 6985–6990 (cit. on p. 42).
- [She18] ALAN SHE, SHUYAN ZHANG, SAMUEL SHIAN, DAVID R CLARKE, and FEDERICO CAPASSO: ‘Large area metalenses: design, characterization, and mass manufacturing’. *Optics express* (2018), vol. 26(2): pp. 1573–1585 (cit. on p. 2).
- [She84] YUEN-RON SHEN: *The principles of nonlinear optics*. John Wiley and Sons, 1984 (cit. on p. 37).
- [Sie98] ANTHONY E SIEGMAN: ‘How to (maybe) measure laser beam quality’. *Diode Pumped Solid State Lasers: Applications and Issues*. Optical Society of America. 1998: MQ1 (cit. on p. 68).
- [Sim14] BORIS SIMKHOVICH and GUY BARTAL: ‘Plasmon–enhanced four–wave mixing for superresolution applications’. *Physical review letters* (2014), vol. 112(5): p. 056802 (cit. on p. 42).
- [Smi16] DARIA SMIRNOVA and YURI S KIVSHAR: ‘Multipolar nonlinear nanophotonics’. *Optica* (2016), vol. 3(11): pp. 1241–1255 (cit. on p. 63).
- [Smi04] DAVID R SMITH, JOHN B PENDRY, and MIKE CK WILTSHIRE: ‘Metamaterials and negative refractive index’. *Science* (2004), vol. 305(5685): pp. 788–792 (cit. on p. 2).

- 
- [Sos98] MS SOSKIN and MV VASNETSOV: ‘Nonlinear singular optics’. *Pure and Applied Optics: Journal of the European Optical Society Part A* (1998), vol. 7(2): p. 301 (cit. on p. 58).
  - [Sur05] SUBRA SURESH, J SPATZ, JP MILLS, ALEXANDRE MICOULET, M DAO, CT LIM, M BEIL, and T SEUFFERLEIN: ‘Connections between single-cell biomechanics and human disease states: gastrointestinal cancer and malaria’. *Acta Biomaterialia* (2005), vol. 1(1): pp. 15–30 (cit. on p. 90).
  - [Suw19] SATAYU SUWANNASOPON, FABIAN MEYER, CHRISTIAN SCHLICKRIEDE, PAPICHAYA CHAISAKUL, JUMRAS LIMTRAKUL, THOMAS ZENTGRAF, and NATTAPORN CHATTHAM: ‘Miniaturized Metalens Based Optical Tweezers on Liquid Crystal Droplets for Lab-on-a-Chip Optical Motors’. *Crystals* (2019), vol. 9(10): p. 515 (cit. on p. 91).
  - [Thi07] MICHAEL THIEL, MANUEL DECKER, MARKUS DEUBEL, MARTIN WEGENER, STEFAN LINDEN, and GEORG von FREYMAN: ‘Polarization Stop Bands in Chiral Polymeric Three-Dimensional Photonic Crystals’. *Advanced Materials* (2007), vol. 19(2): pp. 207–210 (cit. on p. 10).
  - [Tka18] GEORGIY TKACHENKO, DAAN STELLINGA, ANDREI RUSKUC, MINGZHOU CHEN, KISHAN DHOLAKIA, and THOMAS F KRAUSS: ‘Optical trapping with planar silicon metalenses’. *Optics Letters* (2018), vol. 43(14): pp. 3224–3227 (cit. on p. 91).
  - [Tym15] MYKHAILO TYMCHENKO, J SEBASTIAN GOMEZ-DIAZ, JONGWON LEE, NISHANT NOOKALA, MIKHAIL A BELKIN, and ANDREA ALÙ: ‘Gradient nonlinear pancharatnam-berry metasurfaces’. *Physical review letters* (2015), vol. 115(20): p. 207403 (cit. on p. 63).
  - [Van81] J VAN ROEY, J VAN DER DONK, and PE LAGASSE: ‘Beam-propagation method: analysis and assessment’. *Josa* (1981), vol. 71(7): pp. 803–810 (cit. on p. 70).
  - [Wal17] FELICITAS WALTER, GUIXIN LI, CEDRIK MEIER, SHUANG ZHANG, and THOMAS ZENTGRAF: ‘Ultrathin nonlinear metasurface for optical image encoding’. *Nano letters* (2017), vol. 17(5): pp. 3171–3175 (cit. on pp. 57, 63).
  - [Wan17] CHENG WANG, ZHAOYI LI, MYOUNG-HWAN KIM, XIAO XIONG, XI-FENG REN, GUANG-CAN GUO, NANFANG YU, and MARKO LONČAR: ‘Metasurface-assisted phase-matching-free second harmonic generation in lithium niobate waveguides’. *Nature communications* (2017), vol. 8(1): p. 2098 (cit. on p. 31).

- [Wan16] JIAN WANG and JING DU: ‘Plasmonic and dielectric metasurfaces: design, fabrication and applications’. *Applied Sciences* (2016), vol. 6(9): p. 239 (cit. on p. 16).
- [Wan18] LEI WANG, SERGEY KRUK, KIRILL KOSHELEV, IVAN KRAVCHENKO, BARRY LUTHER-DAVIES, and YURI KIVSHAR: ‘Nonlinear wavefront control with all-dielectric metasurfaces’. *Nano letters* (2018), vol. 18(6): pp. 3978–3984 (cit. on pp. 64, 65).
- [Wei11] THOMAS WEISS: ‘Advanced numerical and semi-analytical scattering matrix calculations for modern nano-optics’. 2011 (cit. on p. 93).
- [Wen16a] DANDAN WEN, SHUMEI CHEN, FUYONG YUE, KINLONG CHAN, MING CHEN, MARCUS ARDRON, KING FAI LI, POLIS WING HAN WONG, KOK WAI CHEAH, and EDWIN YUE BUN PUN: ‘Metasurface Device with Helicity-Dependent Functionality’. *Advanced Optical Materials* (2016), vol. 4(2): pp. 321–327 (cit. on p. 42).
- [Wen16b] DANDAN WEN, FUYONG YUE, MARCUS ARDRON, and XIANZHONG CHEN: ‘Multifunctional metasurface lens for imaging and Fourier transform’. *Scientific Reports* (2016), vol. 6: p. 27628 (cit. on p. 42).
- [Whe09] WILLIAM WHEWELL: ‘Singular optics: more ado about nothing’. *J. Opt. A: Pure Appl. Opt* (2009), vol. 11(090201): p. 090201 (cit. on p. 58).
- [Xu18] ZHE XU, WUZHOU SONG, and KENNETH B CROZIER: ‘Optical trapping of nanoparticles using all-silicon nanoantennas’. *ACS Photonics* (2018), vol. 5(12): pp. 4993–5001 (cit. on p. 91).
- [Yan15] YUANMU YANG, WENYI WANG, ABDELAZIZ BOULESBAA, IVAN I KRAVCHENKO, DAYRL P BRIGGS, ALEXANDER PURETZKY, DAVID GEOHEGAN, and JASON VALENTINE: ‘Nonlinear Fano-resonant dielectric metasurfaces’. *Nano letters* (2015), vol. 15(11): pp. 7388–7393 (cit. on pp. 42, 63).
- [Yao11] ALISON M YAO and MILES J PADGETT: ‘Orbital angular momentum: origins, behavior and applications’. *Advances in Optics and Photonics* (2011), vol. 3(2): pp. 161–204 (cit. on p. 60).
- [Ye16] WEIMIN YE, FRANZISKA ZEUNER, XIN LI, BERNHARD REINEKE, SHAN HE, CHENG-WEI QIU, JUAN LIU, YONGTIAN WANG, SHUANG ZHANG, and THOMAS ZENTGRAF: ‘Spin and wavelength multiplexed nonlinear metasurface holography’. *Nature communications* (2016), vol. 7: p. 11930 (cit. on pp. 42, 63).

- 
- [Yin17] XINGHUI YIN, TOBIAS STEINLE, LINGLING HUANG, THOMAS TAUBNER, MATTHIAS WUTTIG, THOMAS ZENTGRAF, and HARALD GIESSEN: ‘Beam switching and bifocal zoom lensing using active plasmonic metasurfaces’. *Light: Science & Applications* (2017), vol. 6(7): e17016–e17016 (cit. on p. 42).
- [Yu12] NANFANG YU, FRANCESCO AIETA, PATRICE GENEVET, MIKHAIL A KATS, ZENO GABURRO, and FEDERICO CAPASSO: ‘A broadband, background-free quarter-wave plate based on plasmonic metasurfaces’. *Nano letters* (2012), vol. 12(12): pp. 6328–6333 (cit. on p. 2).
- [Yu14] NANFANG YU and FEDERICO CAPASSO: ‘Flat optics with designer metasurfaces’. *Nature materials* (2014), vol. 13(2): pp. 139–150 (cit. on pp. 2, 92).
- [Yu11] NANFANG YU, PATRICE GENEVET, MIKHAIL A KATS, FRANCESCO AIETA, JEAN-PHILIPPE TETIENNE, FEDERICO CAPASSO, and ZENO GABURRO: ‘Light propagation with phase discontinuities: generalized laws of reflection and refraction’. *science* (2011), vol. 334(6054): pp. 333–337 (cit. on pp. 3, 42).
- [Yu15] YE FENG YU, ALEXANDER Y ZHU, RAMÓN PANIAGUA-DOMÍNGUEZ, YUAN HSING FU, BORIS LUK’YANCHUK, and ARSENIY I KUZNETSOV: ‘High-transmission dielectric metasurface with  $2\pi$  phase control at visible wavelengths’. *Laser & Photonics Reviews* (2015), vol. 9(4): pp. 412–418 (cit. on p. 91).
- [Zha17] HANQING ZHANG, TIM STANGNER, KRISTER WIKLUND, ALVARO RODRIGUEZ, and MAGNUS ANDERSSON: ‘UmUTracker: A versatile MATLAB program for automated particle tracking of 2D light microscopy or 3D digital holography data’. *Computer Physics Communications* (2017), vol. 219: pp. 390–399 (cit. on p. 100).
- [Zha19] JIHUA ZHANG, MOHAMED ELKABBASH, RAN WEI, SUBHASH C SINGH, BILLY LAM, and CHUNLEI GUO: ‘Plasmonic metasurfaces with 42.3% transmission efficiency in the visible’. *Light: Science & Applications* (2019), vol. 8(1): pp. 1–13 (cit. on p. 2).
- [Zha21] MAOXIONG ZHAO et al.: ‘Phase characterisation of metalenses’. *Light: Science & Applications* (2021), vol. 10(1): p. 52 (cit. on p. 10).
- [Zhe12] NIKOLAY I ZHELUDEV and YURI S KIVSHAR: ‘From metamaterials to metadevices’. *Nature materials* (2012), vol. 11(11): pp. 917–924 (cit. on p. 2).

- 
- [Zou20] XIUJUAN ZOU, GAIGE ZHENG, QUAN YUAN, WENBO ZANG, RUN CHEN, TIANYUE LI, LIN LI, SHUMING WANG, ZHENLIN WANG, and SHINING ZHU: ‘Imaging based on metalenses’. *Photonix* (2020), vol. 1(1): pp. 1–24 (cit. on p. [14](#)).
- [Zul11] JORGE ZULOAGA and PETER NORDLANDER: ‘On the energy shift between near-field and far-field peak intensities in localized plasmon systems’. *Nano letters* (2011), vol. 11(3): pp. 1280–1283 (cit. on p. [47](#)).

---

## List of Figures

---

2.1	Refractive lens-like phase profile . . . . .	9
2.2	Conventional bulky lens versus an ultrathin metalens . . . . .	10
2.3	Phase distributions for different spherical lenses . . . . .	12
2.4	Fermat's Principle describing optical image formation . . . . .	13
2.5	Magnification and focal length for a set of object and image distances	15
2.6	Dielectric constants for Gold as a function of the wavelength according to Johnson and Christy . . . . .	17
2.7	Polarization modulation in real space and polarization space. . . . .	23
2.8	Non-transitivity of the phase difference among three polarization states	24
2.9	Polarization modulation by different wave plates plotted on the Poincaré sphere . . . . .	26
2.10	Plasmonic metalens for imaging at infrared frequency . . . . .	29
2.11	Schematic concept and characteristics of nonlinear metalenses. . . . .	30
3.1	Schematic energy level diagrams of linear and nonlinear processes. . . . .	34
3.2	Graphical calculation method to determine the Pancharatnam-Berry phase on the Poincaré sphere. . . . .	41
3.3	Schematic concept of the imaging with a nonlinear metalens . . . . .	44
3.4	Fabrication process of the nonlinear plasmonic metalens . . . . .	45
3.5	C3 meta-atom size analysis. . . . .	46
3.6	Measured localized surface plasmon polariton resonance. . . . .	46
3.7	Nonlinear spectroscopy measurement of SHG intensity . . . . .	48
3.8	SHG Measurement of the beam propagation in focal region. . . . .	49
3.9	Measured SHG intensity distribution at the focal plane. . . . .	50
3.10	Schematic illustration of the measurement setup. . . . .	52
3.11	1:1 spin-dependent object imaging with nonlinear metalens. . . . .	55
3.12	Nonlinear imaging of double slit apertures. . . . .	57
3.13	Schematic concept of spin controlled orbital angular momentum gen- eration with a nonlinear plasmonic metasurface. . . . .	58
3.14	Plasmonic metasurface design and SHG measurements. . . . .	61
4.1	THG amplitude and phase for different nanopillar geometries. . . . .	65
4.2	SEM images of a nonlinear dielectric metalens. . . . .	66
4.3	TH diffraction efficiency. . . . .	67

4.4	Nonlinear conversion and focusing of the fundamental Gaussian beam.	69
4.5	Image formation of a single Gaussian beam waist. . . . .	74
4.6	Numerical simulation of the THG image formation . . . . .	76
4.7	Simulation and measurement of the THG image formation for an L-shaped aperture. . . . .	77
4.8	Measurement of the THG image formation for different object distances.	78
4.9	Nonlinear imaging governed by the generalized Gaussian lens equation.	80
4.10	Nonlinear virtual image formation with converging THG metalens . .	81
4.11	Simulation of the image formation of two Gaussian beams. . . . .	83
4.12	Nonlinear imaging and spatial correlation for two apertures. . . . .	85
4.13	Nonlinear imaging and higher-order spatial correlations for three apertures. . . . .	86
5.1	Ray optics explanation of the momentum conservation in optical tweezers	90
5.2	Schematic concept and SEM image of the all-dielectric metalens . . .	93
5.3	Optical characterization of the all-dielectric metalens . . . . .	95
5.4	Measurement of the metasurface diffraction efficiency . . . . .	96
5.5	Optical characterization of the vortex metalens . . . . .	97
5.6	Schematic illustration of the measurement setup. . . . .	98
5.7	Metalens for 2D polarization-sensitive drag and drop manipulation of particles. . . . .	101
5.8	Vortex metalens for OAM transfer . . . . .	102
A.1	Geometric optical propagation of a ray of light through a conventional lens . . . . .	129
C.1	Beam propagation method for linear and nonlinear metalens . . . . .	134
D.1	Measurement of the fundamental wave propagation behind two circular apertures and the corresponding TH image formation. . . . .	135
D.2	Nonlinear imaging accompanied by a higher-order autocorrelation. . .	136

## A Derivation of the lensmaker's equation

A conventional bulky refractive lens is an optical device that can focus a collimated beam at an focal point  $F$ . The distance from the center of the lens to this point is called focal distance  $f$ . The question arises how to choose the radius of curvature to focus light exactly at a given focal length. As depicted in fig. A.1, an incident ray of light propagates through a medium with refractive index of  $n_1$  parallel to the optical axis in a vertical position  $\varrho_1$ . The beam is two times refracted at each interface of surrounding medium (with refractive index  $n_1$ ) and the curved surfaces of the lens (with refractive index  $n_2$ ) that are described by the radii of curvature  $R_1$  and  $R_2$ . The beam emerges from the lens in a vertical position  $\varrho_2$ . The angle of incidence at the first (second) interface is  $\alpha_1$  ( $\alpha_3$ ) and the angle of refraction with respect to the normal is  $\alpha_2$  ( $\alpha_4$ ). Note that the size of the lens is exaggerated in the drawing.

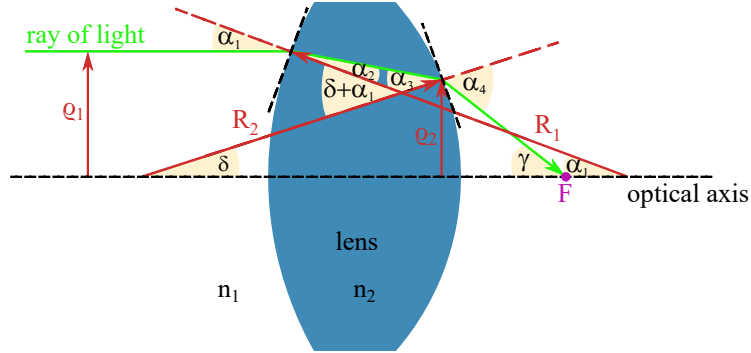


**Figure A.1: Geometric optical propagation of a ray of light through a conventional lens.** An optical lens with refractive index  $n_2$  and radii of curvature  $R_1$  and  $R_2$  is surrounded by a medium with refractive index  $n_1$ . A ray of light (green) hits the lens at a height  $\varrho_1$ . The two refractions of the beam at the interfaces are described by the angles of incidence  $\alpha_1$  and  $\alpha_3$ , and the angles of refraction  $\alpha_2$  and  $\alpha_4$ . The beam then emerges from the lens at a height  $\varrho_2$  and is deflected to the optical axis, with which it encloses an angle  $\gamma$ .

Realistically, the lens is thin, so the following simplifying assumptions are valid:

$$\begin{aligned} \sin \alpha &\approx \tan \alpha \approx \alpha \\ \varrho_1 &\approx \varrho_2 := \varrho \end{aligned} \tag{A.1}$$

The beam deflections at both interfaces are governed by well-known Snell's law.

$$\begin{aligned} n_1 \sin \alpha_1 &= n_2 \sin \alpha_2 \rightarrow n_1 \alpha_1 \approx n_2 \alpha_2 \\ n_1 \sin \alpha_3 &= n_2 \sin \alpha_4 \rightarrow n_1 \alpha_3 \approx n_2 \alpha_4 \end{aligned} \quad (\text{A.2})$$

Basic trigonometric relations can be found from fig. A.1:

$$\begin{aligned} \alpha_1 &= \sin \frac{\varrho_1}{R_1} \approx \frac{\varrho}{R_1} \\ \gamma &= \tan \frac{\varrho_2}{f} \approx \frac{\varrho}{f} \\ \delta &= \sin \frac{\varrho_2}{R_2} \approx \frac{\varrho}{R_2} \end{aligned} \quad (\text{A.3})$$

In the next step, geometric equations are found to describe relations between the angles.

$$\begin{aligned} \alpha_4 &= \gamma + \delta \\ \alpha_2 + \alpha_3 &= \delta + \alpha_1 \end{aligned} \quad (\text{A.4})$$

Starting from the last equation, all other relations can be inserted successively.

$$\begin{aligned} \frac{n_1}{n_2}(\alpha_1 + \alpha_4) &= \varrho \left( \frac{1}{R_1} + \frac{1}{R_2} \right) \\ \frac{n_1}{n_2} \left( \frac{\varrho}{R_1} + \gamma + \delta \right) &= \varrho \left( \frac{1}{R_1} + \frac{1}{R_2} \right) \quad \Big| : \varrho \\ \frac{n_1}{n_2} \left( \frac{1}{R_1} + \frac{1}{f} + \frac{1}{R_2} \right) &= \left( \frac{1}{R_1} + \frac{1}{R_2} \right) \end{aligned} \quad (\text{A.5})$$

Further mathematical simplifications are used to derive the lensmaker's equation:

$$\frac{1}{f} = \left( \frac{n_2}{n_1} - 1 \right) \left( \frac{1}{R_1} + \frac{1}{R_2} \right) \quad (\text{A.6})$$

If one observes the directions of the radii of curvature in fig. A.1,  $R_1$  should enter the equation with a negative sign. This sign is added in the main text.

## B Polarization manipulation in an experimental setup

The following calculation shows an example of a component cascade, the basic idea of which will be helpful for the experimental setup used to investigate metasurfaces that induce a geometric phase change.

$$\begin{aligned}
|j_{\text{out}}\rangle &= M_{\text{hlp}} M_{\text{qwp}}(\pi/4) M_{\text{hwp}}(0) M_{\text{qwp}}(\pi/4) M_{\text{hlp}} |H\rangle \\
&= M_{\text{hlp}} M_{\text{qwp}}(\pi/4) M_{\text{hwp}}(0) M_{\text{qwp}}(\pi/4) |H\rangle \\
&= M_{\text{hlp}} M_{\text{qwp}}(\pi/4) M_{\text{hwp}}(0) |R\rangle \\
&= M_{\text{hlp}} M_{\text{qwp}}(\pi/4) |L\rangle \\
&= M_{\text{hlp}} |H\rangle \\
&= |H\rangle.
\end{aligned} \tag{B.1}$$

A horizontal input polarization  $|H\rangle$  remains unchanged after passing a horizontally aligned linear polarizer and converts to right circularly polarized light (RCP)  $|R\rangle$  with the help of a quarter wave plate (QWP) with its fast axis aligned in a  $45^\circ$  angle with the  $x$ -axis (mathematically positiv sense of rotation). These first two components can be described as a circular polarizer, which only allows RCP light to pass through [Col84]. The HWP changes the sign of the  $y$  component in the Jones vector so that the helicity is changed to left circularly polarized light (LCP)  $|L\rangle$ . The polarization is converted again to horizontal by a second QWP that is aligned like the first one. Then the light intensity remains the same after passing a horizontal polarizer. The last two components can be denoted as a circular polarization analyzer, which only allows LCP light to pass through. By inserting the HWP in the center, there is a delay between  $x$  and  $y$  components, which corresponds to a half wavelength or the phase shift  $\pi$ . A closer look at equation B.1 reveals that the angle of the fast axis of the HWP seems to be irrelevant. Only the phase retardation is decisive. By removing the HWP from the setup no light will pass because only light in circular cross polarization is measured (RCP to LCP). This behavior is expected, since two quarter-wave plates with the same orientation (angle of  $45^\circ$ ) can be regarded as one half-wave plate, which then rotates the linear polarization by an angle of  $90^\circ$ . This component cascade is thus a setup for measuring the circular cross- and co-polarizations. By changing both angles of the QWPs to  $-45^\circ$  the opposite cross-circular polarization (LCP to RCP) is measured. The corresponding co-polarizations (LCP to LCP and RCP to RCP) can be measured accordingly.

This experimental component setup is very similar to the experimental setup used

to study geometric metasurfaces. To measure the Pancharatnam-Berry effect, the observation of the output beam from the metasurface has to be done in the circular cross-polarization relative to the input beam [Min18]. Thus, in this example, the half-wave plate will serve as a placeholder for the metasurfaces studied later.

## C Numerical simulation via beam propagation method for linear and nonlinear metalens

The following figure illustrates exemplarily a numerical calculation using the beam propagation method (fig. C.1). The L-shaped aperture is located in the distance of the focal length  $f = 500 \mu\text{m}$  to the metalens, so the object distance is  $a = -500 \mu\text{m}$ . The aperture is illuminated with a plane wave. After the propagation to the metalens (at  $z = 0 \mu\text{m}$ ) the phase and intensity distribution still show the upright L-shape very well (blue box). In the red box, the propagation through a linear metalens is demonstrated. The intensity distribution of the fundamental wave that contains the phase information of the lens is not changed in this case. Since the object is exactly placed in the distance of the focal length to the linear metalens, no sharp image can be obtained after propagating through the lens. This observation is consistent with the expectation from the Gaussian lens equation, since the image distance diverges in this experimental configuration.

The case of the nonlinear lens is shown in the green box. Due to the nonlinear second harmonic generation process, the electromagnetic field is squared and the intensity distribution of the electromagnetic field that contains the phase information of the lens changes compared to the linear case. The phase distribution has shorter periods from 0 to  $2\pi$  because the design wavelength in the lens-like phase profile is halved compared to the linear case. In the nonlinear signal, it is clear to see how the image forms from the focal plane at  $z = 500 \mu\text{m}$ , giving a sharp SHG image at an image distance of  $b = 2f = 1000 \mu\text{m}$ .

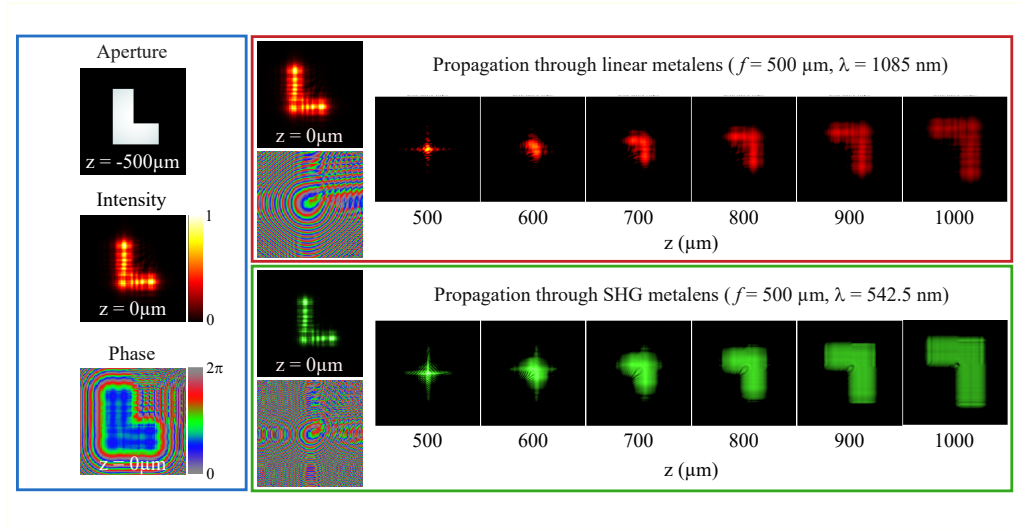


**Figure C.1: Beam propagation method for linear and nonlinear metalens.** **Blue box** L-shaped aperture object is placed in an object distance of  $a = -500 \mu\text{m}$ . The intensity and phase distribution is shown in the plane of the metalens. **Red box** The first two images show the direct effect of the linear lens on the intensity and phase distribution. The propagation through the linear metalens is illustrated by different transverse planes along the  $z$ -propagation direction. **Green box** Corresponding result from the simulation of the propagation through the SHG metalens. The metalens works as a convex lens so that the real image is formed at  $b = 1000 \mu\text{m}$  behind the metalens with the magnification  $\Gamma = -1$ .

## D Experimental demonstration of TH imaging of two and three apertures

The nonlinear nature of the metalens is investigated by imaging an object consisting of two apertures. By using a NIR camera (Xenics Xeva) in a second beam path, one can visualize the beam propagation of the fundamental wave behind the circular apertures true to scale (fig. D.1). The fundamental light propagates through the two

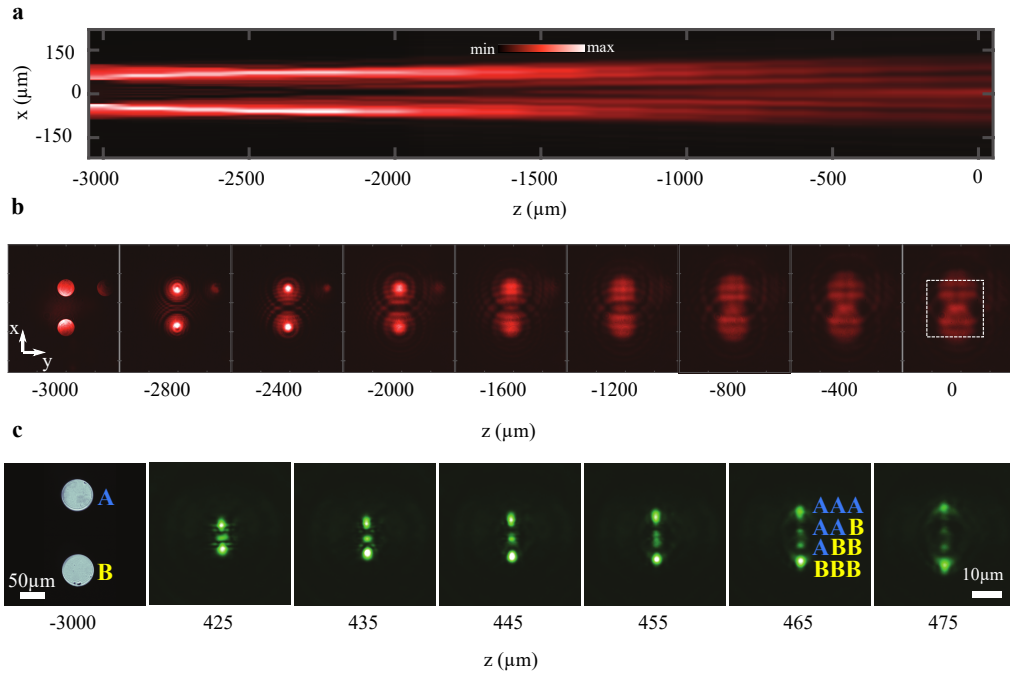


**Figure D.1: Measurement of the fundamental wave propagation behind two circular apertures and the corresponding TH image formation.** **a** Ray tracing on the optical axis with consistent axis scaling. The circular apertures are placed at an object distance of  $a = -3$  mm in front of the metalens. **b** Corresponding transverse intensity distributions on the optical axis. At  $z = 0$   $\mu\text{m}$  the position and size of the nonlinear metalens is shown with a dashed white line. **c** Left: The white light image of the two circular apertures (A and B) in front of the metalens. Right: Cross-section of the corresponding TH intensity after the metalens showing the formation of four maxima associated with the third-order spatial autocorrelation function of the object. Both apertures are simultaneously illuminated with a weakly collimated beam at  $\lambda = 1550$  nm.

apertures and diffracts during the propagation in the linear regime. In fig. D.1 b, the metalens position and size is marked with a dashed white line. Therefore, five different intensity maxima are expected on the nonlinear metalens (comparable to the simulated case with two interfering Gaussian beams in fig. 4.11 d). The signal interferes at the metalens surface and is partially converted to the third-harmonic wavelength. For six selected distances, the transverse TH intensity cross-sections are shown in fig. D.1 c. At the location of the image plane ( $z = 465 \mu\text{m}$ ), four THG intensity maxima are observed instead of two expected spots for linear optics.

According to fig. 4.13, the following figure shows the measured cross-sections of the TH intensity after adding a third circular aperture (fig. D.2). The apertures form a right-angled triangle  $\Delta_{ABC}$ . In an image distance of  $b = 465 \mu\text{m}$ , a similar higher-order correlation process is observed, which shows two additional maxima on every side of the triangle. The distance between the additional maxima on the longer side  $AC$  is greater than on the shorter sides  $BC$  and  $AB$ . Additionally, one can find one central maximum at frequency  $3\omega$  resulting from three  $\omega$ -photons coming from each of the three circular apertures.

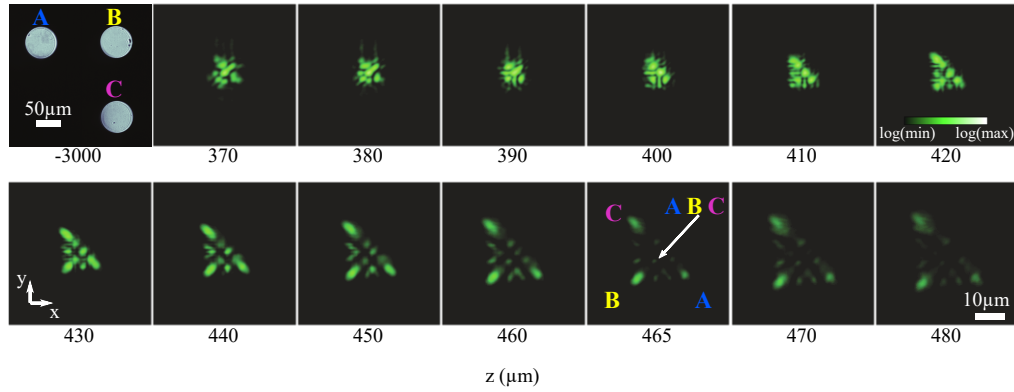


**Figure D.2: Nonlinear imaging accompanied by a higher-order autocorrelation.** Three circular apertures (left top) are illuminated simultaneously at the object distance  $a = -3 \text{ mm}$ . The corresponding experimentally obtained TH intensity distributions at various cross-sections behind the metalens show the formation of 10 maxima associated with the third-order autocorrelation. The image plane for this configuration is at  $b = 465 \mu\text{m}$ . The marked spot corresponds to the THG signal containing photons from all three apertures.

## E Scientific publications

### Scientific publications in peer reviewed journals

1. TEANCHAI CHANTAKIT\*, **Christian Schlickriede**\*, BASUDEB SAIN, FABIAN MEYER, THOMAS WEISS, NATTAPORN CHATTHAM, and THOMAS ZENTGRAF: ‘All-dielectric silicon metalens for two-dimensional particle manipulation in optical tweezers’. *Photonics Research* (2020), vol. 8(9): pp. 1435–1440.
2. LINGXIAO ZHU, XUAN LIU, BASUDEB SAIN, MENGYAO WANG, **Christian Schlickriede**, YUTAO TANG, JUNHONG DENG, KINGFAI LI, JUN YANG, MICHAEL HOLYNSKI, SHUANG ZHANG, THOMAS ZENTGRAF, KAI BONGS, YU-HUNG LIEN, and GUIXIN LI: ‘A dielectric metasurface optical chip for the generation of cold atoms’. *Science Advances* (2020), vol. 6(31): eabb6667.
3. HONGQIANG ZHOU, BASUDEB SAIN, YONGTIAN WANG, **Christian Schlickriede**, RUIZHE ZHAO, XUE ZHANG, QUNSHUO WEI, XIAOWEI LI, LINGLING HUANG, and THOMAS ZENTGRAF: ‘Polarization-Encrypted Orbital Angular Momentum Multiplexed Metasurface Holography’. *ACS nano* (2020), vol. 14(5): pp. 5553–5559.
4. **Christian Schlickriede**, SERGEY S KRUK, LEI WANG, BASUDEB SAIN, YURI KIVSHAR, and THOMAS ZENTGRAF: ‘Nonlinear imaging with all-dielectric metasurfaces’. *Nano Letters* (2020), vol. 20(6): pp. 4370–4376.
5. SATAYU SUWANNASOPON, FABIAN MEYER, **Christian Schlickriede**, PAPHICHAYA CHAISAKUL, JUMRAS LIMTRAKUL, THOMAS ZENTGRAF, and NATTAPORN CHATTHAM: ‘Miniaturized Metalens Based Optical Tweezers on Liquid Crystal Droplets for Lab-on-a-Chip Optical Motors’. *Crystals* (2019), vol. 9(10): p. 515.
6. **Christian Schlickriede**, NAOMI WATERMAN, BERNHARD REINEKE, PHILIP GEORGI, GUIXIN LI, SHUANG ZHANG, and THOMAS ZENTGRAF: ‘Imaging through nonlinear metalens using second harmonic generation’. *Advanced Materials* (2018), vol. 30(8): p. 1703843.
7. QINGHUA GUO\*, **Christian Schlickriede**\*, DONGYANG WANG, HONGCHAO LIU, YUANJIANG XIANG, THOMAS ZENTGRAF, and SHUANG ZHANG: ‘Manipulation of vector beam polarization with geometric metasurfaces’. *Optics Express* (2017), vol. 25(13): pp. 14300–14307.

8. PHILIP GEORGI, **Christian Schlickriede**, GUIXIN LI, SHUANG ZHANG, and THOMAS ZENTGRAF: ‘Rotational Doppler shift induced by spin-orbit coupling of light at spinning metasurfaces’. *Optica* (2017), vol. 4(8): pp. 1000–1005.
9. MANUEL PETER, ANDRE HILDEBRANDT, **Christian Schlickriede**, KIMIA GHARIB, THOMAS ZENTGRAF, JENS FÖRSTNER, and STEFAN LINDEN: ‘Directional emission from dielectric leaky-wave nanoantennas’. *Nano Letters* (2017), vol. 17(7): pp. 4178–4183.
10. GUIXIN LI, LIN WU, KING F LI, SHUMEI CHEN, **Christian Schlickriede**, ZHENGJI XU, SIYA HUANG, WENDI LI, YANJUN LIU, EDWIN YB PUN, THOMAS ZENTGRAF, KOK W. CHEAH, YU LUO, and SHUANG ZHANG: ‘Nonlinear metasurface for simultaneous control of spin and orbital angular momentum in second harmonic generation’. *Nano letters* (2017), vol. 17(12): pp. 7974–7979.
11. CHRISTINA ALPMANN, **Christian Schlickriede**, EILEEN OTTE, and CORNELIA DENZ: ‘Dynamic modulation of Poincaré beams’. *Scientific Reports* (2017), vol. 7(1): pp. 1–9.
12. EILEEN OTTE, **Christian Schlickriede**, CHRISTINA ALPMANN, and CORNELIA DENZ: ‘Complex light fields enter a new dimension: holographic modulation of polarization in addition to amplitude and phase’. *Proceedings of SPIE Complex Light and Optical Forces IX* (2015), vol. 9379: p. 937908.

\* - These authors contributed equally to this work.

## Contributions to international conferences

1. CHRISTIAN SCHLICKRIEDE, SERGEY S KRUK, LEI WANG, BASUDEB SAIN, YURI KIVSHAR, and THOMAS ZENTGRAF: ‘Third-harmonic imaging with all-dielectric nonlinear metalenses’. *CLEO/Europe-EQEC*. Munich, Germany, 2019.
2. CHRISTIAN SCHLICKRIEDE, SERGEY S KRUK, LEI WANG, BASUDEB SAIN, YURI KIVSHAR, and THOMAS ZENTGRAF: ‘Nonlinear dielectric metalenses: imaging and higher-order correlations’. *Postdeadline oral presentation at CLEO: QELS Fundamental Science*. San Jose, California, United States, 2019.
3. CHRISTIAN SCHLICKRIEDE, BASUDEB SAIN, and THOMAS ZENTGRAF: ‘Ultrathin metalenses for imaging with high harmonic generation processes’. *Invited presentation at E-MRS Fall Meeting*. Warsaw, Poland, 2018.
4. THOMAS ZENTGRAF, CHRISTIAN SCHLICKRIEDE, BERNHARD REINEKE, PHILIP GEORGI, and GUIXIN LI: ‘Imaging by Nonlinear Plasmonic Metalenses’. *Nonlinear Photonics*. Zurich, Switzerland, 2018.
5. CHRISTIAN SCHLICKRIEDE, BERNHARD REINEKE, PHILIP GEORGI, THOMAS ZENTGRAF, SHUANG ZHANG, and GUIXIN LI: ‘Subwavelength Pancharatnam-Berry phase controlled metasurface for imaging with instantaneous SHG’. *SPIE NanoScience Engineering*. San Diego, California, United States, 2017.
6. CHRISTIAN SCHLICKRIEDE, TEANCHAI CHANTAKIT, BASUDEB SAIN, HEINZ-SIEGFRIED KITZEROW, THOMAS ZENTGRAF, and NATTAPORN CHATTHAM: ‘Optical tweezers with high-efficiency dielectric metalenses’. *DPG Frühjahrstagung*. Regensburg, Germany, 2019.
7. CHRISTIAN SCHLICKRIEDE, PHILIP GEORGI, GUIXIN LI, SHUANG ZHANG, and THOMAS ZENTGRAF: ‘Imaging with ultrathin nonlinear metalenses’. *DPG Frühjahrstagung*. Berlin, Germany, 2018.
8. CHRISTIAN SCHLICKRIEDE, GUIXIN LI, SHUANG ZHANG, and THOMAS ZENTGRAF: ‘Subwavelength Pancharatnam-Berry phase controlled metasurface for imaging with instantaneous SHG’. *Europhotonics POESII Spring School*. Barcelona, Spain, 2017.
9. CHRISTIAN SCHLICKRIEDE, EILEEN OTTE, CHRISTINA ALPMANN, and CORNELIA DENZ: ‘Spatially variable polarization modulation of Laguerre-Gaussian beams’. *Europhotonics POESII Spring School*. Porquerolles, France, 2016.

10. CHRISTINA ALPMANN, EILEEN OTTE, CHRISTOPH SCHÖLER, CHRISTIAN SCHLICKRIEDE, and CORNELIA DENZ: ‘Complex light for optical micro-manipulation: amplitude, phase and polarization modulation’. *Optical Trapping Applications*. Vancouver, Canada, 2015.
11. CHRISTIAN SCHLICKRIEDE, CHRISTINA ALPMANN, and CORNELIA DENZ: ‘Dynamic polarization modulation of tailored light fields’. *SPIE Photonics Europe*. Brussels, Belgium, 2014.

## Acknowledgments

At this point I would like to take the opportunity to thank and give credits to all of the people that contributed to the success of this thesis.

First of all I would like to thank Prof. Thomas Zentgraf who not only gave me the opportunity to write this thesis and do my research projects at Paderborn University but assisted me with my thesis through his compelling experience and thoughtful advice. He helped me in every way possible to solve any problem that occurred in the cause of the research project, gave me the confidence and space I needed to fully expand my personal potential and showed me through out his daily actions and advice what it takes to be an excellent and proficient scientist. I surely owe him my profoundest apologies for keeping him on the edge of his nerves when he had to wait for me to finish a project and I am deeply thankful for his patience and steadfast confidence in me and my work. I am especially thankful for offering me the opportunity to speak at international conferences on behalf of our working group, present my studies to an international experts in the field and grow throughout the process.

I would like to thank Prof. Heinz Kitzrow who agreed to be my second supervisor. I very much enjoyed the cooperation and I am very thankful for his time and effort.

I would also like to take the time to thank some scientists from other universities who generously shared their expertise with me and contributed significantly to the success of this thesis: I am particularly grateful for the support from Prof. Guixin Li from the Southern University of Science and Technology in China and Prof. Shuang Zhang from the University of Birmingham who helped me to implement and analyze the experiments on the plasmonic SHG metalens. Moreover, I owe my sincere thanks to Prof. Yuri Kivshar and Dr. Sergey Kruk from the Australian National University for assisting me with the investigation of the dielectric THG metalens. Furthermore, I would like to thank Prof. Nattaporn Chattham, from the Kasetsart University and Dr. Teanchai Chantakit from the King Mongkut's Institute of Technology in Thailand. They both contributed a lot in the implementation of the dielectric metalens for integration in optical tweezers. In this respect, I also thank Prof. Thomas Weiss from the University of Stuttgart who provided the RCWA code I used for this project.

I would like to thank my office mates Philip Georgi and Florian Spreyer for not just the scientific debates we had on a daily basis but also for their helpful explanations

whenever I asked for their professional or personal advice. Furthermore, I would like to thank Felicitas Walter, Bernhard Reineke, Daniel Frese and Holger Mühlenbernd for their committed cooperation and shared knowledge about sample fabrication that helped me to quickly fabricate high quality samples on my own. I would also like to give special thanks to Dr. Basudeb Sain for sharing his unparalleled experience in fabrication of dielectric samples and the excellent collaboration in various projects. Since our group has a lot of excellent researchers who are willing to share their knowledge and also like to give you fruitful company while working late in the evening, I would also like to thank Dr. Wenlong Gao, René Geromel, Jinlong Lu, Sophia Thies, Carsten Müller, Lucas Pauly, and Fabian Meier. We shared lively exchange of experiences as well as some lovely conversations and I am truly thankful for your companionship and the great working atmosphere.

Special thanks go to my colleagues of the GRK 1464, especially to Sarah Blumenthal, Thomas Hett, Christoph Eigner, Thorsten Meyers, Nils Weber, Michael Rüsing, Christoph Brodehl, and Joachim Vollbrecht for several critical questions, stimulating discussions and for one or two small beers shared after a long day of work.

In the context of proofreading, I highly appreciate the feedback that I got from Philip Georgi, Christoph Schöler and Evgenij Travkin. It was a fascinating experience to get a different perspective on the subject.

Last but not least I would like to thank my parents, my family and my friends. Thank you for your unconditional love and support, for your patience and your never ending trust in me and the path in life I chose. I would particularly like to thank Laura for her encouragement, understanding, and patience even during hard times.